AD_____

Award Number: DAMD17-96-1-6131

TITLE: Vascular Functional Imaging and Physiological Environment of Hyperplasia, Non-Metastatic and Metastatic Breast Cancer

PRINCIPAL INVESTIGATOR: Zaver M. Bhujwalla, Ph.D.

CONTRACTING ORGANIZATION: The Johns Hopkins University
Baltimore, Maryland 21205-2196

REPORT DATE: October 2001

TYPE OF REPORT: Final

PREPARED FOR: U.S. Army Medical Research and Materiel Command
Fort Detrick, Maryland 21702-5012

# REPORT DOCUMENTATION PAGE

*Form Approved*
*OMB No. 074-0188*



| 1. AGENCY USE ONLY (Leave blank) | 2. REPORT DATE | 3. REPORT TYPE AND DATES COVERED |
|---|---|---|
| | October 2001 | Final (01 Oct 96 - 30 Sep 01) |

**4. TITLE AND SUBTITLE**
Vascular Functional Imaging and Physiological Environment of Hyperplasia, Non-Metastatic and Metastatic Breast Cancer

**5. FUNDING NUMBERS**
DAMD17-96-1-6131

**6. AUTHOR(S)**
Zaver M. Bhujwalla, Ph.D.

**7. PERFORMING ORGANIZATION NAME(S) AND ADDRESS(ES)**
The Johns Hopkins University
Baltimore, Maryland 21205-2196

E-Mail: zaver@mri.jhu.edu

**8. PERFORMING ORGANIZATION REPORT NUMBER**

**9. SPONSORING / MONITORING AGENCY NAME(S) AND ADDRESS(ES)**
U.S. Army Medical Research and Materiel Command
Fort Detrick, Maryland 21702-5012

**10. SPONSORING / MONITORING AGENCY REPORT NUMBER**

**11. SUPPLEMENTARY NOTES**
Report contains color

**12a. DISTRIBUTION / AVAILABILITY STATEMENT**
Approved for Public Release; Distribution Unlimited

**12b. DISTRIBUTION CODE**

**13. ABSTRACT** ***(Maximum 200 Words)***

Our goals were to understand the role of vascularization and physiological and metabolic properties in breast cancer metastasis using magnetic resonance (MR) imaging (I) and MR spectroscopy (S) of human breast cancer models.
Key findings were:
MR spectra of tumors revealed a significant differences in phospholipid composition and in intra- and extracellular pH, between control and transgene tumors formed by MDA-MB-435 human breast carcinoma cells transfected with nm23 constructs. These data demonstrate the potential of noninvasive MRS to detect forms of gene therapy which may involve transfection of cells with nm23. Choline phospholipid metabolite levels progressively increased in cultured human mammary epithelial cells (HMECs) as cells became more malignant. This work is relevant to diagnosis of breast cancer and provides a rationale for selective pharmacological intervention. Lactate levels increased significantly in cultured HMEC following malignant transformation and may promote invasive behavior and contribute to metastasis. 3-dimensional analysis of vascular volume and permeability and histological morphology demonstrated that areas of low vascular volume were associated with cell death and increasingly permeable vasculature. The more metastatic cell lines were characterized by higher vascular volume and permeability. These results indicate a potential use of MRI and MRS for evaluating 'metastatic risk' noninvasively.

| 14. SUBJECT TERMS | 15. NUMBER OF PAGES |
|---|---|
| Research, Breast Cancer, Vascularization, Metastasis | 83 |
| | 16. PRICE CODE |

| 17. SECURITY CLASSIFICATION OF REPORT | 18. SECURITY CLASSIFICATION OF THIS PAGE | 19. SECURITY CLASSIFICATION OF ABSTRACT | 20. LIMITATION OF ABSTRACT |
|---|---|---|---|
| Unclassified | Unclassified | Unclassified | Unlimited |

## TABLE OF CONTENTS

## INTRODUCTION

Vascularization plays a key role in the growth and metastasis of solid tumors [1-3]. In two recent clinical studies, breast cancer patients whose tumors had a high vascular density subsequently went on to develop metastases over a follow up period of 2.5 years [4, 5]. Statistical analyses of these patients showed that vascular density was the single most important factor ($p<0.006$) associated with subsequent formation of metastasis [4]; the other factors examined were epidermal growth factor receptor status ($p<0.01$), node status ($p<0.02$), estrogen receptor status ($p< 0.05$), tumor size ($p<0.06$), tumor grade ($p<0.5$), c-erb-2 expression ($p<0.7$), p53 ($p<0.8$) and tumor type ($p<0.8$). Studies correlating vascularization with metastasis have so far been performed with histological evaluation of excised tissue specimens as a result of which information regarding functioning of vessels is lost. Similarly, the physiological environment of these tumors, in terms of acidity and lactate production remains unknown. Thus a lack of noninvasive methods has left some vital questions about the precise nature of the relationship between vascularization and metastasis unanswered. Tumor neovascularization is induced by the secretion of angiogenic factors which act as chemotactic factors and mitogens for endothelial cells [6]. One of the most potent of these is vascular endothelial growth factor (VEGF) [7]. VEGF also increases vascular permeability [8] which in turn may allow cancer cells greater access to the vasculature [9]. In glioblastoma multiformae areas of necrosis and hypoxia show a higher expression of VEGF [9, 10]. Poorly functioning vessels and the associated hypoxia and necrosis may play a role in attracting further vascularization. Areas of hypoxia are also associated with accumulation of lactate and low pH. These two physiological factors attract neovascularization by stimulating the secretion of angiogenic factors from macrophages [11]. The secretion of enzymes which degrade the basement membrane in the metastatic process increases at low pH [12-14]. Thus, vascularization, the physiological environment, and formation of metastases are highly interdependent. An understanding of the role of the physiological environment in vascularization and metastasis, and the dependence of this environment on metastatic phenotype are essential to delineate the relationship between vascularization and metastasis. Questions which are central to understanding this relationship are - (1) does the metastatic phenotype induce a higher degree of vascularization and is this mediated by modulation of the physiological environment ? (addressed in Specific Aims 1 and 3) (2) If so, do nonmetastatic tumors and preneoplastic tissue exhibit proportionately lower vascularization ? (addressed in Specific Aims 1 and 2) (3) Which particular property of the vascularization e.g. permeability, or vascular volume is the dominant factor in the dependence of metastasis on vascularization ? (addressed in Specific Aims 1 and 2) (4) Is a significant fraction of the vessels observed in the histological studies non-functional and does the resultant unsuitable environment induce expression of signals or substances which prompt and enable the cells to metastasize ? (addressed in Specific Aim 1). The overall goal of this research proposal is to use noninvasive Magnetic Resonance (MR) Imaging (I) and Spectroscopy (S) to answer the questions posed above.

## BODY

The research proposed consisted of three closely related aims which were designed to unravel the complex relationship between vascularization and metastasis. Our overall goal in this project was to determine key vascular and physiological properties which result in the close relationship between vascular density and metastasis as this information may ultimately be used to prevent tumor metastasis. We had proposed the following three aims:

Aim 1: To investigate the relationship between the metastatic phenotype and the development of vascularization and evaluate the functionality of the developing vascularization in terms of vascular volume, vascular permeability and relative perfusion.
Hypothesis #1: More metastatic lines will exhibit a higher level of vascularization and permeability for similar volumes. A significant number of vessels detected by immunoperoxidase staining will not be functional and this number will increase with the size of the tumor.

Aim 2: To investigate the effect of increasing (a) tumor vascularization and (b) tumor vascularization and permeability on the formation of metastases.
Hypothesis #2: Higher vascularization and permeability will lead to an increase or an earlier incidence of metastases for all the lines.
(Aims 1 and 2 are related to questions 1-4 outlined in background)

Aim 3: To determine the relationship between metastatic phenotype and intra- and extracellular pH and lactate production.
Hypothesis #3: More metastatic lines will be more glycolytically active *in vivo*, creating an environment of high lactate and low extracellular pH for volume matched lesions.
(Aim 3 is related to question 1 outlined in background)

The technical objectives outlined in our statement of work were to delineate the role of vascular volume, permeability and perfusion and tumor physiological environment in the formation of metastasis from human breast cancer lines with preselected invasive and metastatic potential grown in SCID (severe combined immune deficient) mice.

***Final Report for the funding period covering 10/1/96 to 9/31/00 and a no-cost extension period of 10/1/00 to 9/31/01.***

## Progress in Year 1

In the progress report for Year 1 we presented data which demonstrated that there were significant differences in the vascular volume generated by a invasive metastatic human breast cancer line MDA-MB-231 and a nonmetastatic mouse tumor model RIF-1. Studies correlating VEGF distribution with MRI maps of vascular volume and permeability demonstrated that areas around necrosis showed high expression of VEGF and were more permeable. In Year 1 we also presented data to demonstrate that there were significant differences in pH regulation and the phospholipid metabolism in solid tumors growing *in vivo* in SCID mice for a highly metastatic and a less metastatic human breast cancer line. We had therefore made significant progress in Aim 1 and Aim 3 by the end of the first year of the grant.

Details of these studies can be found in the following published manuscripts which are included as appendices.

Bhujwalla, Z. M., Artemov, D., Glockner, J. Tumor angiogenesis, vascularization and contrast enhanced MRI. *Topics in Magnetic Resonance Imaging,* 10(2):92-103, 1999. **Appendix #1**

Bhujwalla, Z. M., Aboagye, E. O., Gillies, R. J., Chacko, V. P., Mendola, C. E., Backer, J. M. Nm23-transfected MDA-MB-435 human breast carcinoma cells form tumors with altered phospholipid metabolism and pH. A $^{31}$P NMR study *In vivo* and *In vitro. Magnetic Resonance in Medicine,* 41: 897-903, 1999. **Appendix #2**

**Progress in Year 2**

In Year 2 we had the following achievements. First we showed that the alterations in phospholipid metabolism observed for a highly metastatic and less metastatic tumor could be generalized to an entire panel of human mammary epithelial cells, ranging from normal to highly malignant and metastatic. We also demonstrated that lactate levels significantly increased in malignant cells compared to normal and immortalized hyperplastic human mammary epithelial cells. In addition we developed an implemented multi-slice imaging pulse sequences instead of the originally proposed single slice studies of tumors to determine the vascular characteristics over the entire tumor. We also developed a visualization software program which would allow us to interactively relate MRI information with histological maps. Details of these studies can be found in the following published manuscripts which are included as appendices.

Aboagye, E. and Bhujwalla, Z. M. Malignant Transformation Alters Membrane Phospholipid Metabolism of Human Mammary Epithelial Cells. *Cancer Research,* 59, 80-84, 1999. **Appendix #3**.

Aboagye, E., Mori, N., and Bhujwalla, Z. M. Effect of Malignant Transformation on lactate levels of Human Mammary Epithelial Cells. *Advances in Enzyme Regulation,* Vol.41, pp 251-260, 2001. **Appendix #4.**

Gillies, R. J., Bhujwalla, Z. M., Evelhoch, J., Garwood, M., Neeman, M., Robinson, S. P., Sotak, C. H., van der Sanden, B. Applications of Magnetic Resonance in Model Systems I: Tumor Biology and Physiology. *Neoplasia,* 2(1):1-14, 2000. **Appendix #5.**

**Progress in Year 3**

In Year 3 used the significant technical advances made in year 2 to characterize vascular patterns for three human breast cancer lines, MDA-MB-435, MDA-MB-231 and MCF-7 inoculated in the mammary fat pad of SCID mice. In addition, we developed a technique to image tumor extracellular pH using proton spectroscopic imaging. Details of these studies can be found in the following published manuscript which is included as an appendix.

van Sluis R, Bhujwalla Z, Raghunand N, Ballesteros P, Alvarez J. Cerdan S Gillies RJ. Imaging of extracellular pH of tumors using 1H MRSI. *Magnetic Resonance in Medicine,* 41: 743-750, 1999. **Appendix #6.**

## Progress in Year 4

In Year 4 we completed our comprehensive characterization of vascular patterns for three human breast cancer cell lines, MDA-MB-435, MDA-MB-231 and MCF-7 inoculated in the mammary fat pad of SCID mice. Parallel studies were performed to evaluate the invasiveness of these cells lines in an MRI based matrigel assay. VEGF levels secreted by cells and solid tumors was characterized. We also assayed the spontaneous and experimental metastasis from these tumors models by examining lung sections stained with hematoxylin and eosin for metastatic nodules. Details of these studies can be found in the following published manuscript which is included as an appendix.

Bhujwalla, Z. M., Artemov, D., Natarajan, K., Ackerstaff, E., and Solaiyappan, M. Vascular Differences Detected by MRI for Metastatic *versus* Nonmetastatic Breast and Prostate Cancer Xenografts. *Neoplasia*, Vol.3, pp 143-153, 2001. *(Front cover).* **Appendix #7.**

## Progress during the no-cost extension period

During the no-cost extension period we have made progress in two important areas. First we realized that our separate studies had demonstrated that the metastatic phentotype was characterized by typical metabolic and vascular characteristics. Specifically we have observed that the malignant and metastatic phenotype is characterized by high total choline, high lactate and low extracellular pH and high permeability. For the first time by using a multi-parametric approach of combined vascular and spectroscopic imaging, we are evaluating which combinations of vascular and metabolic/physiological regions in a solid tumor represent the highest 'metastatic threat'. A combined MRI/MRS approach of acquiring metabolic, extracellular pH and vascular images from the same localized regions within a solid tumor will provide further understanding of the dynamics between these parameters and their role in cancer invasion and metastasis.

*Combined pH imaging and Vascular Imaging of Solid Tumors*
*In vivo* imaging of pHe was performed as described in van Sluis et al [15] using the imidazolic pHe marker IEPA. Briefly, localized $^1$H spectroscopic imaging was performed on a GE Omega 4.7T spectrometer with the BASSALE pulse sequence [16] as described above with TE/TR=32/1000, NS=6, and sweep width of 6000 Hz within 30 min. Images of pHe were generated from the SI [15] zero-filled once in the spatial dimensions for an effective resolution of 1 mm x 1 mm x 4 mm.

**Figure 1.** 3-dimensional reconstructed maps obtained from a single MDA-MB-231 tumor (460 mm3) of (a) MRI map of vascular volume (range 0 to 200 μl/g); (b) MRI map of vascular permeability (range 0 to 7 μl/g-

min); (c) Fused map of vascular volume and permeability; (d) Fused map of vascular volume, permeability and pHe (range from 5.3 to 7.2); (e) Hematoxylin and eosin stained histological sections. Spatial resolutions of the vascular volume and permeability maps are 0.125 mm in-plane with 1 mm slice thickness. The pHe map was obtained with a spatial resolution of 1 mm x 1 mm x 4mm.

After spectroscopic imaging, multi-slice relaxation rates ($T_1^{-1}$) of the tumor were obtained as described above for 4 slices matching the SI data set (slice thickness of 1 mm). Maps of vascular volume and permeability were obtained as described earlier. Both SI and vascular maps were obtained during a single experiment without disturbing the position of the animal or the tumor in the coil.

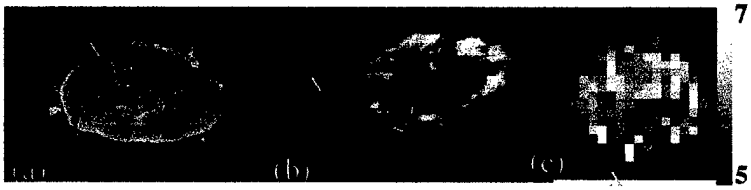


**Figure 2** : Triplanar views of 3D reconstructed data sets of (a) H&E stained sections (b) combined color maps of vascular volume, permeability and extracellular pH and (c) map of extracellular pH. x marks the orientation of the capillary.

We have generated color maps of vascular volume (red), permeability (green) and pHe (blue) and displayed an integrated image of all three parameters (Figure 1 and 2). The combined color map generated provides a visual display of the relationship between pHe and vascular characteristics.

Thus, for example, regions of high vascular volume and high pHe appear as magenta while regions of high permeability and high pHe appear as cyan. High vascular volume, permeability and pHe would appear white. Our preliminary data suggest that there is some overlap of regions of high vascular volume and high pHe. In addition, pHe values in necrotic areas appear to be very acidic (5.8 to 6.0). 3D reconstructed views of hematoxylin and eosin stained sections obtained from this tumor demonstrate extensive necrosis within the central region of the tumor (Figure 1e and 2a).

In future studies the relationship between the individual parameters (vascular volume, vascular permeability, total choline, lactate/lipid, extracellular pH and hypoxia) and metastatic outcome will first be evaluated separately. Depending upon the trends we observe in the separate evaluations, we will evaluate the combinations of those parameters in the co-registered data sets. Shown in Figure 3 are examples of analyses we have developed and performed for spatially co-registered maps of vascular volume, permeability and extracellular pH. Parametric maps of vascular volume, permeability and pHe obtained from the voxels of metastatic (MDA-MB-231) and non-metastatic tumor models (MCF-7) were used to generate three dimensional volumetric histogram matrices. The metastatic and nonmetastatic tumor data are displayed in red and green respectively.

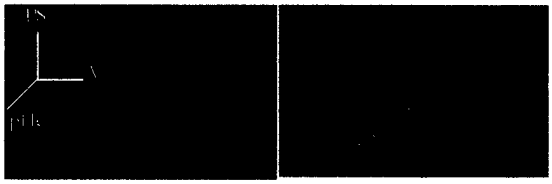

**Figure 3:** Three dimensional volumetric density maps generated from grouped voxels for a metastatic tumor model (MDA-MB-231, red) and a non-metastatic tumor model (MCF-7, green). Vascular volume (V) is displayed along the x-axis, permeability (PSP) along the y-axis, and pHe along the z-axis. The density of the histogram map is displayed as the intensity of the color.

This display extends the conventional histogram plot to a volumetric histogram. Each voxel in the 3D display corresponds to an entry in a three dimensional matrix of vascular volume, permeability and pHe. The x-axis of the table represents vascular volume, the y-axis represents permeability and

the z-axis represents pHe. The intensity of color of the voxel represents the frequency of occurrence (histogram count) of the entry from the sampled data set. Differences between the multi-parametric voxel distributions for the two tumor models were detected in these preliminary studies. These differences can also be visualized by overlaying the red and green volumetric histograms. These histogram maps confirm previous observations that vascular volume and permeability is higher for MDA-MB-231 tumors compared to MCF-7 tumors [17]. Also confirmed are previous observations that, within individual voxels, regions of high vascular volume exhibit low permeability and *vice versa* [17]. The MDA-MB-231 tumors also show a trend of a higher histogram intensity of voxels with high vascular volume and high pHe and high permeability and high pHe compared to MCF-7 tumors. To visualize these relationships we can also generate color maps of vascular volume (red), permeability (green) and pHe (blue) and display an integrated image of all three parameters. The combined color map generated provides a visual display of the relationship between pHe and vascular characteristics. Thus, for example, regions of high vascular volume and high pHe appear as magenta while regions of high permeability and high pHe appear as cyan. High vascular volume, permeability and pHe would appear white.

Details of these studies will be published in the following two manuscripts which are currently in press.

> Bhujwalla, Z.M., Artemov, D., Ballesteros, P., Cerdan, C., Gillies, R.J. and Solaiyappan, M. Combined vascular and extracellular pH imaging of solid tumors. *NMR in Biomedicine*, (in press) 2001. Special Issue on Angiogenesis, Editor: Kevin Brindle.
>
> Bhujwalla, Z.M., Artemov, D., Aboagye, E., Ackerstaff, E., Gillies, R.J., Natarajan, K. and Solaiyappan, M. The Physiological Environment in Cancer Vascularization, Invasion and Metastasis. Novartis Foundation Symposium 240. Published by John Wiley and Sons, October 2001 (No. 0471 49959 5).

During the no cost extension period we also performed studies to alter tumor vascular characteristics using the implantation of slow release VEGF pellets. Shown in Figure 4 are multi-slice maps of vascular permeability obtained from an MDA-MB-231 tumor.

A slow release VEGF pellet (1.6 micrograms over 21 days) pellet manufactured using a stabilizer matrix supplied by Innovative Research of America (Sarasota, Florida) was transplanted adjacent to the tumor. In a study on four tumors with a VEGF pellet and five control tumors with a placebo pellet, we observed that the tumors with a VEGF pellet demonstrated increased permeability in a localized region adjacent to the pellet. Example of images and maps of vascular permeability obtained from a VEGF pellet tumor are shown in Figures 4 and 5.

Maps of vascular permeability from a tumor with a VEGF pellet transplanted adjacent to it are shown in Figure 4. These maps were obtained at day 3 after insertion of the pellet. The location of the pellet in this animal is shown by the arrows in the corresponding high resolution images (Figure 5) obtained at the end of the vascular imaging studies of this animal. The high resolution images and the vascular permeability maps are from the entire cross sectional region of the animal, and the lung cavity is evident in the high resolution images. The tumor is marked by the box in Figures 4 and 5.

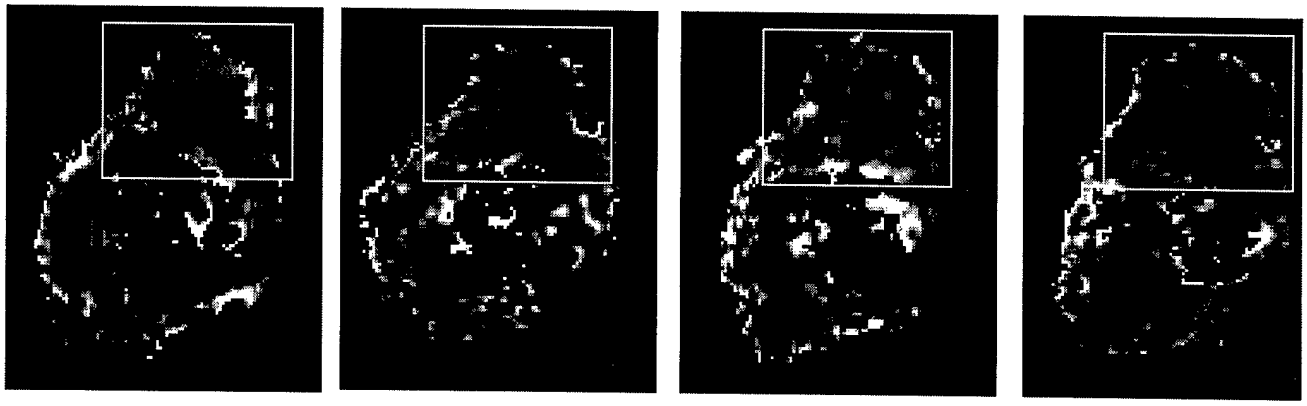

**Figure 4:** Multi-slice maps of vascular permeability obtained from an MDA-MB-231 tumor (tumor volume 380 mm3) in the mammary fat pad. Maps were obtained as described in Bhujwalla et al, Neoplasia, 2001. The vascular permeability maps were obtained from four 1 mm thick slices (in-plane resolution 0.125 mm). The box marks the region of the tumor. The location of the VEGF pellet is shown in Figure 5. Increased permeability was detected in a localized region near the pellet Permeability values ranged from 0 to 33.5 ul/gm-min.

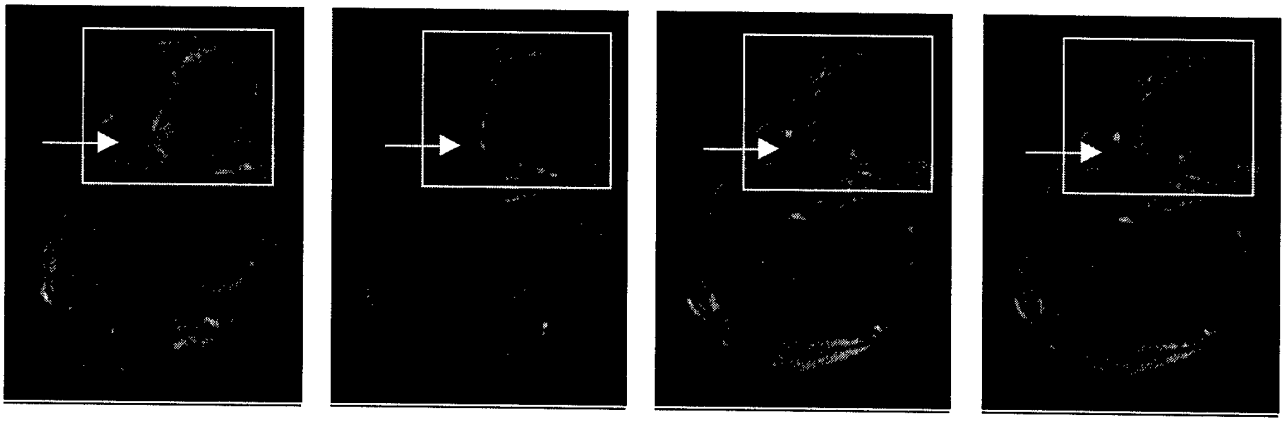

**Figure 5**: High resolution cross-sectional images obtained from a mouse with a MDA-MB-231 tumor in the mammary fat pad (same animal as in Figure 4). The box marks the tumor region. The arrow marks the location of the VEGF pellet. The lungs, which appear as a dark cavity, can be observed in the images. These images were obtained at the end of the albumin-GdDTPA study.

These results demonstrate the feasibility of altering tumor vascular characteristics and detecting them noninvasively by MRI. In future studies, we will make VEGF overexpressing breast cancer cell lines instead of using slow release pellets as this will result in a more uniform distribution of VEGF within the tumor.

To conclude, we have addressed all the technical objectives within the statement of work of the grant. These studies have resulted in the publication of 12 manuscripts and the presentation of 14 abstracts at national and international meetings. The insights we have obtained from these studies have led to new lines of investigation leading to the award of 3 R01's and one P20 from the NIH and one Komen Grant.

**KEY RESEARCH ACCOMPLISHMENTS:**

The major findings to emerge from the research studies funded by this grant are :

• NMR spectra of primary tumors in SCID mice revealed a dramatic and consistent difference in the phospholipid composition of control and transgene tumors formed by derivatives of MDA-MB-435 human breast carcinoma cells transfected with nm23 constructs. Significant differences in intra and extracellular pH were also detected for solid tumors derived from these lines. This was one of the first *in vivo* observations to link the activity of a putative metastasis suppressor gene to metabolic processes. The data also demonstrate the potential of noninvasive NMR spectroscopy to detect forms of gene therapy which may involve transfection of cells with nm23.

• Choline phospholipid metabolite levels progressively increased in cultured HMEC as cells become more malignant. We therefore propose that carcinogenesis in human breast epithelial cells results in progressive alteration of membrane choline phospholipid metabolism. This work is relevant to diagnosis of breast cancer and also provides a rationale for selective pharmacological intervention.

• Lactate levels increase significantly in cultured HMEC following malignant transformation. However, following malignant transformation, there did not appear to be a close dependence between lactate levels observed in malignant cell lines and the metastatic potential of these lines. The increased lactate production may result in an acidic environment which may promote invasive behavior and contribute to metastasis.

• 3-dimensional interactive analysis of vascular volume and permeability and histological morphology demonstrates that areas of low vascular volume are associated with cell death and increasingly permeable vasculature. Regions of high vascular volume and high vascular permeability do not coincide spatially. These findings imply that in addition to previously proposed mechanisms of high tumor interstitial pressure, the delivery of macromolecular agents to the tumor interstitium may also be limited by the lower permeability of tumor vasculature in precisely those viable vascular areas where they necessarily should be delivered for effective treatment.

• The more metastatic cell lines are characterized by higher vascular volume and vascular permeability *in vivo* for analysis performed for regions of high vascular volume and permeability. Cancer cells expressing both high invasive and angiogenic capacity represent the most lethal phenotype. The results indicate a potential use of MRI for evaluating 'metastatic risk' noninvasively.

• Development of combined vascular and metabolic imaging to determine which specific combinations of vascular and metabolic characteristics are most permissive for metastasis to occur from solid tumors.

• Implantation of a slow release VEGF pellet adjacent to tumor, and determination of its effect on vascular permeability.

## REPORTABLE OUTCOMES

Peer reviewed manuscripts

1. Aboagye, E. and Bhujwalla, Z. M. Malignant Transformation Alters Membrane Phospholipid Metabolism of Human Mammary Epithelial Cells. *Cancer Research,* 59, 80-84, 1999.

2. van Sluis R, Bhujwalla Z, Raghunand N, Ballesteros P, Alvarez J. Cerdan S Gillies RJ. Imaging of extracellular pH of tumors using 1H MRSI. *Magnetic Resonance in Medicine,* 41: 743-750, 1999.

3. Bhujwalla, Z. M., Aboagye, E. O., Gillies, R. J., Chacko, V. P., Mendola, C. E., Backer, J. M. Nm23-transfected MDA-MB-435 human breast carcinoma cells form tumors with altered phospholipid metabolism and pH. A $^{31}$P NMR study *In vivo* and *In vitro. Magnetic Resonance in Medicine,* 41: 897-903, 1999 .

4. Aboagye, E. O., Dillehay, L. E., Bhujwalla, Z. M., Lee, D-J. The hypoxic cytotoxin tirapazamine induces acute changes in tumor energy metabolism and pH: A 31P Magnetic Resonance Spectroscopy Study. *Radiation Oncology Investigations,* 6: 249-254, 1998.

5. Aboagye, E., Artemov, D., Senter, P. D. and Bhujwalla, Z. M. Intratumoral Conversion of 5-Fluorocytosine to 5-Fluorouracil by Monoclonal Antibody-Cytosine Deaminase Conjugates: Noninvasive detection of prodrug activation by Magnetic Resonance Spectroscopy and Spectroscopic Imaging. *Cancer Research,* 58, 4075-4078, 1998.

6. Aboagye, E., Mori, N., and Bhujwalla, Z. M. Effect of Malignant Transformation on lactate levels of Human Mammary Epithelial Cells. *Advances in Enzyme Regulation*, Vol.41, pp 251-260, 2001.

7. Bhujwalla, Z. M., Artemov, D., Natarajan, K., Ackerstaff, E., and Solaiyappan, M. Vascular Differences Detected by MRI for Metastatic *versus* Nonmetastatic Breast and Prostate Cancer Xenografts. *Neoplasia*, Vol.3, pp 143-153, 2001. *(Front cover)*

8. Bhujwalla, Z.M., Artemov, D., Ballesteros, P., Cerdan, C., Gillies, R.J. and Solaiyappan, M. Combined vascular and extracellular pH imaging of solid tumors. *NMR in Biomedicine*, (in press) 2001. Special Issue on Angiogenesis, Editor: Kevin Brindle.

Review article

9. Gillies, R. J., Bhujwalla, Z. M., Evelhoch, J., Garwood, M., Neeman, M., Robinson, S. P., Sotak, C. H., van der Sanden, B. Applications of Magnetic Resonance in Model Systems I: Tumor Biology and Physiology. *Neoplasia,* 2(1):1-14, 2000.

Invited Review

10. Bhujwalla, Z. M., Artemov, D., Glockner, J. Tumor angiogenesis, vascularization and contrast enhanced MRI. *Topics in Magnetic Resonance Imaging,* 10(2):92-103, 1999.

11. Bhujwalla, Z. M., Artemov, D., Solaiyappan, M. Insights into Tumor Vascularization using Magnetic Resonance Imaging and Spectroscopy. *Experimental Oncology*, Vol. 22, pp 3-7, 2000.

Symposium Proceedings

12. Bhujwalla, Z.M., Artemov, D., Aboagye, E., Ackerstaff, E., Gillies, R.J., Natarajan, K. and Solaiyappan, M. The Physiological Environment in Cancer Vascularization, Invasion and Metastasis. Novartis Foundation Symposium 240. Published by John Wiley and Sons, October 2001 (No. 0471 49959 5).

Presentations at National and International Meetings (abstracts published in meeting Proceedings)

1. Artemov, D., Bhujwalla, Z.M. 3-dimensional MRI quantitation of tumor vascular volume and permeability. Fifth Annual Meeting, International Society of Magnetic Resonance in Medicine, Vancouver, April, 1997.

2. Gillies, R.J., Raghunand, N., Bhujwalla, Z.M., Ballesteros, P., Alvarez, J., Cerdan, S. Measurement of extracellular pH in tumors by $^{1}H$ MRSI. Fifth Annual Meeting, International Society of Magnetic Resonance in Medicine, Vancouver, April, 1997.

3. Aboagye, E.O., Dillehay, L.E., Bhujwalla, Z.M., Lee, J.D. "Effects of tirapazamine on the energy metabolism of RIF-1 tumors" 1998, Session II-31. $9^{th}$ International Conference on Chemical Modifiers of Cancer Treatment, Clearwater, 1998.

4. Aboagye, E.O., Bhujwalla, Z.M., Gillies, R.J., Mendola, C.E., Backer, J.M. "Nm23-Transfected MDA-MB-435 human breast carcinoma cells form tumors with altered phospholipid metabolism and pH. A $^{31}P$ NMR study in vivo and in vitro" $89^{th}$ Annual Meeting of the American Association for Cancer Research, New Orleans, 1998.

5. Aboagye, E.O., Bhujwalla, Z.M. "The Choline phospholipid resonances as tumor markers in mammary epithelial cells: underlying mechanisms" Sixth Annual Meeting, International Society for Magnetic Resonance in Medicine, Sydney, April, 1998.

6. Aboagye, E.O., Artemov, A., Senter, P.D., Bhujwalla, Z.M. "Tumor selective drug activation by monoclonal antibody-cytosine deaminase conjugates monitored by magnetic resonance spectroscopy and spectroscopic imaging" Sixth Annual Meeting, International Society for Magnetic Resonance in Medicine, Sydney, April, 1998.

7. Bhujwalla, Z.M., Aboagye, E.O., Gillies, R.J., Mendola, C.E., Barker, J.M. "Nm23-transfected MDA-MB-435 human breast carcinoma cells form tumors with altered phospholipid metabolism and pH. A $^{31}$P NMR study in vivo and in vitro". Sixth Annual Meeting, International Society for Magnetic Resonance in Medicine, Sydney, April, 1998.

8. van Sluis, R, Bhujwalla, Z.M., Raghunand, N., Ballesteros, P., Alvarez, J., Cerdan, S., Gillies, R.J. "Imaging of extracellular pH using $^{1}$H MRSI". Sixth Annual Meeting, International Society for Magnetic Resonance in Medicine, Sydney, April, 1998.

9. Solaiyappan, M., Artemov, D. and Bhujwalla, Z.M. Functional Correlation of 3-Dimensional MRI Maps of Tumor Vascular Volume and Permeability with 3-Dimensional Histological Morphology. Sixth Annual Meeting, International Society for Magnetic Resonance in Medicine, Sydney, April-May 1998.

10. Bhujwalla, Z.M., Aboagye, E.O., Mori, N., Chacko, V.P., Artemov, D. and Pilatus, U. "The anti-inflammatory agent indomethacin increases phosphodiester levels in human breast cancer cells". ISMRM Workshop on Magnetic Resonance in Exp. and Clinical Cancer Research, St. Louis, Missouri, 1998.

11. Aboagye, E.O., Bhujwalla, Z.M. "Characterization of lactate in normal and malignant Human mammary epithelial cells". Seventh Scientific Meeting and Exhibition of the International Society of Magnetic Resonance in Medicine, Philadelphia, May 1999.

12. Bhujwalla, Z.M., Artemov, D., Solaiyappan, M., Mao, D., Backer, J.P. Comparison of vascular volume and permeability for tumors derived from metastatic human breast cancer cells with and without the metastasis suppressor gene nm23. Seventh Scientific Meeting and Exhibition of the International Society of Magnetic Resonance in Medicine, Philadelphia, May 1999.

13. Artemov, D., Solaiyappan, M., Bhujwalla, Z.M. 3-dimensional interactive registration of MR images and histological data. Seventh Scientific Meeting and Exhibition of the International Society of Magnetic Resonance in Medicine, Philadelphia, May 1999.

14. Aboagye, E.O., Mori, N., Pilatus, U., Artemov, D., Chacko, V.P., Bhujwalla, Z.M., "Alteration of phospholipid metabolism in human breast cancer cells by the anti-inflammatory agent indomethacin". Proceedings of the 90$^{th}$ Annual Meeting of the American Association for Cancer Research, Philadelphia, 1999.

Funding awarded based on work supported by this award

***NIH (Bhujwalla, Z.M., P.I.)*** ***04/01/97-03/31/01***
1 R01 CA73850 (no cost extension till 02)

*'Functional Imaging of the Metastatic Phenotype' In vivo* and perfused cell studies to determine the role of physiological environment and vascularization in the metastatic spread of prostate

cancer. This grant was recently reviewed for competitive renewal and received a percentile score of 1.7.

***NIH (Bhujwalla, Z.M., P.I.)*** ***07/01/99-06/30/04***
1 R01 CA82337-01
*'Hostile Environments Promote Invasion and Metastasis'*
The aim of these studies is to identify the interaction between the physiological environment and inflammatory signaling and vascularization in breast cancer invasion and metastasis and the ability of anti-inflammatory agents to prevent invasion and metastasis.

***NIH (Bhujwalla, Z. M., P.I.)*** ***03/01/00-02/28/03***
1 P20 CA86346

*'Multidisciplinary Functional Imaging of Cancer'*
This application was funded to establish a 'Pre-In vivo Cellular and Molecular Imaging Center'

***NIH (Bhujwalla, Z.M., P.I.)*** ***04/01/01 – 03/31/04***
1 R01 CA90471

*'Imaging Lymphatic Clearance in Tumor Metastasis'* This application, written in collaboration with Dr. Michal Neeman (P.I. subcontract, Weizmann Institute), is to understand the role of lymphangiogenesis in breast cancer metastasis.

***Completed Projects***
***Komen Foundation (Bhujwalla, Z.M., P.I.)*** ***03/01/98-02/28/00***

*'Functional Imaging of Breast Cancer Progression to the Metastatic Phenotype.'*
*In vivo* and cellular studies to understand the role of the physiological environment and vascularization in breast cancer cell invasion and metastasis using human breast cancer lines *in vitro* and transplanted in SCID mice.

## CONCLUSIONS

The results obtained demonstrate that there are significant differences in vascular characteristics between the metastatic and non or less metastatic lines. High vascular volume and high vascular permeability characterized the most metastatic breast cancer line. The non metastatic human breast cancer line MCF-7 exhibited a lower vascular volume as well as lower vascular permeability. Results from studies with poorly invasive MCF-7 cells transfected to overexpress the angiogenic factor FGF-1 demonstrate that angiogenic capability alone does not determine the metastatic end-point [35]. Thus, cancer cells expressing both high invasive and angiogenic capacity represent the most lethal phenotype.

It is essential to characterize the vasculature of the regions of high vascular volume or permeability, since the significance is less apparent when averaging the measurements over the entire tumor. This demonstrates the necessity of techniques which can detect vascular characteristics with spatial information.

Regions of high vascular volume and high vascular permeability do not coincide spatially within the same tumor. Regions of low vascular volume were usually associated with foci of necrosis in the histological sections. High permeability was related to a higher expression of VEGF. These findings imply that in addition to previously proposed mechanisms of high tumor interstitial pressure [29, 30] the delivery of macromolecular agents to the tumor interstitium may also be limited by the lower permeability of tumor vasculature in precisely those viable vascular areas where they necessarily should be delivered for effective treatment.

Preliminary studies using combined vascular and extracellular pH imaging suggest that there are specific combinations of vascular and metabolic regions which are most permissive for metastasis to occur.

Preliminary studies of transplantation of a slow release VEGF pellet adjacent to a tumor results in a very localized increase of vascular permeability but does not alter overall vascular characteristics or tumor growth significantly.

## REFERENCES


1. Weiss L, and Ward PM (1983). Cell detachment and metastasis. *Cancer Metastasis Rev* **2**, 111-127.
2. Meyer T, and Hart IR (1998). Mechanisms of tumour metastasis. *Eur J Cancer* **34**, 214-221.
3. Melnyk O, Shuman MA, and Kim KJ (1996). Vascular endothelial growth factor promotes tumor dissemination by a mechanism distinct from its effect on primary tumor growth. *Cancer Res* **56**, 921-924.
4. Weidner N, Semple JP, Welch WR, and Folkman J (1991). Tumor angiogenesis and metastasis--correlation in invasive breast carcinoma. *N Engl J Med* **324**, 1-8.
5. Horak ER, Leek R, Klenk N, LeJeune S, Smith K, Stuart N, Greenall M, Stepniewska K, and Harris AL (1992). Angiogenesis, assessed by platelet/endothelial cell adhesion molecule antibodies, as indicator of node metastases and survival in breast cancer. *Lancet* **340**, 1120-1124.
6. Folkman J (1997). Angiogenesis and angiogenesis inhibition: an overview. *Exs* **79**, 1-8.
7. Nicosia RF (1998). What is the role of vascular endothelial growth factor-related molecules in tumor angiogenesis? [comment]. *Am J Pathol* **153**, 11-16.
8. Senger DR, Van de Water L, Brown LF, Nagy JA, Yeo KT, Yeo TK, Berse B, Jackman RW, Dvorak AM, and Dvorak HF (1993). Vascular permeability factor (VPF, VEGF) in tumor biology. *Cancer Metastasis Rev* **12**, 303-324.
9. Shweiki D, Neeman M, Itin A, and Keshet E (1995). Induction of vascular endothelial growth factor expression by hypoxia and by glucose deficiency in multicell spheroids: implications for tumor angiogenesis. *Proc Natl Acad Sci U S A* **92**, 768-772.
10. Plate KH, Breier G, Weich HA, and Risau W (1992). Vascular endothelial growth factor is a potential tumour angiogenesis factor in human gliomas in vivo. *Nature* **359**, 845-848.
11. Jensen JA, Hunt TK, Scheuenstuhl H, and Banda MJ (1986). Effect of lactate, pyruvate, and pH on secretion of angiogenesis and mitogenesis factors by macrophages. *Lab Invest* **54**, 574-578.
12. Rozhin J, Sameni M, Ziegler G, and Sloane BF (1994). Pericellular pH affects distribution and secretion of cathepsin B in malignant cells. *Cancer Res* **54**, 6517-6525.
13. Kato Y, Nakayama Y, Umeda M, and Miyazaki K (1992). Induction of 103-kDa gelatinase/type IV collagenase by acidic culture conditions in mouse metastatic melanoma cell lines. *J Biol Chem* **267**, 11424-11430.
14. Kato Y, Ozono S, Shuin T, and Miyazaki K (1996). Slow induction of gelatinase B mRNA by acidic culture conditions in mouse metastatic melanoma cells. *Cell Biol Int* **20**, 375-377.
15. van Sluis R, Bhujwalla ZM, Raghunand N, Ballesteros P, Alvarez J, Cerdan S, Galons JP, and Gillies RJ (1999). In vivo imaging of extracellular pH using 1H MRSI. *Magn Reson Med* **41**, 743-750.
16. Shungu DC, and Glickson JD (1994). Band-selective spin echoes for in vivo localized 1H NMR spectroscopy. *Magn Reson Med* **32**, 277-284.
17. Bhujwalla ZM, Artemov D, Natarajan K, Ackerstaff E, and Solaiyappan M (2001). Vascular differences detected by MRI for metastatic versus nonmetastatic breast and prostate cancer xenografts. *Neoplasia* **3**, 143-153.

*Topics in Magnetic Resonance Imaging*
**10**(2): 92–103


Review

# Tumor Angiogenesis, Vascularization, and Contrast-Enhanced Magnetic Resonance Imaging

Zaver M. Bhujwalla, Ph.D., Dmitri Artemov, Ph.D., and James Glockner, M.D., Ph.D.

**Summary:** Angiogenesis, the process by which new blood vessels are generated, occurs during wound healing, in the female reproductive system during ovulation and gestation, and during embryonic development. The process is carefully controlled with positive and negative regulators, because several vital physiological functions require angiogenesis. The consequences of abnormal angiogenesis are either excessive or insufficient blood vessel growth. Ulcers, strokes, and heart attacks can result from the absence of angiogenesis normally required for natural healing, whereas excessive blood vessel proliferation may favor tumor growth and dissemination, blindness, and arthritis. In this review, the process of angiogenesis and the characteristics of the resulting tumor vasculature are outlined. Contrast-enhanced magnetic resonance imaging techniques that currently are available for basic research and clinical applications to study various aspects of tumor angiogenesis and neovascularization are discussed. **Key Words:** Angiogenesis—Vascularization—Cancer—Contrast-enhanced magnetic resonance imaging.

## BRIEF HISTORICAL PERSPECTIVE OF TUMOR VASCULATURE

Of all the complexities and protean facets that cancer displays, the ability of a colony of cancer cells to recruit, form, establish, and maintain a vascular network is one of the most fascinating. Interest in tumor vasculature has existed since the 1920s and earlier. For instance, in 1907, Goldmann (1) noted that the development of a tumor in the liver, stomach, or any other organ resulted in "chaotic irregularity" of the blood vessels and that a growing tumor exhibited an extensive formation of blood vessels that was most apparent in the zone of proliferation that for infiltrating tumors, is at the periphery. He also observed that necrosis occurred in highly vascularized growths, and he made the unique suggestion that areas of necrosis were "the battlefield on which assailant and defendant both perished." Similarly, it was recognized as early at 1945 by Algire et al. (2) that malignant cells provoked a continued vascular proliferation.

Research through the subsequent decades has only served to further reveal the undeniable importance of tumor vasculature not only for tumor growth and hematogeneous dissemination, but also for cancer therapy. Observations that had a significant impact on the field of radiation therapy were made by Thomlinson and Gray (3) on human specimens of bronchogenic carcinoma in 1955. In histologic sections of bronchogenic carcinoma, necrosis was found to occur at a distance of 160 μm or greater from the nearest vessel. This distance corresponded closely to the diffusion distance calculated by them, where the concentration of oxygen would approach zero. Their observations provided some of the earliest indirect evidence of the existence of hypoxia and hence radioresistant cells in the tumors (4).

Characteristic "hallmarks" of tumor vasculature have emerged from numerous studies, which now span almost a century (for reviews see references 5–7). Notable among

From the Oncology Section, Division of MR Research, Department of Radiology, The Johns Hopkins University School of Medicine, Baltimore, Maryland, U.S.A.

Address correspondence and reprint requests to Dr. Zaver M. Bhujwalla, Oncology Section, Division of MR Research, Department of Radiology, The Johns Hopkins University School of Medicine, Rm 208C Traylor Building, 720 Rutland Avenue, Baltimore, MD 21205, U.S.A.; or zaver@mri.jhu.edu.

these characteristics of tumor vasculature are (1) spatial heterogeneity and chaotic structures; (2) arteriovenous shunts; (3) acutely collapsed vessels and transiently collapsing vessels; (4) poorly differentiated, fragile, and leaky vessels lacking in smooth muscle cell lining; and (5) vasculature that frequently is unable to match the rapid growth of cancer cells, resulting in areas of hypoxia and necrosis. In an influential review, Rubin and Casarett (8) pointed out that although the ability of a tumor cell to survive depends on its distance from the capillary from which essential substrates and oxygen diffuse, necrosis is not always due to absence of vascularization or due to the tumor outgrowing its blood supply, a sentiment first expressed by Goldmann (1) in 1907. Acute vascular collapse due to high tumor interstitial pressure (6,9,10), the immune-related destruction of cells, and the release of toxic agents (11) have been cited as some of the other causes.

Vascular properties of tumors have always been considered important because of their role in the delivery of therapeutic agents, and because radioresistant hypoxic cells may be a potential source of treatment failure following radiation therapy. The recent overwhelming interest in tumor vascularization and angiogenesis, however, has arisen due to two findings. One of these is that high vascular density in histologic specimens may be predictive of the disposition of the tumor to metastasize (12–16). Because angiogenesis is critical for tumor growth, antiangiogenic treatment as well as antineovasculature therapies have been proposed and investigated for cancer treatment (17,18). The second finding, related to antiangiogenic therapy, is that repeated treatment cycles with the angiogenesis inhibitor endostatin induced tumor dormancy without inducing tumor drug resistance in at least three experimental tumor models (19).

## TUMOR ANGIOGENESIS

Although it was recognized from very early on that tumor cells secrete substances to induce vascularization (20), Folkman and his colleagues (21) were the first to isolate a tumor angiogenic factor in 1971. Studies using transgenic mice now suggest a model of tumorigenesis in which mutated oncogenes and tumor repressor genes induce cell proliferation and hyperplasia. There appears to be a secondary set of events after cell proliferation leading from hyperplasia to neoplasia (17,22,23). The induction of angiogenesis is one of the critical events or "switches" in this progression, given that the prevascular phase can persist for years with limited growth of the lesion (23).

Tumor growth to about 1 mm can be accomplished in the absence of neovascularization, because all essential nutrients and waste products can diffuse across this distance; however, once a tumor has reached this threshold stage of growth, vascularization is essential for additional growth and progression (17,22,23). The normal proliferation rate of endothelial cells is very low compared to many other cell types in the body, and the turnover time of these cells can exceed 1,000 days. In contrast, tumor capillary endothelial cells have a potential doubling time of 2.14 to 13 days (24,25).

Tumor cells, as mentioned earlier, have the ability to induce neovascularization through the release of angiogenesis factors (17,22,23). However, not only cancer cells but also inflammatory cells that infiltrate the tumor and the extracellular matrix can be a source of angiogenesis factors (26). Also as mentioned earlier, there are positive and negative regulators of angiogenesis. Several factors have now been identified as angiogenic promoters and angiogenic inhibitors (26), and several of these promoters and inhibitors are listed in Table 1. The phenomenon of tumor angiogenesis begins with the degradation of the basement membrane of the parent vessel by proteases secreted by activated endothelial cells that migrate and proliferate, leading to the formation of solid endothelial cell sprouts into the stromal space in response to the angiogenic factors. Vascular loops are formed and capillary tubes develop, with formation of tight junctions and deposition of new basement membrane (17,22,23,26).

An angiogenic factor that has attracted significant interest is vascular endothelial growth factor (VEGF). Of all the various angiogenesis promoters and inhibitors, VEGF appears to be the most responsive to the abnormal physiological environments of hypoxia, extracellular acidosis, and substrate deprivation that occur in solid tumors (27). Current information on VEGF has been reviewed extensively by Neufeld et al. (28). VEGF induces angiogenesis

**TABLE 1.**

| Angiogenesis promoters | Angiogenesis inhibitors |
|---|---|
| Fibroblast growth factors | Thrombospondin 1 |
| Placental growth factor | Angiostatin |
| Vascular endothelial growth factor | Endostatin |
| Transforming growth factor α | Prolactin 16-kD fragment |
| Transforming growth factor β | Metalloproteinase inhibitors |
| Angiogenin | Platelet factor 4 |
| Interleukin 8 | Genistein |
| Hepatocyte growth factor | Transforming growth factor β (?) |
| Platelet-derived endothelial cell growth factor | Interferon α |
| | Placental proliferin-related protein |
| Angiopoietin 1 | Fumagillol |
| Granulocyte colony-stimulating factor | Retinoids |
| | Protamine |
| Wound fluid | |
| Epidermal growth factor | |
| Tumor necrosis factor α | |
| Prostaglandins | |

(29,30) and is a potent vascular permeability factor (31). There are five isoforms of VEGF (with 121, 145, 165, 189, and 206 amino acids) generated from alternative splicing of the VEGF gene that are distinguishable by their heparin and heparin-surface binding properties, water solubility, and target receptors (28). The various forms of VEGF bind to two tyrosine-kinase receptors (*flt-1*) and (*KDR/flk-1*), which are expressed almost exclusively on endothelial cells. In addition, endothelial cells express neuropilin-1 and neuropilin-2 coreceptors, which bind selectively to the 165 amino acid form of VEGF. Of the various isoforms of VEGF, the 121 and 165 forms predominate, although the 189 form also is found in most VEGF-producing cell types (32). Expression of VEGF-145 is restricted to cells derived from reproductive organs (28). Hypoxia-mediated transcription of VEGF is thought to occur through the binding of the hypoxia-inducible factor 1 (HIF-1$\alpha$) to an HIF-1 binding site located in the VEGF promoter (33). Hypoxia also promotes the stability of VEGF mRNA through binding proteins (34). There appears to be a dependence of VEGF expression on COX-2 and iNOS that is mediated through prostaglandin $E_2$ and nitric oxide (35). Under hypoxic conditions, which are typical for most solid tumors, VEGF expression is regulated by pH and glucose concentration (36,37). VEGF expression also can be modulated by oncogenes (28) and by the tumor suppressor gene p53 (39,40) although results to the contrary have been observed (41).

## SOME ASPECTS OF NON-MAGNETIC RESONANCE BIOASSAYS FOR MEASURING ANGIOGENESIS AND VASCULARIZATION

The most commonly used bioassays for angiogenesis are (1) the developing chick chorioallantoic membrane, (CAM) (2) the corneal pocket assay, and (3) the transparent Millipore chamber model grown in the rabbit ear or hamster cheek pouch (20,42,43). The CAM bioassay is carried out in fertilized chick eggs in which a window is prepared by removal of a section of egg shell or in which the shell is totally removed and the egg cultured in a Petri dish. Test substances are placed onto the chick chorionic membrane of 8- to 10-day-old fertilized chick egg on filters or coverslips. Neovascularization is monitored visually, 1–2 days after implantation, and the membranes are fixed and evaluated histologically. In the rabbit corneal assay, test substances are incorporated into sustained release polymer pellets that are implanted into a surgical pocket prepared in the cornea. With a positive response there is directional growth of new capillaries from the limbal blood vessel toward the implant. The bioassay can be quantified by measuring the rate of vessel growth, as well as the length and the density of the new blood vessels. Angiogenesis in the transparent Millipore chamber is evaluated similarly. These techniques have been used for pioneering studies in angiogenesis, but some of the disadvantages are the limitations on the number of samples that can be assayed and the difficulty in quantifying the results.

The initial angiogenic stimulus results in the formation of tumor neovasculature necessary to establish the solid tumor and deliver substrates and nutrients. Angiogenesis, continues to occur through the life time of the tumor, because new vasculature has to be continually generated with tumor growth. An example of this is shown in Fig. 1. Thus, at any given time in the history of a growing solid tumor, there will be established vasculature and vasculature in the process of being formed. Three quantities, tumor blood flow, tumor vascular volume, and vascular permeability, have mainly been used to characterize tumor vasculature. Several methods are available to measure tumor blood flow quantiatively; however, most of these methods, with the exception of positron emission tomography are either invasive or lack spatial information. The reader is referred to three excellent reviews on measurement and characterization of tumor blood flow (7,27,44).

Some of the earliest measurements of percent vascular volume were obtained by morphometric estimation of vessels in histologic sections (2,45). The functionality of vessels cannot be evaluated in histologic sections, and it may be that a fraction of the vessels is nonfunctional. This may result in a discrepancy between results obtained using morphometric analysis and results obtained using magnetic resonance imaging (MRI) (discussed later), which measures vasculature into which the contrast agent can be delivered. This issue becomes increasingly important as immunoperoxidase staining of molecules such as CD31 and CD34 (46), which are present on the surface of endothelial cells, are used to identify vessels. It also should be mentioned here that in studies that have shown a dependence of metastasis on microvessel density, the analysis usually is performed by identifying the area of highest neovascularization within the section and obtaining microvessel counts in those areas. In the study by Weidner et al. (12), for patients with invasive breast carcinomas with any metastases, the mean microvessel counts for the areas of highest neovascularization were 101 (at 200× field) compared to 45 in carcinoma from patients without metastases. Thus, the number of microvessels in the regions of highest neovascularization determines risk of metastasis. Several macrosopic and microscopic methods of measuring vascular volume have been developed (47) that usually require administration of radioactive tracers and excision of the tumor (48).

Different mathematical formulae have been used to

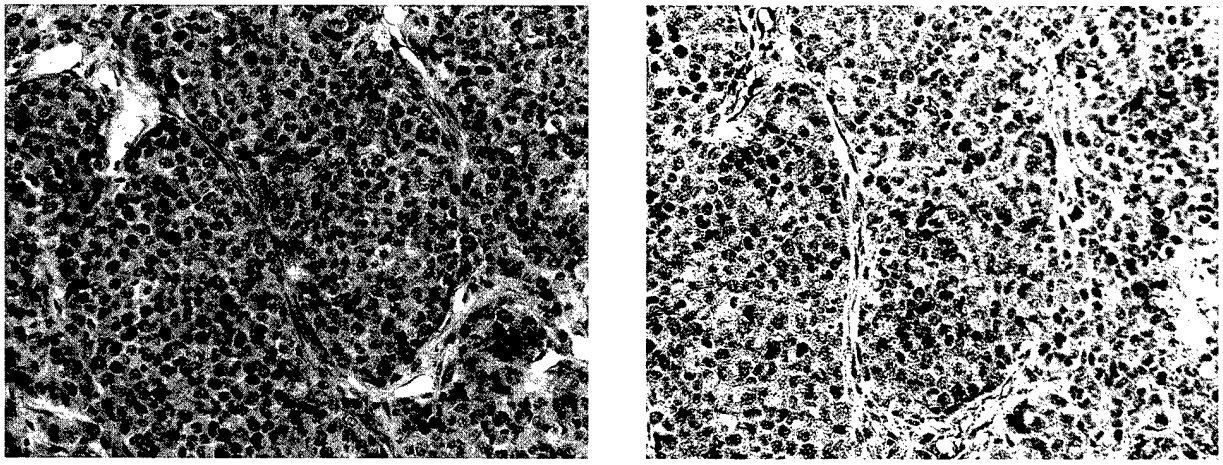


**FIG. 1.** High-power micrograph (×400) of sprouting endothelial cells in two adjacent 5-μm thick sections stained **(A)** with hematoxylin and eosin and **(B)** immunostained for VEGF expression. Sections were obtained from a 10-mm-diameter MDA-MB-231 human breast cancer model growing in the flank of a SCID mouse.

compute vessel permeability (5). Usually an effective "permeability-surface area" product (PS), also referred to as "capillary-diffusion capacity," is obtained by determining the rate of extravasation of the test substance into the tumor. PS values quoted in literature depend on the molecular size of the test substance used; the reader is referred to excellent reviews on tumor vascular permeability (5,48).

## MRI OF ANGIOGENESIS AND VASCULARIZATION

Angiogenesis is a dynamic process. A method to quantitate neovascularization in situ without perturbing or excising the tumor would be useful to examine the temporal relationship between neovascularization and tumor growth and determine the effects of antiangiogenic therapy. A noninvasive method of obtaining an index of vascularization or microvessel density also would be advantageous clinically to (1) determine the effects of preoperative hormonal deprivation on vascularization, (2) determine the aggressiveness of the lesion, and (3) play a role in the selection and monitoring of patients treated with antiangiogenic drugs. MRI is suitable for these purposes because MR images can be obtained noninvasively with an inplane resolution on the order of 100 μm. Vascularization can be evaluated using intrinsic endogenous contrast (49) or with exogenous paramagnetic contrast agents. Gadolinium chelates are the contrast agents frequently used for MRI. These agents are tightly bound complexes of the rare earth element gadolinium (Gd) and various chelating agents. The seven unpaired electrons of Gd produce a large magnetic moment that results in paramagnetic properties when the ion is placed in a magnetic field and creates contrast in an MR image. Paramagnetic agents shorten both T1 (spin-lattice relaxation time ) and T2 (spin-spin relaxation time), but because tissue T2 values are intrinsically short, the T1 effect of the contrast agent predominates; tissues that take up a paramagnetic agent are brightened (positive enhancement). Susceptibility effects of Gd-based contrast agents resulting in enhancement of T2 and T2* relaxation have been used to measure vascular volume and flow in clinical studies in brain (50). These studies have been reviewed elsewhere (51) and are not discussed here because their application to tumors is limited due to leaky vasculature and relatively slow perfusion rate in tumors.

The tissue concentration of Gd-based agents can be calculated from changes in T1 obtained from quantitative T1 maps or T1-weighted images. Several Gd complexes are under development or in use. Low-molecular-weight Gd-DTPA compounds (0.57 kD) are used in clinics for contrast enhancement of various lesions including malignant tumors. Macromolecular contrast agents, such as albumin-(Gd-DTPA), remain in the intravascular space with a half-life of several hours because of their large molecular weight (approximately 65 kD). Thus, analysis of relaxivity changes induced by an intravascular agent can be used to determine blood or vascular volume and vascular permeability (52,53). A novel and promising area is the design of receptor-targeted contrast agents where the re-

sulting contrast is dependent on the density of receptor expression (54). In the following sections we present brief descriptions of current MR methods used to characterize tumor vascularization based on the physical properties of the contrast agent used. Of the three parameters mainly used to characterize tumor vasculature, currently only vascular volume and vascular permeability can be quantified with contrast-enhanced proton imaging. Quantitative blood flow measurements have been obtained using deuterium MRI with $D_2O$ as the blood flow tracer (55,56). A detailed discussion of this technique is beyond the scope of the present review which is restricted to proton imaging.

**Assessment of angiogenesis with gradient-echo MRI**

Detection of tumor vasculature using the intrinsic T2* contrast produced by deoxygenated hemoglobin in tumor capillaries (49) is based on the BOLD technique originally proposed by Ogawa et al. (57) for brain imaging. The functional dependence of T2* is given by Equation 1:

$$1/T2^* \alpha (1 - Y)b, \qquad (1)$$

where $Y$ is the fraction of oxygenated blood and $b$ is the partial vascular or blood volume fraction. In hypoxic tumors where $0 < Y < 0.2$, the contrast produced by the method is primarily dependent on $b$, which permits rapid in vivo determination of vessel densities in tumors. The method works best in poorly oxygenated tumors such as subcutaneous models and human xenografts with random orientation of sprouting capillaries. The technique has been used to detect changes in tumor vascularization following induction of angiogenesis by exogenous angiogenic compounds (49) and to obtain "functional vascular" maps of genetically modified HIF-1 (+/+ and −/−) animal tumor models (58). The method provides fast and truly noninvasive of measurement of tumor vascularization because it does not require injection of contrast agent. However, it cannot provide quantitative measurements of tumor vascular volume, and it cannot measure vascular permeability or blood flow.

**MRI detection of tumor angiogenesis by receptor-targeted contrast agents**

The feasibility of imaging newly formed vasculature in squamous cell carcinoma in rabbits was demonstrated recently by Sipkins et al. (54) using a paramagnetic contrast agent targeted to the endothelial $\alpha_v\beta_3$ integrin. The contrast agent was composed of Gd-labeled polymerized liposomes conjugated with biotinylated antibodies targeted against $\alpha_v\beta_3$ receptors on endothelial cells. A selective enhancement of the tumors was demonstrated without any significant binding of the contrast agent to normal muscle vasculature adjacent to the tumor. The large particle diameter of 300–350 nm provided a prolonged life time of the contrast agent in plasma lasting approximately 8 h, allowing accumulation of the contrast agent at the $\alpha_v\beta_3$ receptors. Image intensity proportional to the density of the receptors was obtained from standard T1-weighted images. The method provides information about the density of neovasculature, but dynamic vascular characteristics such as permeability or flow cannot be measured.

**Low-molecular-weight contrast agents**

Because low-molecular-weight contrast agents are the only class of paramagnetic agents approved for routine clinical use, there are multiple reports describing applications of these agents to image a variety of tumors including breast tumors (59–61), brain tumors (51), and uterine cervical carcinomas (62). Similarly, several theroretical models have been developed to derive and quantify tumor vascular parameters for these agents.

A frequently used theoretical model of analysis for low-molecular-weight contrast agents is that of Tofts (63), which mainly relies on the existence of vascular and interstitial compartments with uniform tracer concentrations within the compartments. The model also assumes that transport of the agent across the capillaary wall is not flow limited. The model ultimately derives influx and outflux transfer constants and extravascular extracellular space. The arterial input function required by the model can be measured separately or defined in real time using voxels localized within large blood vessels. The analytical solution of the model can be derived by approximating the arterial input function to a multiexponential decay as first described by Ohno et al. (64). The concentration of Gd-DTPA is measured from changes in the T1 relaxation rate assuming that water is in fast exchange.

If the flow rate is low and unable to replenish the leak of contrast agent from the vasculature and the extraction fraction of the agent is high, i.e., the fraction of agent leaving the vasculature during a single pass of blood through the tissue is close to 1, which is likely for low-molecular-weight compounds and highly permeable tumors, then only the product of (*blood flow · extraction fraction*) can be defined using the model (65). However, if flow can be measured independently then the extraction fraction (E) and PS can be defined and quantified. Kovar et al. (66) recently used this approach where the freely diffusable tracer $D_2O$ was used to measure flow independently of Gd-DTPA-dimeglumine, which was used to determine the extraction fraction. The method is somewhat restricted by the low sensitivity of deuterium MRI resulting in low spatial resolution and because $D_2O$ cannot be used clinically. Combining MRI with an imaging modality

such as positron emission tomography can provide an alternative approach for quantitative measurements of PS in human tumors.

Another approach, developed by Degani et al. (61), uses a three-time-point method to obtain wash-in and wash-out patterns of the contrast agent. The patterns are displayed as an artificial color map with the intensity and hue of the colors proportional to the patterns. The method is based on the two-compartment flow-independent model proposed by the authors previously (60). In the current version the method is model-free and can be used to differentiate between malignant and benign breast lesions, even for situations where the original kinetic model fails to characterize the contrast uptake curves. The method requires obtaining three T1-weighted maps (one precontrast and two postcontrast) that can be acquired with high spatial resolution. However, using the hue and intensity of the color maps to independently quantify vascular permeability, vascular volume or flow rate currently is not feasible.

**Macromolecular contrast agents**

Quantitative determination of parameters of tumor vasculature with low-molecular-weight contrast agent is complicated by fast extravasation of the contrast agent from leaky capillaries in tumors. The availability of high-molecular-weight contrast agents such as albumin-Gd-DTPA complexes or synthetic compounds such as polylysine-Gd-DTPA and gadomer-17 provides a unique opportunity for quantitative determination of tumor vascular volume and vascular PS for molecules of comparable sizes (52,67) The relatively slow leakage of these agents from the vasculature results in a long half-life time and complete equilibration of plasma concentrations within the tumor independently of blood flow, which in this case is large compared with PS. Assuming fast exchange of water between all the compartments in the tumor (plasma, interstitium, and cells), the concentration of the contrast agent within any given voxel is proportional to changes in relaxation rate (1/T1) before and after administration of the contrast. Relaxation rates can be measured either directly using fast single-shot T1 methods (53) or from T1-weighted steady-state experiments (68) that provide better temporal resolution but are susceptible to experimental artifacts caused by variations in T2 and T2* relaxation times. Pixel-by-pixel maps can be reconstructed from the acquired data and processed with an appropriate model to obtain spatial maps of tumor vascular volume and vascular permeability surface area product.

A simple linear compartment model describing uptake of the contrast agent from plasma postulates a negligible reflux of contrast agent from the interstitium back to the blood compartment. Blood concentrations of the contrast agent can be approximated to be constant for the duration of the MR experiment, and, under these conditions, contrast uptake is a linear function of time (48,69,70). On a plot of contrast agent concentration versus time, the slope of the line provides the parameter PS, and the intersect of the line with the vertical axis at time zero provides vascular volume. For qunatitative determination of these parameters, the change in relaxation rate of the blood also should be quantified. Changes in blood T1 can be obtained separately for blood samples taken before injection of the contrast agent and at the end of the experiment. The method is anaologous to the measurement of vascular volume using radiolabeled proteins, usually $^{125}$I-albumin (48, 69,70). However, as pointed out by Tozer and Morris (71), the invasive method requires excision of the tumor, and there may be a possibility of overestimating vascular volume because the protein may already have extravasated within 2 min usually required for equilibration of the protein within plasma.

A more complex two-compartment model, which takes into account reflux of the contrast agent and changing concentrations of the contrast agent in plasma, was developed by Su et al. (72) and Brasch et al. (68). The model used by Su et al. (72) derives three parameters—vascular volume, vascular permeability, and a reflux constant. Brasch et al. (68) use a simple exponential approximation of clearance of the contrast agent from blood, and their model does not require determining the arterial input function. Five parameters (vascular volume, fractional leakage, reflux rates, the initial concentration of contrast agent in plasma, and the fractional turnover rate or clearance of the contrast agent from blood) can be derived from the nonlinear fitting of tissue concentrations of the contrast agent obtained experimentally. PS can be obtained from the product of (*vascular volume · fractional leakage rate*). Blood concentrations of the contrast agent can be defined from large blood vessels within the field of view of the image (68), serial blood samples collected from an arterial line at different time points (72), or from signal enhancement of reference tissue such as liver (73).

For large macromolecular agents such as albumin Gd-DTPA (molecular weight approximately 65 kD), blood concentrations equilibrate within 2–3 min and do not change for at least 60 min after intravenous bolus injection. Tissue concentrations of the agent for a time period starting 5 min after the bolus required for plasma equilibration and up to 40 min after the bolus increase linearly with time. Therefore, the simple linear model is preferable for analysis of intrinsically noisy relaxation data, because this model is much more more stable in comparison with nonlinear fitting algorithms required for the two-compartment models discussed earlier. Accuracy of mea-

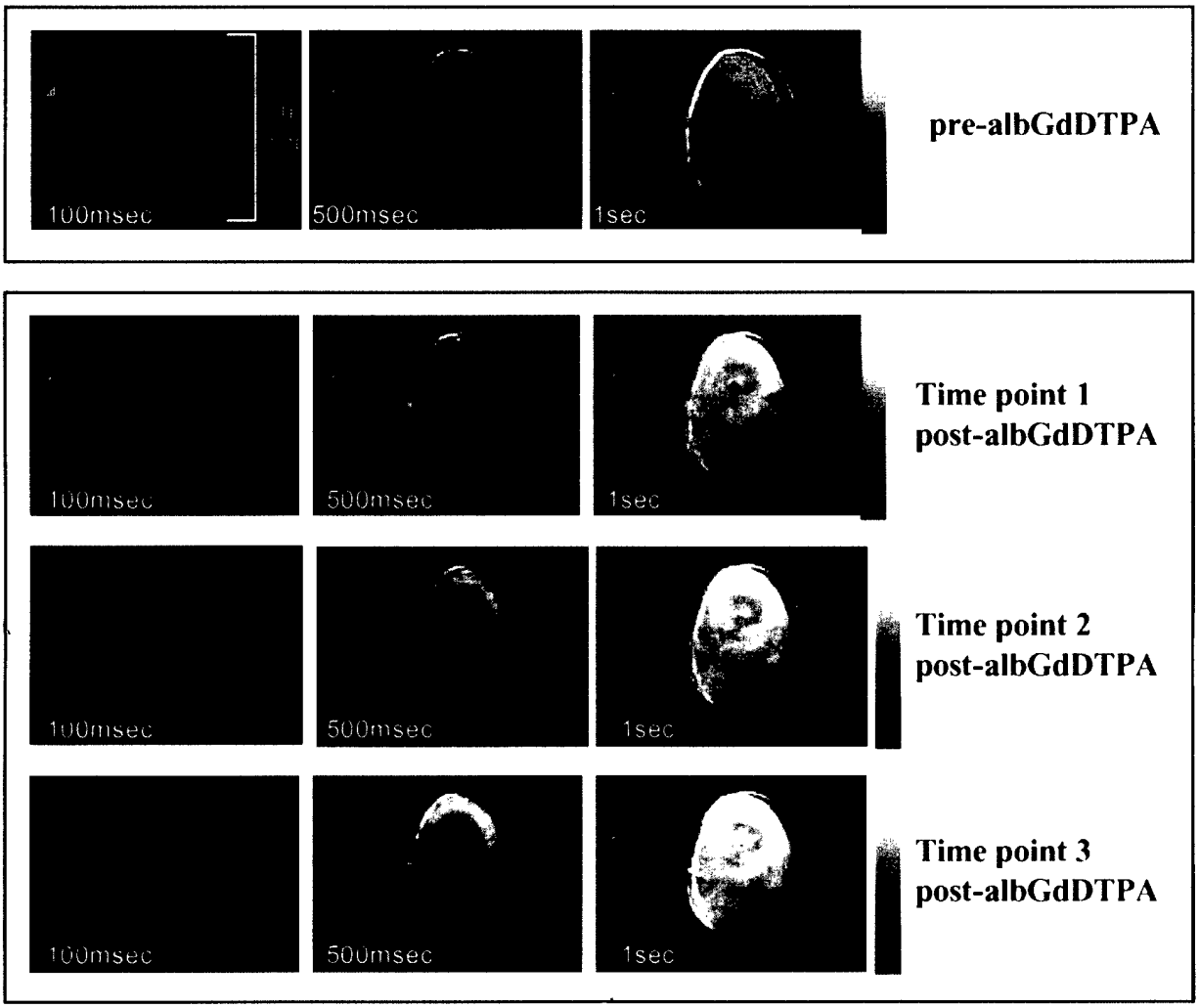


**FIG. 2.** Saturation recovery spin-echo images showing the uptake and distribution of albumin Gd-DTPA in a subcutaneous flank MDA-MB-231 tumor (volume 154 $mm^3$) before and at 18, 34, and 50 min after injection (IV) of albumin-Gd-DTPA. A small glass capillary containing water doped with Gd-DTPA can be observed in the images. Images are displayed for three saturation recovery time intervals (100 ms, 500 ms, 1 sec) for a 700-μm sagittal slice through the center of the tumor (field of view = 16 mm; 128 × 128 matrix; number of averages = 2; sweep width = 20,000; in-plane resolution = 125 μm; repetition time = 100 ms; echo time = 16 ms). Images are displayed scaled so that the capillary intensity is constant in all the images to allow easier comparison of the image intensities.

surement of the tissue vascular volume does depend, however, on the water exchange rate between the vascular and extracellular compartments. Using a simplified model of fast exchange where there may be intermediate-to-slow exchange can lead to significant underestimation of vascular volume. Experimental approaches to minimize these errors are based on observations that the initial slope of the relaxation curve is independent of the exchange rate (74,75).

Large-molecular-weight contrast agents potentially may be used to measure tumor blood flow by detecting the first pass of the agent through tumor vasculature, similar to the method described previously (50,51), although this approach may not be feasible when the heart beat is very rapid, as for rodents. Studies exploring the feasibility of such an approach are yet to be performed.

In our laboratory, we used the dynamic distribution of the intravascular paramagnetic contrast agent albumin-Gd-DTPA to quantitate vascular volume and permeability and related the images obtained to the distribution of VEGF and cell morphology in histologic sections obtained from the imaged slice. Vascular volume and permeability were characterized for two different tumor models (MDA-MB-231 human breast cancer line in severe combined immune deficient (SCID) mice and RIF-1 in C3H mice) with the primary aim of determining the ability

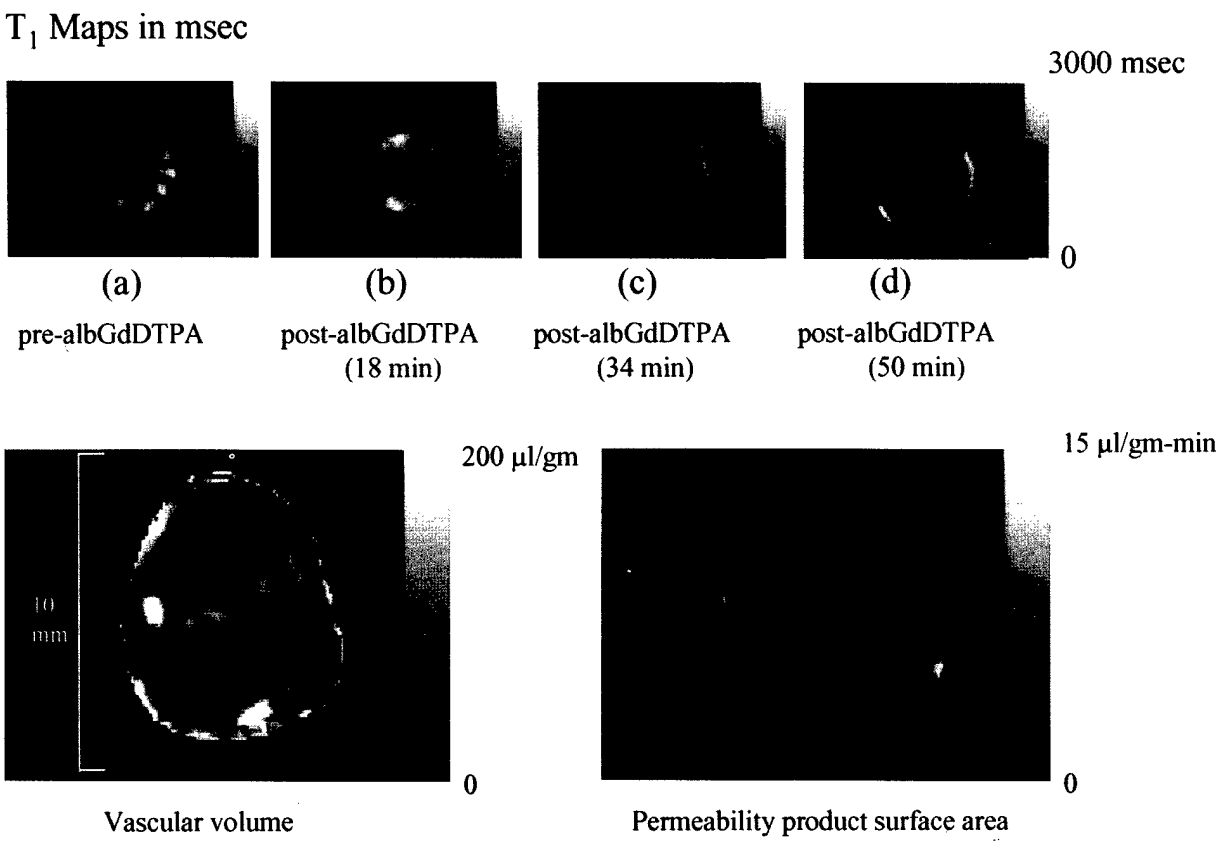


**FIG. 3.** T1 maps and maps of vascular volume and permeability generated from the images shown in Fig. 1. Vascular volume and permeability product surface area (PS) maps were generated from the ratio of Δ(1/T1) values in the images to that of blood using an IDL (Interactive Data Language, Research Systems, Inc., Boulder, CO, U.S.A.) program. The slope of Δ(1/T1) ratios versus time in each pixel was used to compute PS, and the intercept of the line at zero time was used to compute vascular volume. The gray scale is labeled with the minimum and maximum values of vascular volume and permeability.

of the technique to detect differences in these parameters for these two models. Such a technique then may be applied to determine the correlation between vascular volume and permeability for tumors derived from clones with different metastatic capacity. We detected significant differences in vascular volume generated by the MDA-MB-231 breast cancer line compared to the RIF-1 cell line. We also detected significant differences in vascular permeability for MDA-MB-231 tumors growing in the mammary fat pad compared to MDA-MB-231 tumors growing in the flank. These latter results confirm previous observations made for brain tumor cells (76) that the tumor microenvironment can dictate the permeability of the vasculature.

T1 maps were obtained for a 700-µm sagittal slice through the center of the tumor using a progressive saturation recovery technique for saturation recovery time intervals of 100 ms, 500 ms, and 1 sec followed by spin-echo imaging for each phase encoding step. A 0.2-ml bolus of a solution of 60 mg/ml albumin-Gd-DTPA made up in saline was injected through the tail vein (dose of 500 mg/kg). T1 maps were obtained before and for three to five time points after the intravenous injection. At the end of the imaging studies, the animal was sacrificed, 0.5 ml of blood was withdrawn from the inferior vena cava to measure blood T1, and the tumors were excised and fixed in 10% buffered formalin for sectioning and staining. Precontrast blood T1 values were obtained from a separate tumor-bearing group of four SCID and three C3H mice. T1 values of blood collected in a tube were measured using inversion recovery with 10 recovery time points. Five 5-µm-thick, paraffin-embedded histologic sections were obtained from the imaged slice and immunohistochemically stained for VEGF expression (Santa Cruz Biotechnology, Santa Cruz, CA, U.S.A.) (16). Adjacent sections were stained with hematoxylin and eosin for morphologic information.

A representative dataset demonstrating the raw images, obtained in this case for an MDA-MB-231 flank tumor, is shown in Fig. 2. The corresponding T1 maps as well as maps of vascular volume and permeability generated from these images are shown in Fig. 3. Both vascular volume

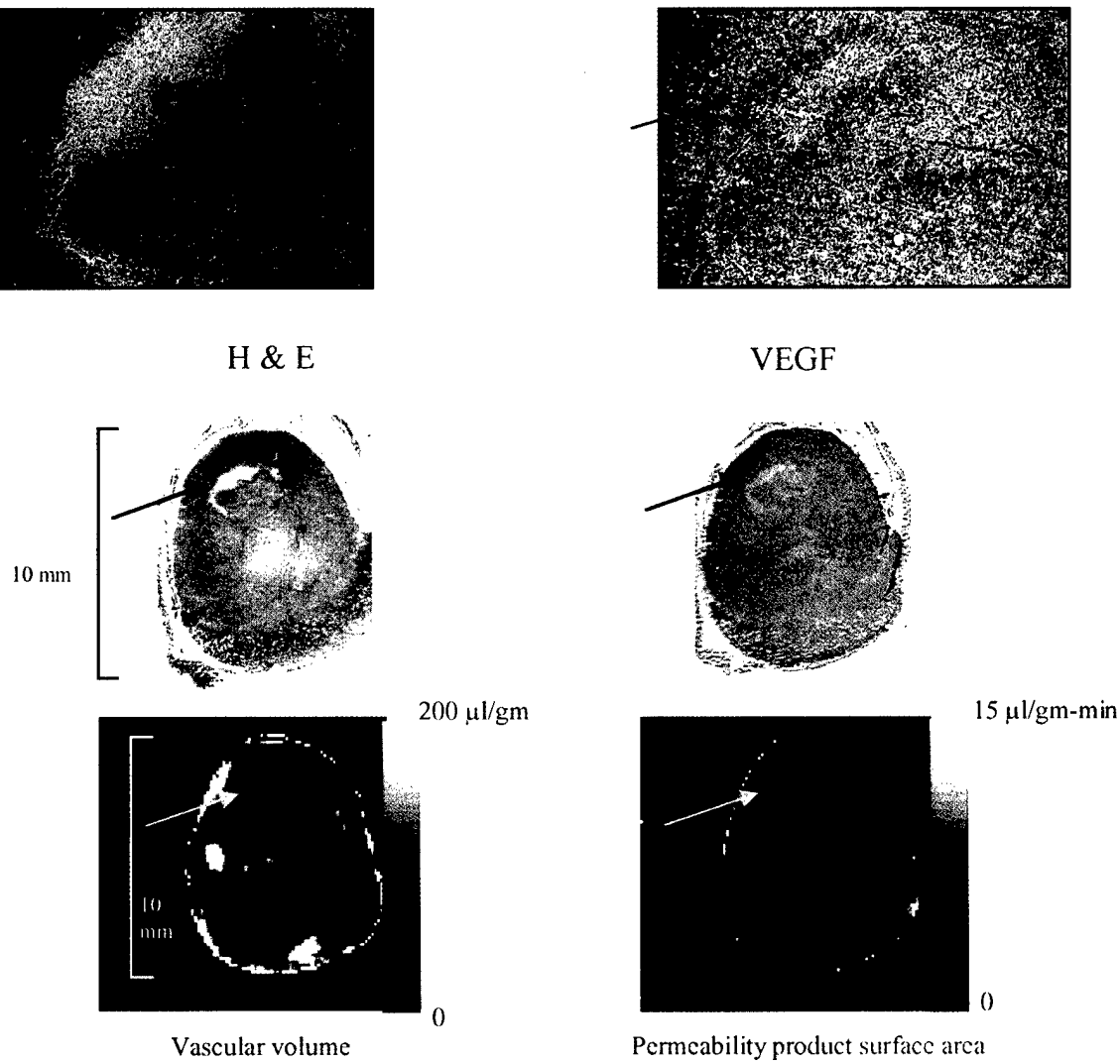


**FIG. 4.** Adjacent 5-µm-thick, histologic sections obtained from the imaged slice in Figs. 2 and 3. The arrow in both sections indicates an area containing necrotic cells. The necrotic area is shown at a higher magnification within the inset of each section. One section is stained with hematoxylin and eosin (section marked H & E in figure); the other section is stained for vascular endothelial growth factor (VEGF) expression using immunoperoxidase staining (section marked VEGF in figure). Regions with an increased brown stain indicate higher levels of VEGF expression. Maps of vascular volume and permeability are included for comparison.

and permeability were spatially heterogeneous, and this was observed for all the tumors examined. Most tumors showed a higher vascular volume around the periphery, which was consistent with the presence of higher vessel density in the histologic sections and consistent with previous observations that peripheral vascularization is one of two basic patterns of tumor vascularization, the other being central vascularization (8). Regions with the highest vascular volume usually did not exhibit high permeability. Two adjacent tumor sections obtained from the imaged slice (shown in Figs. 2 and 3) and stained with hematoxylin and eosin and immunostained for VEGF expression are displayed in Fig. 4 with the corresponding maps of vascular volume and permeability included for comparison. Regions of low vascular volume in the MRI maps frequently contained necrotic foci (see magnified inset in Fig. 4) in the histologically stained sections: the regions corresponding to low vascular volume usually were more permeable, as can be observed by comparing the regions marked by an arrow in Fig. 4. A possible explanation, consistent with the necrotic foci observed in these areas, is that areas with low vascular volume may contain the most leaky and nonfunctional vasculature. VEGF staining was most intense around necrotic areas (see arrow in Fig. 4). A coarse spatial agreement was observed between areas with high VEGF expression in the histologic section and areas

of high permeability observed in the MR images. Vascular volumes of MDA-MB-231 mammary fat pad tumors (46.6 ± 9 μl/g, n = 6) were significantly higher ($p < 0.05$) than RIF-1 tumors (18.7 ± 4 μl/g, n = 4); values represent mean ± 1 SEM. MDA-MB-231 tumor vasculature was significantly ($p < 0.016$) more permeable in the flank (1.64 ± 0.26 μl/g · min, n = 4) compared to the mammary fat pad (0.85 ± 0.13 μl/g · min, n = 6). Despite the lower vascular volume, the volume doubling time of the RIF-1 tumor model was 3 days compared to 14 days for the MDA-MB-231 model, yet RIF-1 tumors at the volumes studied here do not exhibit necrosis. These data demonstrate the complex balance that exists among vascular volume, tumor growth, and necrosis. Cell cycle time, cell loss factor, the rate of dead cell clearance, the ability of cells to generate an angiogenic response, the endothelial cell proliferation rate, the growth fraction, and the energy and oxygen requirements of cells all play a role in this balance (25,77).

## CONCLUSION

The undoubted advantage of contrast-enhanced MRI lies in its ability to obtain vascular parameters noninvasively with in-plane spatial resolutions on the order of 200 μm or less. Thus, it is possible to determine the relationship between vascular volume and vascular permeability within a single pixel and to study the dynamics of this relationship as well as other vascular properties with tumor growth and therapy. Using MRI to study transgenic tumors with specific genetic alterations, in combination with immunostaining of specific molecules not only on endothelial cells but targeted at various stages of the angiogenic pathway, will provide an even greater versatility for understanding tumor angiogenesis and vascularization especially when combined with three-dimensional interactive visualization software (78). With three-dimensional MRI maps, or multislice imaging, it should be possible to measure regions with the highest vascular volume and permeability, as well as the total tumor areas or volumes associated with these high vascular volume and permeability to understand the relationship between vascularization and metastasis. Clinically, some of the major foreseeable applications of contrast-enhanced MRI are to increase the specificity for detecting malignant lesions and for the prognosis of malignant lesions, to detect the efficiency of antiangiogenic treatments as they become clinically available, and equally importantly to use the uptake and distribution of contrast agents to predict the efficiency of delivery of therapeutic agents of similar size to the tumor (79).

**Acknowledgments:** Support from the USAMRMC (DAMD17-96-1-6131), from the Susan G. Komen Breast Cancer Foundation, and from the NIH (R01 CA73850) is gratefully acknowledged.

## REFERENCES

1. Goldmann, E. The growth of malignant disease in man and the lower animals, with special reference to the vascular system. *Proc R Soc Med* 1907;1:1–13.
2. Algire GH, Chalkley HW, Legallais FY, Park HD. Vascular reactions of normal and malignant tissues in vivo. I. Vascular reactions of mice to wounds and to normal and neoplastic transplants. *J Natl Cancer Inst* 1945;6:73–85.
3. Thomlinson RH, Gray LH. The histological structure of some human lung cancers and the possible implications for radiotherapy. *Br J Cancer* 1955;9:539–49.
4. Alper T, Howard-Flanders P. Role of oxygen in modifying the radiosensitivity of E. coli B. *Nature* 1956;178:978–9.
5. Jain RK. Transport of molecules across tumor vasculature. *Cancer Mestastasis Rev* 1987;6:559–93.
6. Jain RK. Transport of molecules in the tumor interstitium: A review. *Cancer Res* 1987;47:3039–51.
7. Jain RK. Determinants of tumor blood flow: A review: *Cancer Res* 1988;48:2641–58.
8. Rubin P, Casarett G. Microcirculation of tumors, part I: Anatomy, function, and necrosis. *Clin Radiol* 1966;17:220–9.
9. Wiig H, Tveit E, Hultborn R, Reed RK, Weiss L. Interstitial fluid pressure in DMBA-induced rat mammary tumours. *Scand J Clin Invest* 1982;42:59–4.
10. Tozer GM, Lewis S, Michalowski A, Aber V. The relationship between regional variations in blood flow and histology in a transplanted rat fibrosarcoma. *Br J Cancer* 1990;61:250–7.
11. Falk P. Differences in vascular pattern between spontaneous and the transplanted C3H mouse mammary carcinoma. *Eur J Cancer* 1982; 18:155–65.
12. Weidner N, Semple JP, Welch WR, Folkman J. Tumor angiogenesis and metastasis—Correlation in invasive brest carcinoma. *N Engl J Med* 1991;324:1–8.
13. Horak ER, Leek R, Klenk N, et al. Angiogenesis, assessed by platelet/endothelial cell adhesion molecule antibodies, as indicator of node metastases and survival in breast cancer. *Lancet* 1992;340: 1120–4.
14. Hall MC, Zagars GK, Troncoso P, et al. Significance of tumor angiogenesis in clinically localized prostate carcinoma treated with external beam radiotherapy. *Urology* 1994;44:869–75.
15. Siegal JA, Uu E, Brawer MK. Topography of neovascularity in human prostate carcinoma. *Cancer* 1995;75:2545–51.
16. Takahashi Y, Kitadai Y, Bucana CD, Cleary KR, Ellis LM. Expression of vascular endothelial growth factor and its receptor, KDR, correlates with vascularity, metastasis, and proliferation of human colon cancer. *Cancer Res* 1995;55:3964–8.
17. Folkman J. Anti-angiogenesis: New concept for therapy of solid tumors. *Ann Surg* 1972;175:409–16.
18. Denekamp J. Review article: Angiogenesis, neovascular proliferation and vascular pathophysiology as targets for cancer therapy. *Br J Radiol* 1993;66:181–96.
19. Boehm T, Folkman J, Browder T, O'Reilly MS. Antiangiogenic therapy of experimental cancer does not induce drug resistance. *Nature* 1997;390:404–7.
20. Greenblatt M, Shubik P. Tumor angiogenesis: Transfilter diffusion studies in the hamster by the transparent chamber technique. *J Natl Cancer Inst* 1968;41:111–24.
21. Folkman J, Merler E, Abernathy C, Williams G. Isolation of a tumor factor responsible for angiogenesis. *J Exp Med* 1971;133:275–88.
22. Folkman J. How is blood vessel growth regulated in normal and neoplastic tissue? *Cancer Res* 1986;46:467–73.
23. Folkman J, Watson K, Ingber D, Hanahan D. Induction of angio-

genesis during the transition from hyperplasia to neoplasia. *Nature* 1989;339:58–61.
24. Tannock IF. Population kinetics of carcinoma cells, capillary endothelial cells, and fibroblasts in a transplanted mouse mammary tumor. *Cancer Res* 1970;30:2470–6.
25. Hirst DG, Denekamp J, Hobson B. Proliferation kinetics of endothelial and tumour cells in three mouse mammary carcinomas. *Cell Tissue Kinetics* 1982;15:251–61.
26. Moses MA. The role of vascularization in tumor metastasis. In: F. William Orr, MR Buchanan, L Weiss, eds. *Microcirculation in cancer metastasis.* Boca Raton: CRC Press, 1991:257–76.
27. Vaupel P, Kallinowski F, Okunieff P. Blood flow, oxygen and nutrient supply, and metabolic microenvironment of human tumors: A review. *Cancer Res* 1989;49:6449–65.
28. Neufeld G, Cohen T, Gengrinovitch S, Poltorak Z. Vascular endothelial growth factor (VEGF) and its receptors. *FASEB J* 1999;13: 9–22.
29. Gospodarowicz D, Abraham JA, Schilling J. Isolation and characterization of a vascular endothelial cell mitogen produced by pituitary-derived folliculo stellate cells. *Proc Natl Acad Sci USA* 1989; 86:7311–5.
30. Ferrara N, Henzel WJ. Pituitary follicular cells secrete a novel heparin-ninding growth factor specific for vascular endothelial cells. *Biochem Biophys Res Commun* 1989;161:851–8.
31. Senger DR, Galli SJ, Dvorak AM, Perruzzi CA, Harvey VS, Dvorak HF. Tumor cells secrete a vascular permeability factor that promotes accumulation of ascites fluid. *Science* 1983;219:983–5.
32. Bacic M, Edwards NA, Merril MJ. Differential expression of vascular endothelial growth factor (vascular permeability factor) forms in rat tissues—Short communication. *Growth Factors* 1995;12: 11–5.
33. Levy AP, Levy NS, Wegner S, Goldberg MA. Transcriptional regulation of the rat endothelial growth factor gene by hypoxia. *J Biol Chem* 1995;270:13333–40.
34. Claffey KP, Shih SC, Mullen A, et al. Identification of a human VPF/VEGF 3′ untranslated region mediating hypoxia-induced mRNA stability. *Mol Biol Cell* 1998;9:469–81.
35. Chiarugi V, Magnelli L, Gallo O. Cox-2, iNOS and p53 as playmakers of tumor angiogenesis (Review). *Int J Mol Med* 1998;2: 715–9.
36. Brooks SE, Gu X, Kaufmann PM, Marcus DM, Caldwell RB. Modulation of VEGF production by pH and glucose in retinal Muller cells. *Curr Eye Res* 1998;17:875–82.
37. Shweiki D, Neeman M, Itin A, Keshet E. Induction of vascular endothelial growth factor expression by hypoxia and by glucose deficiency in multicell spheroids: Implication for tumor angiogenesis. *Proc Natl Acad Sci USA* 1995;92:768–72.
38. Feldkamp MM, Lau N, Rak J, Kerbel RS, Guha A. Normoxic and hypoxic regulation of vascular endothelial growth factor (VEGF) by astrocytoma cells is mediated by Ras. *Int J Cancer* 1999;81:118–24.
39. Mukhopadhyay D, Tsiokas I, Sukhatme VP. Wild-type p53 and v-src exert opposing influences on human vascular endothelial growth factor gene expression. *Cancer Res* 1995;55:6161–5.
40. Bouvet M, Ellis LM, Nishizaki M, et al. Adenovirus-mediated wild type p53 gene transfer down-regulates vascular endothelial growth factor expression and inhibits angiogenesis in human colon cancer. *Cancer Res* 1998;58:2288–92.
41. Agani F, Kirsch DG, Friedman SL, Kastan MB, Semenza GL. p53 does not repress hypoxia-induced transcription of the vascular endothelial growth factor gene. *Cancer Res* 1997;57:4474–7.
42. Ausprunk DH, Knighton DR, Folkman J. Vascularization of normal and neoplastic tissues grafted to the chick chorioallantois: Role of host and preexisting graft blood vessels. *Am J Pathol* 1975;79:597–628.
43. Gimbrone MA, Cotran RS, Leapman SB, Folkman J. Tumor growth and neovascularization: An experimental model using the rabbit cornea. *J Natl Cancer Inst* 1974;52:413–27.
44. Jain RK, Ward-Hartley KA. Tumor blood flow: Characterization, modification and role in hyperthermia. *IEEE Trans* 1984;SU-31: 504–26.
45. Chalkley HW. Method for the quantitative morphologic analysis of tissues. *JNCI* 1943;4:47–53.
46. Kacemi A, Vervelle C, Uzan S, Challier JC. Immunostaining of vascular, perivascular cells and stromal components in human placental villi. *Cell Mol Biol* 1999;45:101–13.
47. Song CW, Levitt SH. Quantitative study of vascularity in Walker carcinoma 256. *Cancer Res* 1971;31:587–89.
48. Peterson H-I. Vascular and extravascular spaces in tumors: Tumor vascular permeability. In: Peterson H-I, ed. *Tumor blood circulation: Angiogenesis, vascular morphology and blood flow of experimental and human tumors.* Boca Raton: CRC Press, 1979:77–85.
49. Abramovitch R, Frenkiel D, Neeman M. Analysis of subcutaneous angiogenesis by gradient echo magnetic resonance imaging. *Magn Reson Med* 1998;39:813–24.
50. Ostergaard L, Weisskoff RM, Chesler D, Gyldensted C, Rosen BR. High resolution measurement of cerebral blood flow using intravascular tracer bolus passages. Part I: Mathematical approach and statistical snalysis. *Magn Reson Med* 1996;36:715–25.
51. Sorensen AG, Tievsky AL, Ostergaard L, Weisskoff RM, Rosen BR. Contrast agents in functional MR imaging. *J Magn Reson Imaging* 1997;7:47–5.
52. Schmiedl U, Ogan M, Paajanen H, et al. Albumin labeled with Gd-DTPA as an intravascular, blood pool-enhancing agent for MR imaging: biodistribution and imaging studies. *Radiology* 1987;162: 205–10.
53. Schwarzbauer C, Syha J, Haase A. Quantification of regional blood volume by rapid T1 mapping. *Magn Reson Med* 1993;29:709–12.
54. Sipkins DA, Cheresh DA, Kazemi MR, Nevin LM, Bendarski MD, Li KCP. Detection of tumor angiogenesis in vivo by $\alpha v\beta 3$-targeted magnetic resonance imaging. *Nature Med* 1998;4:623–6.
55. Larcombe McDouall JB, Evelhoch JL. Deuterium nuclear magnetic resonance imaging of tracer distribution in $D_2O$ clearance measurements of tumor blood flow in mice. *Cancer Res* 1990;50:363–9.
56. Evelhoch JL. Measurement of tumor blood flow by deuterium NMR and the effects of modifiers. *NMR Biomed* 1992;5:290–5.
57. Ogawa S, Lee T-M, Nayak AS, Glynn P. Oxygenation-sensitive contrast in magnetic resonance image of rodent brain at high magnetic fields. *Magn Reson Med* 1990;14:68–78.
58. Carmeliet P, Dor Y, Herbert J-M, et al. Role of HIF-1a in hypoxia-mediated apoptosis, cell proliferation and tumor angiogenesis. *Nature* 1998;394:485–90.
59. Sinha S, Lucas-Quesada FA, DeBruhl ND, et al. Multifeature analysis of Gd-enhanced MR images of breast lesions. *J Magn Reson Imaging* 1997;7:1016–26.
60. Furman-Haran E, Margalit R, Grobgeld D, Degani H. Dynamic contrast-enhanced magnetic resonance imaging reveals stress-induced angiogenesis in MCF7 human breast tumors. *Proc Natl Acad Sci USA* 1996;93:6247–51.
61. Degani H, Gusis V, Weinstein D, Fields S, Strano S. Mapping pathophysiological features of breast tumors by MRI at high spatial resolution. *Nature Med* 1997;3:780–2.
62. Hawighorst H, Knapstein PG, Weikel W, et al. Angiogenesis of uterine cervical carcinoma: characterization by pharmacokinetic magnetic resonance parameters and histological microvessel density with correlation to lymphatic involvement. *Cancer Res* 1997;57: 4777–86.
63. Tofts PS. Modeling tracer kinetics in dynamic Gd-DTPA MR imaging. *J Magn Reson Imaging* 1997;7:91–101.
64. Ohno K, Pettigrew KD, Rapoport SI. Local cerebral blood flow in the conscious rat as measured with 14C-antipyrene, 14C-iodoantipyrine and 3H-nicotine. *Stroke* 1979;10:62–7.
65. Larsson HBW, Stubgaard M, Frederiksen JL, Jensen M, Henriksen O, Paulson OB. Quantitation of blood-brain barrier defect by magnetic resonance imaging and gadolinium-DTPA in patients with multiple sclerosis and brain tumors. *Magn Reson Med* 1990;16:117–31.
66. Kovar DA, Lewis MZ, River JN, Lipton MJ, Karczmar GS. In vivo

imaging of extraction fraction of low molecular weight MR contrast agents and perfusion rate in rodent tumors. *Magn Reson Med* 1997; 38:259–68.

67. Ogan MD, Schmiedl U, Mosley ME, Grodd W, Paajanen H, Brasch RC. Albumin labeled with Gd-DTPA; an intravascular contrast enhancing agent for magnetic resonance blood pool imaging: preparation and characterization. *Invest Radiol* 1987;22:665–71.
68. Brasch R, Pham C, Shames D, et al. Assessing tumor angiogenesis using macromolecular MR imaging contrast media. *J Magn Reson Imaging* 1997;7:68–74.
69. Braunschweiger P, Schiffer LM. Effect of dexamethasone on vascular function in RIF-1 tumors. *Cancer Res* 1986;46:3299–303.
70. Braunschweiger P. Effect of cyclophosphamide on the pathophysiology of RIF-1 solid tumors. *Cancer Res* 1988;48:4206–10.
71. Tozer GM, Morris CC. Blood flow and blood volume in a transplanted rat fibrosarcoma: Comparison with various normal tissues. *Radiother Oncol* 1990;17:153–66.
72. Su M-Y, Muhler A, Lao X, Nalcioglu O. Tumor characterization with dynamic contrast-enhanced MRI using contrast agents of various molecular weights. *Magn Reson Med* 1998;39:259–69.
73. Su M-Y, Wang Z, Roth GM, Lao X, Samoszuk MK, Nalcioglu O. Pharmacokinetic changes induced by vasomodulators in kidneys, livers, muscles, and implanted tumors in rats as measured by dynamic Gd-DTPA-enhanced MRI. *Magn Reson Med* 1996;36:868–77.
74. Schwickert HC, Roberts TPL, Shames DM, et al. Quantification of liver blood volume: Comparison of ultra short T1 inversion recovery echo planar imaging (ULSTIR-EPI), with dynamic 3D-gradient recalled echo imaging. *Magn Reson Med* 1995;34:845–52.
75. Donahue KM, Weisskoff RM, Chesler DA, et al. Improving MR quantitation of regional blood volume with intravascular T1 contrast agents: Accuracy, precision, and water exchange. *Magn Reson Med* 1996;36:858–67.
76. Yuan F, Salehi AA, Boucher Y, Vasthare US, Tuma RF, Jain RK. Vascular permeability and microcirculation of gliomas and mammary carcinomas transplanted in rat and mouse cranial windows. *Cancer Res* 1994;54:4564–8.
77. Steel GG. *Growth kinetics of tumours: Cell population kinetics in relation to the growth and treatment of cancer.* Oxford: Clarendon Press, 1977.
78. Bhujwalla ZM, Artemov D, Solaiyappan M, Mao D, Backer JP. Comparison of vascular volume and permeability for tumor derived from metastatic human breast cancer cells with and without the metastasis suppressor gene nm23. In: *Proceedings of 7th Scientific Meeting of the ISMRM,* Philadelphia, 1999.
79. Artemov D, Bhujwalla ZM. Drug delivery to tumors: Potential of MR for measurement and prediction. In *Proceedings of 7th Scientific Meeting of the ISMRM,* Philadelphia, 1999.

Magnetic Resonance in Medicine 41:897–903 (1999)

# Nm23-Transfected MDA-MB-435 Human Breast Carcinoma Cells Form Tumors With Altered Phospholipid Metabolism and pH: A $^{31}$P Nuclear Magnetic Resonance Study In Vivo and In Vitro

Zaver M. Bhujwalla,[1]* Eric O. Aboagye,[1] Robert J. Gillies,[2] V.P. Chacko,[1] Charmaine E. Mendola,[3] and Joseph M. Backer[3]

**Nm23 genes are involved in the control of the metastatic potential of breast carcinoma cells. To understand the impact of nm23 genes on tumor physiology and metabolism, a $^{31}$P nuclear magnetic resonance (NMR) spectroscopic study was performed on tumors formed in the mammary fat pad of severe combined immunodeficiency mice by MDA-MB-435 human breast carcinoma cells transfected with cDNA encoding wild type nm23-H1 and nm23-H2 proteins. Tumors formed by MDA-MB-435 cells transfected with vector alone were used as controls. All transgene tumors exhibited significantly higher levels of phosphodiester (PDE) compounds relative to phosphomonoester (PME) compounds in vivo compared with control tumors. Similar differences in PDE and PME also were observed for spectra obtained from cells growing in culture. Intracellular pH was significantly lower and extracellular pH was significantly higher for transgene tumors compared with control tumors. Histologic analysis of lung sections confirmed reductions in incidence, number, and size of metastatic nodules for animals bearing transgene tumors. These results suggest that nm23 genes may affect suppression of metastasis through phospholipid-mediated signaling and cellular pH regulation. Magn Reson Med 41:897–903, 1999.** © **1999 Wiley-Liss, Inc.**

**Key words: human breast carcinoma metastasis; nonmetastatic 23 transfection; phospholipid metabolism and pH; $^{31}$P nuclear magnetic resonance spectroscopy**

The ability of solid tumors to metastasize and establish colonies at distant sites is one of the most life-threatening aspects of cancer. Despite continuing advances in the molecular characterization of events promoting metastasis, little impact has been made on therapy or survival for patients with advanced metastatic tumors (1). This is due partly to the lack of identifiable targets against which to design antineoplastic agents to control the metastatic spread of cancer. Multinuclear magnetic resonance (multi-NMR) methods have a unique role to play in answering this challenge by providing an understanding of the biochemical and physiologic mechanisms involved in invasion and metastasis. Such an understanding can identify rational targets for therapy.

Recently it was shown that the nm23 (nonmetastatic) gene is related to suppression of metastasis; the metastasis suppression function of the nm23 gene was proposed on the basis of correlation and transfection studies in murine and human systems (2,3). Two highly homologous and evolutionary conserved nm23 genes, nm23–1 and nm23–2, have been identified in rodents (4,5), and two nm23 genes (nm23-H1 and nm23-H2) have been identified in humans (6,7). The two murine nm23 genomic DNAs have been cloned and sequenced (8,9). The human nm23-H1 and nm23-H2 genes have been localized to chromosome 17q21 (10,11). These genes encode 17-kDa proteins identified as nucleoside diphosphate kinase A (NDPK A) and NDPK B, which form homomers and heteromers. In addition, NDPK B displays an increasing list of other activities that apparently are unrelated to its catalytic functions (4). However, the cellular mechanisms by which the nm23 protein suppresses metastatic phenotypic expression is still unknown. In the current study, we have used $^{31}$P NMR spectroscopy to study metabolic and physiologic characteristics of tumors induced in severe combined immunodeficiency (SCID) mice by MDA-MB-435 human breast carcinoma cells transfected with wild type cDNA of nm23-H1 and nm23-H2 and demonstrated that nm23 transfection alters phospholipid metabolism and pH in these breast tumors. Histologic analysis of lung sections from tumor-bearing animals was performed to confirm decreases in metastatic behavior of these breast tumors following transfection with nm23-H1 and nm23-H2. These studies have provided further understanding of the cellular functions of nm23 and of the mechanisms of action of nm23–1 and nm23–2 genes and their role in metastatic dissemination of tumor cells.

## MATERIALS AND METHODS

Coding sequences of normal nm23-H1 and nm23-H2 proteins were cloned into the eucaryotic expression vector pβalPstNeo under control of a constitutive HCMV promoter (11,12). The vector contains an neo resistance gene under control of a simian virus 24 (SV40) promoter. MDA-MB-435 breast carcinoma cells were transfected with nm23 constructs by using a Lipofectin kit (BRL-Life Technologies, Inc., Gaithersburg, MD), and selection of trans-

[1]Oncology Section-Division of Magnetic Resonance Research, Department of Radiology, The Johns Hopkins University School of Medicine, Baltimore, Maryland.

[2]Department of Biochemistry, University of Arizona, Tucson, Arizona.

[3]Department of Microbiology and Immunology, New York Medical College, Valhalla, New York.

Grant sponsor: USAMRMC; Grant numbers: DAMD17–96–1-6131, DAMD17–94–4368, CA58881–03, and DAMD17–96–6078.

Charmaine E. Mendola is currently at the Department of Pharmacology, UMDNJ-R.W. Johnson Medical School, Piscataway, NJ 08854.

*Correspondence to: Zaver M. Bhujwalla, Department of Radiology, The Johns Hopkins University School of Medicine, Room 208C Traylor Building, 720 Rutland Avenue, Baltimore, MD 21205. E-mail: zaver@mri.jhu.edu

Received 28 September 1998; revised 16 December 1998; accepted 26 December 1998.

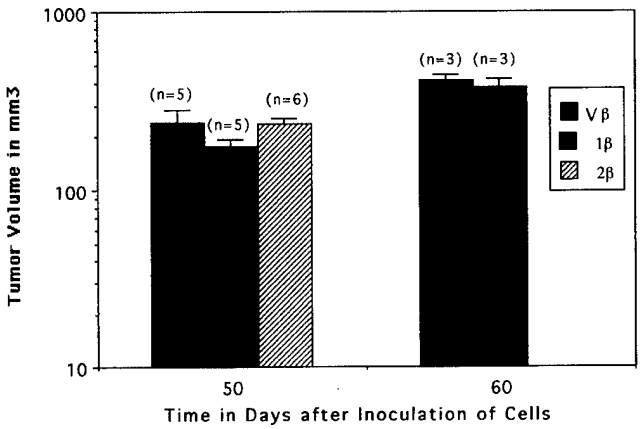


FIG. 1. Tumor volumes following inoculation of identical cell numbers ($10^6$ cells in 0.05 ml of Hank's balanced salt solution) in the mammary fat pad for the groups of animals used in the study. Bars represent ± 1 standard error of the mean (S.E.M.).

fected clones was performed in the presence 800 μg/ml G418. Nm23-transfected pooled clones of MDA-MB-435 were then transfected with p1Zsp-βgluc (puro), a mammalian expression vector containing bacterial β-glucuronidase under control of a constitutive HCMV promoter and puromycin-resistance gene under control of an SV40 promoter (gift from Dr. T. Jones, Lederle Laboratories). Selection of clones expressing bacterial β-glucuronidase was performed in the presence of 0.375 μg/ml puromycin and 800 μg/ml G418. Pooled clones of double-transfected cells named MDA-MB-435-Vβ, MDA-MB-453–1β, and MDA-MB-435–2β (for vector/β-glucuronidase, nm23-H1/β-glucuronidase, and nm23-H2/β-glucuronidase transfections, respectively) were maintained in the presence of 0.375 μg/ml puromycin and 200 μg/ml G418 in Dulbecco's minimum essential medium (Sigma Ltd., St. Louis, MO) containing 10% fetal bovine serum (Sigma Ltd.). Presence of transgenes was confirmed by polymerase chain reaction (PCR) analysis, Western blot analysis, and staining with 5-bromo-4-chloro-3-indol 1 glucuronide (X-glu). Cell doubling times were determined by counting cells plated in 10 mm Petri dishes (three plates per cell line) using a hemocytomter. Cells were counted 48 hr after plating $5 \times 10^4$ cells per Petri dish. Cell doubling times were approximately 1.5–2.5 days, with no significant differences between the cell lines. Mean values ± 1 standard error of the mean (S.E.M.) for the three lines were as follows: 2.3 days ± 0.4 (MDA-MB-435-Vβ), 1.5 days ± 0.1 (MDA-MB-435–1β), and 2.4 days ± 0.6 (MDA-MB-435–2β).

MDA-MB-435-Vβ, MDA-MB-435–1β, and MDA-MB-435–2β cells were inoculated in the upper left thoracic mammary fat pad of SCID mice, and $10^6$ cells were inoculated in 0.05 ml of Hank's balanced salt solution (Sigma Ltd.). The experimental protocol was approved by the Institutional Animal Care and Use Committee. Mice were anesthetized with ketamine (50 mg/kg; Aveco Ltd.) and acepromazine (5 mg/kg; Aveco Ltd.). Tumor volumes, which were measured just prior to performing the $^{31}$P NMR spectroscopic studies, were calculated from caliper measurements of tumor axes (a,b,c) by using the equation for an elliptical volume (π/6)abc. Volumes used in this study were of the order of 300 mm$^3$.

$^{31}$P NMR spectroscopic studies were performed on a GE CSI 4.7 T instrument (General Electric, Fremont, CA) equipped with shielded gradients. Spectra were obtained with home-built solenoidal coils fitted around the tumor. Because the coil design allowed the probe to be tuned to the proton frequency for shimming, proton images were acquired with the coil to ascertain that only the tumor (and skin) was in the sensitive volume of the coil. Animal body temperature was maintained at 37°C by heat generated

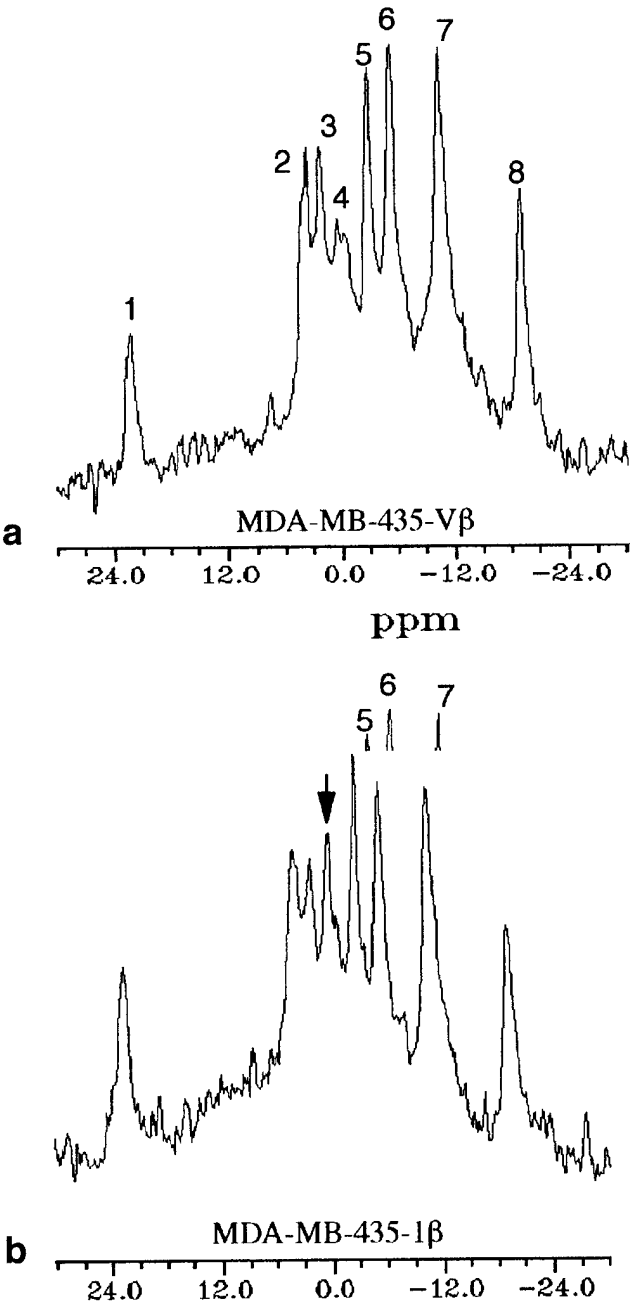


FIG. 2. Representative fully relaxed $^{31}$P nuclear magnetic resonance (NMR) spectra obtained from an MDA-MB-435-Vβ tumor (**a**) and from an MDA-MB-435–1β tumor (**b**). Peak assignments are 1) 3-aminopropylphosphonate (3-APP); 2) phosphomonoester (PME); 3) inorganic phosphate (Pi); 4) phosphodiester (PDE); 5) phosphocreatine (PCr); 6) γ-nucleoside triphosphate (NTP); 7) α-NTP (set to −10 ppm); and 8) β-NTP.

from a pad circulating with warm water. For the $^{31}P$ NMR studies, mice were injected intraperitoneally with a solution of the extracellular pH marker 3-aminopropylphosphonate (3-APP; Sigma Ltd.) administered in a volume of 0.2 ml saline (480 mg/kg) following anesthetization. Fully relaxed $^{31}P$ NMR spectra were obtained by using a 45° flip angle with 64 scans, a repetition of 5 sec, and a sweep width (SW) of 10000 Hz. Parameters were determined from two spectra obtained per tumor. NMR examinations were completed within 20 min. Extracellular pH (pHe) was obtained from the chemical shift of 3-APP (13), and intracellular pH (pHi) was obtained from the chemical shift of inorganic phosphate (Pi) (14) from the endogenous reference α-nucleoside triphosphate (NTP) set to −7.57 ppm. pHe was calculated from the relationship $pH = 6.91 + \log [(\delta_{3\text{-APP}} - 21.11)/(24.30 - \delta_{3\text{-APP}})]$, and pHi was calculated from the relationship $pH = 6.66 + \log [(\delta_{Pi} - 0.65)/(3.11 - \delta_{Pi})]$. Data sets were processed by using an exponential line-broadening factor of 22 Hz. Peak areas were determined in the time domain by using an in-house, nonlinear, least-squares, curve-fitting routine for MR data analysis written by Dr. D.C. Shungu.

High-resolution spectra of perchloric acid (PCA) extracts from tumors and cell lines were obtained to resolve the components of the peak in the phosphodiester (PDE) and the phosphomonoester (PME) regions. Mice were anesthetized, and tumors were excised and immediately freeze clamped. Neutralized PCA extracts of tumors were lyophilized and resuspended in $D_2O$. High-resolution $^{31}P$ NMR spectra of tumor extracts were acquired at 11.7 T (MSL-500 spectrometer; Bruker) with a 10-mm high-resolution probe. Spectra were acquired with a 45° flip angle, an SW of 8000 Hz, a repetition time of 5 sec, a block size of 4 K, and 3600 scans.

PCA extracts were obtained from equal numbers of cells for all of the lines used in the study. Cell volumes of the lines were identical. Cells from approximately eight flasks with similar confluency for each cell line were trypsinized, and the action of trypsin was blocked with ice-cold growth medium. Cells were fed approximately 3 hr prior to trypsinization. Cells were washed twice with cold 0.9% NaCl solution and extracted with ice-cold 8% (volume/volume) PCA. The supernatant was neutralized (with 3 M $K_2CO_3$/1 M KOH), lyophilized, and resuspended in $D_2O$. Phosphorus spectra of the extracts were obtained at 11.7 T with a 10-mm high-resolution probe. Spectral acquisition parameters were 45° flip angle, SW = 8000 Hz, 5 sec repetition time, 4 K block size, and scans = 32000–128000.

Lungs from tumor-bearing animals were excised at the end of the NMR experiments and fixed in 10% buffered formalin. Three 5-μm-thick, paraffin-embedded sections were obtained from each pair of lungs and stained with hematoxylin and eosin. Lung sections were examined under an optical microscope and evaluated for incidence, number, and size of metastatic nodules.

Statistical analysis of the data was performed by using StatView II software (version 1.04; Abacus Concepts, Inc., Berkeley, CA). One factorial analysis of variance (ANOVA) was used to evaluate the statistical significance of the in vivo data.

## RESULTS

All of the cell lines were tumorigenic in SCID mice, with a latent period of 5–6 weeks. Growth rates for control and transgene tumors were similar, with a volume-doubling time of 10–14 days. Tumor volumes for groups of animals inoculated at the same time are shown in Figure 1. These data demonstrate the absence of any significant differences in growth rate or "silent interval" following inoculation of the different cell lines in the mammary fat pad.

The most striking difference between $^{31}P$ NMR spectra of control (Fig. 2a) and transgene tumors (Fig. 2b) was a marked increase of the peak in the PDE region relative to the PME region in spectra of transgene tumors. The components of the PME region were identified as the membrane precursors phosphocholine (PC) and phosphoethanolamine (PE), and those of the PDE region were identified as the membrane breakdown products glycerophosphocholine (GPC) and glycerophosphoethanolamine (GPE). These components were identified from the high-resolution $^{31}P$ NMR spectra of tumor extracts by using the spectral assignments of Evanochko et al. (15). Elevation of the PDE peak relative to the PME peak was observed consistently for all transgene tumors but not for MDA-MB-435-Vβ control tumors. An example of a high-resolution spectrum obtained from PCA extracts of MDA-MB-435–1β tumors

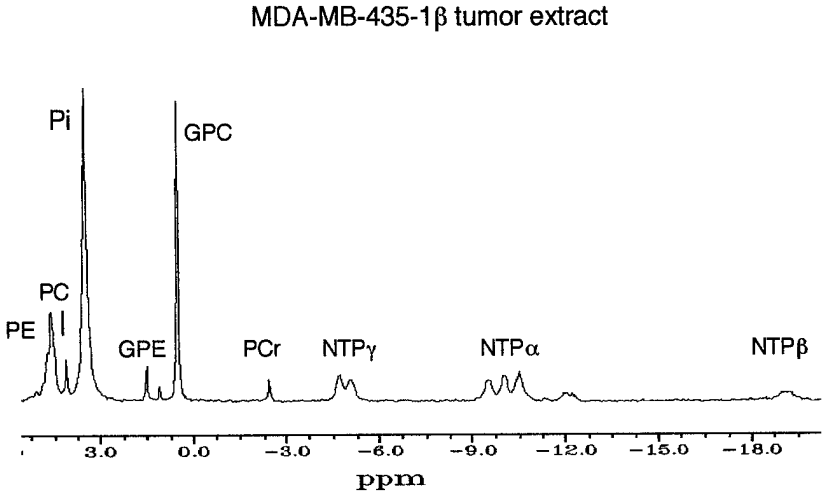


FIG. 3. High-resolution $^{31}P$ NMR spectrum from MDA-MB-435–1β tumor extract (obtained from three pooled tumors). Spectral acquisition parameters for in vivo tumors and extract are detailed in Materials and Methods. GPC, glycerophosphocholine; GPE, glycerophosphoethanolamine; PC, phosphocholine; PE, phosphoethanolamine.

Table 1
Nuclear Magnetic Resonance Parameters and Tumor Volumes Obtained From In Vivo Tumors Derived From Control and Transgene MDA-MD-435 Cells

| Solid tumor type | Transfection and nm23 levels | Tumor volume ($mm^3$) | PDE/PME = [GPE + GPC] / [PE + PC] | pHi | pHe |
|---|---|---|---|---|---|
| Control MDA-MB-435-Vβ (n = 7) | Vector/β-glucuronidase transfection (low nm23-H1, H2) | 324 ± 42 | 0.60 ± 0.05 | 7.37 ± 0.07 | 6.8 ± 0.11 |
| Transgene MDA-MB-435-1β (n = 6) | nm23-H1/β-glucuronidase transfection (high nm23-H1) | 311 ± 45 | 1.45 ± 0.24* | 7.16 ± 0.05* | 7.17 ± 0.1* |
| Transgene MDA-MB-435-2β (n = 6) | nm23-H2/β-glucuronidase transfection (high nm23-H2) | 255 ± 19 | 1.36 ± 0.14* | 7.15 ± 0.06* | 7.09 ± 0.08* |

*Ninety-five percent confidence limit ($P < 0.05$), analysis of variance, Fisher's protected least significant difference test. Values represent mean ± 1 standard error of the mean; n represents number of animals for each group; PDE, phosphodiester; PME, phosphomonoester; GPE, glycerophosphoethanolamine; GPC, glycerophosphocholine; PE, phosphoethanolamine; PC, phosphocholine; pHi, intracellular pH; pHe, extracellular pH.

with the corresponding peak assignments is shown in Figure 3.

The in vivo results for all of the animals in the study are summarized in Table 1 and show that the PDE/PME ratio was significantly higher for the transgene tumors compared with control tumors. Significant differences in pHi and pHe also were detected for the transgene tumors. pHi was significantly lower, whereas pHe was significantly higher for nm23-H1- and nm23-H2-transfected tumors compared with those derived from cells transfected with vector only (Table 1). No significant differences in NTP/Pi were detected between the cell lines.

$^{31}P$ NMR high-resolution spectra of isolated cell extracts obtained from cells growing in tissue culture flasks for each of the transfected cell lines and the control cell line are shown in Figure 4. PDE/PME ratios obtained from cell extracts are summarized in Table 2. Observations made in vivo also were apparent in the spectra of cell extracts, suggesting that differences in PME and PDE peaks for the transgene tumors are due to intrinsic cellular properties arising from transfection of cells with nm23 rather than in vivo physiologic effects related to tumor vascularization or the fraction of necrosis.

For the evaluation of metastasis, we analyzed the lungs of five animals bearing MDA-MB-435-Vβ tumors and six animals with MDA-MB-435–1β tumors. Because the two nm23 genes (nm23-H1 and nm23-H2) are 88% to 90% identical in their amino acid sequences, respectively, we analyzed the lungs of two randomly picked animals with MDA-MB-435–2β tumors that showed no evidence of lung metastasis. Data from micrcoscopic analysis of the lung specimens obtained from tumor bearing mice are presented in Table 3. Lungs obtained from animals bearing transgene tumors showed a reduction in the incidence as well as the number and size of metastatic nodules compared with control tumors (Fig. 5).

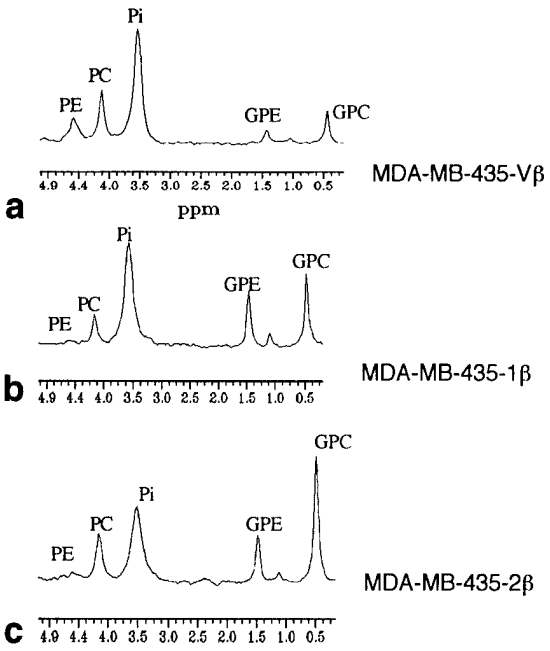


FIG. 4. High-resolution $^{31}P$ NMR spectra of cells from MDA-MB-435-Vβ (**a**), MDA-MB-435–1β (**b**), and MDA-MB-435–2β (**c**) cell lines maintained in tissue culture flasks. Spectra are expanded to focus on the phospholipid region. Spectral acquisition parameters are detailed in Materials and Methods.

## DISCUSSION

The metastatic cascade is a complex phenomenon. To establish metastatic colonies at a site distant from the primary tumor, a cancer cell should pass successfully through the following stages: invasion, intravasation, arrest of cancer cells, extravasation, and, finally, neovascular-

Table 2
Phosphodiester/Phosphomonoester Ratios of Control and Transgene Cells

| Tumor cell type | Transfection and nm23 levels | (PDE/PME) = [GPE + GPC][a] / [PE + PC] |
|---|---|---|
| Control MDA-MB-435-Vβ | Vector/β-glucuronidase transfection (low nm23-H1, 2) | 0.53 |
| Transgene MDA-MB-435-1β | nm23-H1/β-glucuronidase transfection (high nm23-H1) | 1.96 |
| Transgene MDA-MB-435-2β | nm23-H2/β-glucuronidase transfection (high nm23-H2) | 1.7 |

[a]Values obtained from eight flasks per cell line. Cells were obtained from a total of eight T-150 flasks for each cell line.

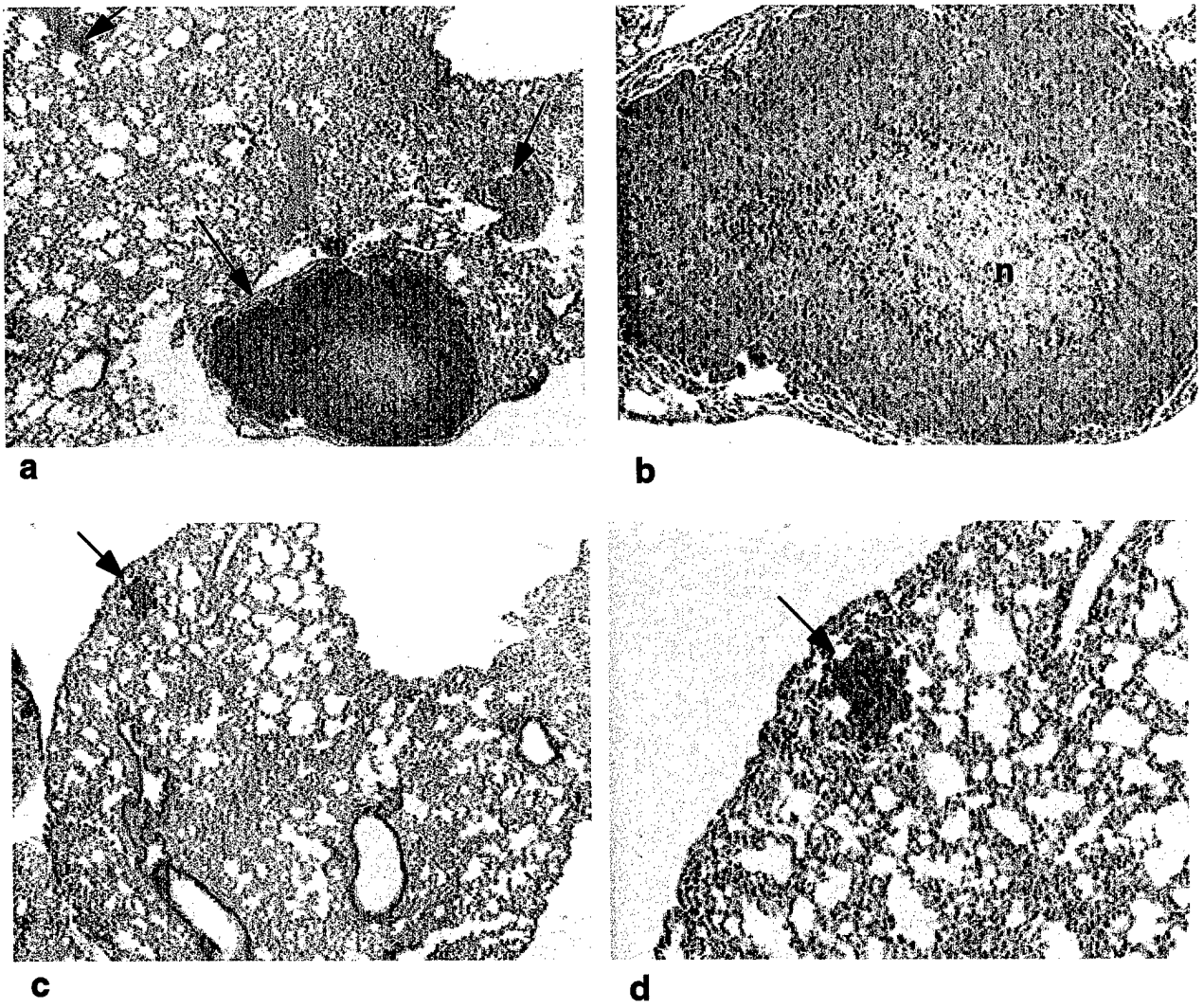


FIG. 5. Photomicrographs demonstrating the marked differences in metastatic nodules in lung sections obtained from mice bearing MDA-MB-435-Vβ and MDA-MB-435–1β tumors. **a,b:** Low- and high-power photomicrographs, respectively, from lung sections obtained from a mouse with an MDA-MB-435-Vβ tumor. **c,d:** Low- and high-power photomicrographs, respectively, from lung sections obtained from a mouse with an MDA-MB-435–1β tumor. Metastatic nodules are marked by arrows, and n denotes a region of necrosis in the metastatic nodule shown in b. No nodules were observed in lung sections that were examined for mice bearing MDA-MB-435–2β tumors.

ization. Attenuation of metastasis may occur at any of these stages. Histologic analyses of lung sections from tumor-bearing animals demonstrated that control tumors and transgene tumors formed by derivatives of MDA-MB-435 human breast carcinoma cells transfected with nm23 constructs showed different metastatic potential. $^{31}$P NMR spectra of primary tumors in SCID mice revealed significant differences in the phospholipid composition, pHi, and pHe of control and transgene tumors. Because transgene tumors were formed by pooled, transfected cells, these alterations were not due to properties of individual clones. These differences in $^{31}$P NMR spectra have provided an insight into how the loss of the nm23 gene induces metabolic and physiologic alterations that may facilitate metastatic dissemination.

Transgene tumors in vivo formed by wild type forms of nm23-H1 and nm23-H2 exhibited a significantly higher amount of PDE relative to PME levels compared with control tumors. These differences in phospholipid metabo-

Table 3
Incidence, Number, and Size of Metastatic Nodules Detected in Histologic Sections Obtained from Lungs of Tumor-Bearing Animals

| Tumor type | Incidence of metastatic nodules[a] | Number of metastatic nodules averaged for all animals | Range of sizes of metastatic nodules |
|---|---|---|---|
| Control MDA-MB-435-Vβ | 5/5 | 20 | 50–3000 μm[b] |
| Transgene MDA-MB-435-1β | 4/6 | 2 | 50–700 μm[c] |
| Transgene MDA-MB-435-2β | 0/2 | 0 | — |

[a]Number of animals with lungs containing metastatic nodules/number of animals with lungs examined (three histologic sections were analyzed for each lung specimen).
[b]Mean nodule diameter averaged over all the sections was 800 μm.
[c]Only one nodule was 700 μm in diameter. The remaining nodules were less than 100 μm in diameter.

lism also were detected in cultured cell extracts. The higher PDE levels, including an elevation of GPC, detected for the transgene tumors therefore appeared to be due to cellular characteristics rather than to in vivo physiologic characteristics, such as vascularization or necrosis. GPC is formed by degradation of membrane phospholipids by the enzyme phospholipase $A_2$ ($PLA_2$), and this mechanism of $PLA_2$ on membrane phospholipids provides precursors for eicosanoids when the cleaved fatty acid is arachidonic acid (16). Arachidonic acid-derived eicosanoids include important lipid mediators in signal transduction and tumor promotion, such as prostaglandins, thromboxanes, and leukotrienes (17). These oxygenated fatty acids can have diverse effects on cancer cell motility, invasion, and metastasis (17–20), and the changes in phospholipid metabolism detected following nm23 transfection may reflect the involvement of the nm23 gene product in phospholipid-mediated signaling mechanisms regulating cell motility. This possibility is consistent with the observation by Kantor et al. (21) that murine melanoma and human breast carcinoma cells that are transfected stably with nm23-H1 do not migrate in response to chemoattractants.

The second significant metabolic effect was the difference in both pHi and pHe between the control and transgene tumors. Transgene tumors formed by MDA-MB-435–1β and MDA-MB-435–2β cells showed significantly lower steady-state pHi values compared with control tumors. Studies of cells within a bioreactor system have shown that low pHi can result in an increase of GPC and a decrease of PC, which is most likely due to inhibition of GPC/GPE phosphodiesterase activity (22). Inhibition of GPC/GPE phosphodiesterase activity may explain in part the differences in PDE and PME levels for the control and transgene cancer cells (23,24). In the bioreactor system, however, inhibition of GPC/GPE phosphodiesterase activity occurred only for pHi lower than 7. Because pHi values in all of the tumors in our study were greater than 7, inhibition of GPC/GPE phosphodiesterase activity cannot explain entirely the differences in PDE and PME observed. The lower pHe values of the control tumors and the higher pHe values of transgene tumors formed by MDA-MB-435–1β and MDA-MB-435–2β cells are particularly interesting, because low pHe may enhance the invasive behavior of human breast carcinoma cells. An acidic pericellular pH, for instance, was found to increase the secretion of the active form of the lysosomal protease cathepsin B over time for human breast carcinoma cells (25). Human melanoma cells have been observed to secrete a higher level of 90-kDa gelatinase (a Type IV collagenase) at a pHe of 6.8 compared with pH 7.3 (26). This acid-induced secretion of gelatinase was blocked by cycloheximide, indicating that the enzyme induction was due to de novo synthesis. Thus, pH-related mechanisms may also play a role in facilitating invasion and metastasis in vivo for breast carcinoma cells that lack the nm23 gene.

Although the physiologic and metabolic effects detected in our study may alter invasive and metastatic behavior independently, it is also possible that they may be synergistic or necessary but not sufficient without the other. The results obtained here may open new opportunities for diagnosis/prognosis of metastatic dissemination as well as potential targeting of phospholipid metabolism and pH regulation for antimetastatic therapeutics. This is the first in vivo observation that links activity of a putative metastasis suppressor nm23 gene to metabolic processes. The results also demonstrate the potential of noninvasive NMR to detect forms of gene therapy for suppression of metastasis that may involve transfection of cells with nm23.

## ACKNOWLEDGMENTS

We thank Mr. G. Cromwell for transplanting the tumors and maintaining the cell lines and Ms. Noriko Mori for her assistance with preparing the extracts. This work was supported by USAMRMC grant DAMD17–96–1-6131 (Z.M.B.), DAMD17–94–4368 and CA58881–03 (R.J.G.), and DAMD17–96–6078 (J.M.B.).

## REFERENCES

1. Aznavoorian S, Murphy AN, Stetler-Stevenson WG, Liotta LA. Molecular aspects of tumor cell invasion and metastasis. Cancer 1993;71:1368–1383.
2. Steeg PS, Bevilaqua G, Kopper L, Thorgeirsson UP, Talmadge JE, Liotta LA, Sobel ME. Evidence for a novel gene associated with low tumor metastatic potential. J Natl Cancer Inst 1988;80:200–204.
3. De La Rosa A, Williams RL, Steeg PS. Nm23/nucleoside diphosphate kinase: toward a structural and biochemical understanding of its biological functions. Bioessays 1995;17:53–62.
4. MacDonald NJ, De La Rosa A, Steeg PS. The potential role of nm23 in cancer metastasis and cellular differentiation. Eur J Cancer 1995;31A: 1096–1100.
5. Urano T, Takamiya K, Furukawa K, Shiku H. Molecular cloning and functional expression of the second mouse nm23/NDP kinase gene, nm23-M2. FEBS Lett 1992;309:358–362.
6. Rosengard AM, Krutrzsch HC, Shearn A, Biggs JR, Barker E, Margulies IMK, King CR, Liotta LA, Steeg PS. Reduced NM23/Awd protein in tumor metastasis and aberrant *Drosophilia* development. Nature 1989; 342:177–180.
7. Stahl JA, Leone A, Rosengard AM, Porter L, King CR, Steeg PS. Identification of a second human nm23 gene, nm23-H2. Cancer Res 1991;51:445–449.
8. Ishikawa N, Shimada N, Munakaata Y, Watanabe K, Kimura N. Isolation and characterization of a gene encoding rat nucleoside diphosphate kinase. J Biol Chem 1992;267:14366–14372.
9. Shimada N, Ishikawa N, Munakata Y, Toda T, Watanabe K, Kimura N. A second form (b isoform) of nucleoside diphosphate kinase from rat. J Biol Chem 1993;268:2583–2589.
10. Kelsell D, Black D, Solomon E, Spur NK. Localization of a second nm23 gene, NME2, to chromosome 17q21–22. Genomics 1003;17:522–524.
11. Backer JM, Mendola CE, Kovesdi I, Fairhurst JL, O'Hara B, Shows TB, Mathews S, Murty VVS, Chaganti RSK. Chromosomal localization and nucleoside diphosphate kinase activity of human metastasis-suppressor NM23–1 and NM23–2. Oncogene 1993;8:497–502.
12. Backer JM, Mendola CE, Price J, Hamby CV. Effects of overexpression of nm23/NDPKs and their catalytically inactive mutants in MDA-MB-435 human breast carcinoma cells. In: Proceedings of the 87th Annual Meeting of American Association for Cancer Research, Washington, DC; 1996. Volume 37, p 78.
13. Gillies R, Liu Z, Bhujwalla ZM. $^{31}P$ MRS measurements of extracellular pH of tumors using 3-aminopropylphosphonate. Am J Physiol 1994;267: C195–C203.
14. Moon RB, Richards JH. Determination of intracellular pH by $^{31}P$ magnetic resonance. J Biol Chem 1973;248:7276–7278.
15. Evanochko WT, Sakkai TT, Ng TC, Krishna NR, Kim HD, Zeidler RB, Ghanta VK, Brockman RW, Schiffer LM, Braunschweiger PG, Glickson JD. NMR study of in vivo RIF-1 tumors: analysis of perchloric acid extracts and identification of $^{1}H$, $^{31}P$ and $^{13}C$ resonances. Biochim Biophys Acta 1984;805:104–116.
16. Dennis E. Diversity of group types, regulation and function of phospholipase A2. J Biol Chem 1994;269:13057.
17. Honn KV, Chen YQ. Prostacyclin, hydroxy fatty acids and cancer

metastasis. In: Rubanyi GM, Vane J, editors. Prostacyclin: new perspectives for basic research and novel therapeutic indications. Amsterdam: Elsevier Science; 1992. p 181–200.
18. Chen YO, Liu B, Tang DG, Honn KV. Fatty acid modulation of tumor cell-platelet-vessel wall interaction. Cancer Metast Rev 1992;11:389–410.
19. Fulton AM. The role of eicosanoids in tumor metastasis. Prostaglandins Leukotrienes Essential Fatty Acids 1988;34:229–237.
20. Karmali RA, Choi K, Otter G, Schmit F. Eicosanoids and metastasis: experimental aspects in Lewis lung carcinoma. Cancer Biochem Biophys 1986;9:97–104.
21. Kantor JD, McMormick B, Steeg PS, Zetter BR. Inhibition of cell motility after nm23 transfection of human and murine tumor cells. Cancer Res 1993;53:1971–1973.
22. Galons JP, Job C, Gillies RJ. Increase of GPC levels in cultured mammalian cells during acidosis: a $^{31}$P MR spectroscopic study using a continuous bioreactor system. Magn Reson Med 1995;33:422–426.
23. Daly PF, Lyon RC, Faustino PJ, Cohen JS. Phospholipid metabolism in cancer cells monitored by $^{31}$P NMR spectroscopy. J Biol Chem 1987;262: 14875–14878.
24. Daly PF, Zugmaier G, Sandler D, Carpen M, Myers CE, Cohen JS. Regulation of the cytidine phospholipid pathways in human cancer cells and effects of 1-beta-D-arabinofuranosylcytosine: a noninvasive $^{31}$P nuclear magnetic resonance study. Cancer Res 1990;50:552–557.
25. Rozhin J, Sameni M, Ziegler G, Sloane BF. Pericellular pH affects distribution and secretion of cathepsin B in malignant cells. Cancer Res 1994;54:6517–6525.
26. Kato Y, Nakayama Y, Umeda M, Miyazaka K. Induction of 103 kDa gelatinase/type IV collagenase by acidic culture conditions in mouse metastatic melanoma cell lines. J Biol Chem 1992;267:11424–11430.

[CANCER RESEARCH 59, 80–84, January 1, 1999]

# Malignant Transformation Alters Membrane Choline Phospholipid Metabolism of Human Mammary Epithelial Cells[1]

**Eric O. Aboagye and Zaver M. Bhujwalla[2]**

*The Johns Hopkins University School of Medicine, Division of Magnetic Resonance Research–Oncology Section, Department of Radiology, Baltimore, Maryland 21205*

## ABSTRACT

**Transduction of mitogenic signals in cells can be mediated by molecules derived from the synthesis and breakdown of the major membrane phospholipid, phosphotidylcholine. Studies were performed on human mammary epithelial cells in culture to understand the impact of malignant transformation and progression on membrane phospholipid metabolism. In the model system used here, phosphocholine levels and total choline-containing phospholipid metabolite levels increased with progression from normal to immortalized to oncogene-transformed to tumor-derived cells. These changes occurred independently of cell doubling time. A "glycerophosphocholine to phosphocholine switch" was apparent with immortalization. This alteration in phenotype of increased phosphocholine relative to glycerophosphocholine was observed in oncogene-transformed and for all human breast tumor cell lines analyzed. The results demonstrate that progression of human mammary epithelial cells from normal to malignant phenotype is associated with altered membrane choline phospholipid metabolism.**

## INTRODUCTION

PtC[3] is the most abundant phospholipid in biological membranes and together with other phospholipids, such as phosphatidylethanolamine and neutral lipids, form the characteristic bilayer structure of cells and regulate membrane integrity (1, 2). MCPM (Fig. 1), *i.e.,* biosynthesis and hydrolysis of PtC, are essential processes for mitogenic signal transduction events in cells (3–6). There is now increasing evidence to suggest that products of MCPM such as PCho, diacylglycerol, and arachidonic acid metabolites may function as second messengers essential for the mitogenic activity of growth factors particularly in the activation of the *ras-raf-1-MAPK* cascade and protein kinase C pathway (3–6). Together with inositol phospholipid metabolism, MCPM can also provide a sustained activation of mitogenic signal transduction via a positive feedback interaction (4, 7).

The regulation of MCPM can occur through growth factor stimulation (4, 5) or requirements for eicosanoid production.[4] There is now increasing evidence to suggest that the activity of key enzymes involved in MCPM are regulated by receptor tyrosine kinase cascade downstream of the *ras/raf* interaction (8, 9). This assertion is supported by the fact that activation of receptor tyrosine kinase growth factor-mediated signal transduction at the level of growth factor, *ras,* or *raf* produces an enhanced MCPM (8, 9). Because signal transduction events and genetic alterations involving amplification of oncogenes such as *erbB2* play a crucial role in the development of the normal breast, carcinogenesis of its epithelium, and progression of breast cancer, it is possible that regulation of the levels of choline-containing metabolites may be linked to malignant transformation and progression of the breast epithelium.

NMR has been used to study choline phospholipid metabolism in cells or excised tissues, as well as noninvasively *in vivo* (10–13). Depending on the experimental conditions, $^1$H NMR methods can detect either individual choline phospholipid metabolites or a peak corresponding to total choline-containing metabolites. Using $^1$H NMR, invasive cancer could be distinguished from benign breast lesions by the high total choline phospholipid metabolite levels in the former (10). In another study, increased choline phospholipid metabolite levels characterized two cancer cell lines (MCF-7 and T47D) compared with that of a normal HMEC line; there were no distinct differences in high energy phosphates and the rates of glucose consumption and aerobic glycolysis (14). These studies support the existence of differences in phosphatidylcholine metabolism between normal epithelial cells and cancer cells *in vitro* and between benign and malignant cells *in vivo*. The possibility of differential regulation of MCPM in normal *versus* tumor cells suggests a diagnostic role for enhanced MCPM and has implications for therapeutic intervention.

Despite the indication of an altered MCPM in breast cancer cells, no attempt has been made to systematically relate the multistep process of carcinogenesis to altered MCPM in mammary epithelial cells. To address this issue, we have assessed PCho, GPC, and choline levels in a number of epithelial cell lines derived from reduction mammoplasty (normal) tissues and neoplastic lesions and also investigated the effects of immortalization and oncogene transformation on MCPM. Such a model has been used previously by other workers to evaluate the stepwise progression in mammary epithelium from normal to malignant phenotype (15–20). Our data suggest that phenotypic changes in MCPM probably commence early in carcinogenesis and may, as with most other neoplastic phenotypes, be regulated by an interplay of cellular immortalization and oncogene transformation.

## MATERIALS AND METHODS

**Cell Lines.** HMECs used in this study include finite life span HMEC strains 184 and 48, derived from reduction mammoplasty tissues; nontumorigenic immortal cell lines 184A1 and 184B5, derived from benzo(*a*)pyrene-treated 184 cells; and the 184B5-*erbB2* cell line, derived from 184B5 by transfection with the *erbB2* oncogene. All of the above cell lines were obtained from Dr. Martha Stampfer (Lawrence Berkeley National Laboratory, Berkeley, CA) and cultured in MCDB 170 media supplemented as described previously (21, 22). MCF-12A, a spontaneously immortalized cell line established from MCF-12M mortal cells (23), was obtained from American Type Culture Collection (Rockville, MD) and cultured in DMEM-Ham's F12 medium supplemented as described previously (23). All of the human breast cancer cell lines were derived from pleural effusions in patients with breast cancer and were obtained from American Type Culture Collection. The tumor-derived cell lines were all cultured in DMEM-Ham's F12 medium supplemented with 10% fetal bovine serum.

**Growth Rate and Cell Size.** The growth rate of the cell lines used in this study were determined using the MTT assay (24). Briefly, cells ($5 \times 10^3$) were plated in 24-well plates in 1 ml of media and incubated under normal culture conditions for up to 6 days. To estimate cell number, the cells were incubated with MTT (Sigma Chemical Co., St. Louis, MO) for 4 h. MTT was then removed, and the resulting formazan crystals were dissolved in 1 ml of DMSO and 125 $\mu$l of glycine buffer (pH 10.5; Ref. 24). The UV absorbance of the

Received 6/18/98; accepted 10/28/98.

The costs of publication of this article were defrayed in part by the payment of page charges. This article must therefore be hereby marked *advertisement* in accordance with 18 U.S.C. Section 1734 solely to indicate this fact.

[1] This work was supported by USAMRMC Grant DAMD-17-96-16131.

[2] To whom requests for reprints should be addressed, at The Johns Hopkins University School of Medicine, Division of Magnetic Resonance Research–Oncology Section, Department of Radiology, 208C Traylor Building, 720 Rutland Avenue, Baltimore, MD 21205.

[3] The abbreviations used are: PtC, phosphatidylcholine; MCPM, membrane choline phospholipid metabolism; PCho, phosphocholine; GPC, glycerophosphocholine; NMR, nuclear magnetic resonance; HMEC, human mammary epithelial cell; MTT, 3-(4,5-dimethylthiazol-2-yl)-2,5-diphenyltetrazolium bromide; TSP, trimethylsilylpropionate.

[4] Z. M. Bhujwalla and E. O. Aboagye, unpublished data.

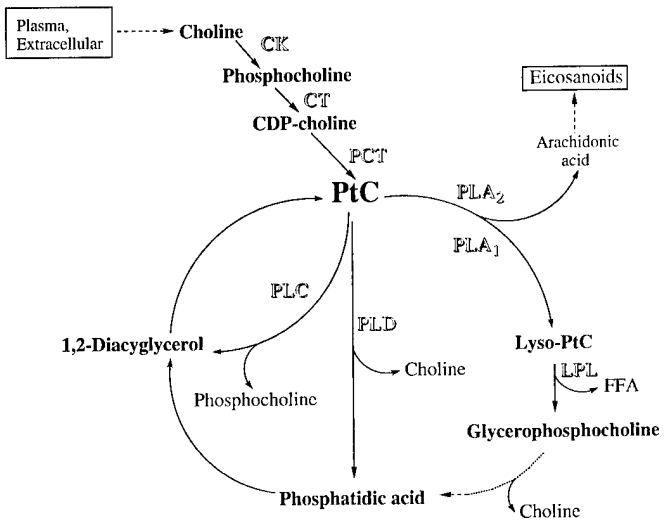


Fig. 1. Biosynthesis and hydrolysis of PtC. Phosphorylation of choline to PCho by choline kinase (*CK*) is the first step in the biosynthesis of PtC. PCho is then converted to PtC via intermediates involving the rate-limiting enzyme CTP: phosphocholine cytidyltransferase (*CT*) and phosphocholine transferase (*PCT*). Hydrolysis of PtC is effected by three major PtC-specific enzymes, phospholipase C (*PLC*), phospholipase D (*PLD*), and phospholipase $A_1$ and $A_2$ ($PLA_1$ and $PLA_2$). *FFA*, free fatty acid.

formazan solution was recorded at 553 nm (λmax). Four replicates were used to calculate the cell doubling time for each cell line. Because the cells had different morphologies and diameters, the cell size was determined for each cell line by trypsinizing the cells and counting the diameter of 20 random cells using an optical microscope.

**Extraction.** To determine the choline phospholipid metabolite content, cells growing in culture were fed with fresh media 24 h before extraction and used at 70–80% confluency. Cells ($10^7$ to $10^8$) were trypsinized, washed twice with normal saline, and homogenized with ice-cold 8% perchloric acid (5 ml). The homogenates were centrifuged (15000 rpm for 15 min at 4°C), and the supernatants were neutralized with 3 M $K_2CO_3$/1 M KOH buffer. The samples were again clarified by centrifugation, treated with ~50 mg Chelex (Sigma) to remove divalent ions, lyophilized, and resuspended in 0.5 ml of $D_2O$ for NMR analysis. Trimethylsilyl propionate (5 μl) was used as an internal standard. $^1H$ NMR spectra of the extracts were acquired on a 11.7T Bruker NMR spectrometer with a 5-mm probe. Fully relaxed spectra (without saturation effects) were obtained using the following acquisition parameters: 30° flip angle, 6000 Hz sweep width, 4.7 s repetition time, 32 K block size, and 512 scans. The data were analyzed using an in-house software, Soft Fourier Transform (P. Barker, The Johns Hopkins University). PCho, GPC, and total choline-containing (PCho + GPC + choline) metabolite levels were determined and normalized to cell size. Between three and five independent extracts were analyzed per cell line.

The reason for normalizing metabolite levels to cell size was due to differences in cell size between the cell lines used in this study. This necessitated normalization to either cell size or protein concentration. The former requires fewer cells and is therefore suited to experiments with mortal cells, which senesce after 5 to 18 passages. To determine concentrations, peak amplitudes for choline PCho, GPC, and total choline-containing metabolites (PCho + GPC + choline) were compared with that of the internal standard TSP according to the equation:

$$[\text{metabolite}] = \text{Amplitude}_{(\text{metabolite})} \times \frac{[\text{TSP}]}{\text{Amplitude}_{(\text{TSP})} \times \text{cell number} \times \text{cell volume}}$$

where [metabolite] is concentration of the metabolite expressed as fmol/$\mu m^3$, [TSP] is the molar concentration of TSP used, and cell volume ($\mu m^3$) was calculated from the radius of the cell according to the equation, volume = $4/3 \times \pi r^3$. For this equation to be valid, it is necessary that spectra are fully relaxed, as was the case here, or to correct for saturation.

**Statistical Analysis.** Statistical analysis of the data were performed using StatView II version 1.04, 1991 (Abacus Concepts, Inc., Berkeley, CA). The statistical significance of differences in metabolite levels between cell lines was determined using the Mann-Whitney *U* test. *P*s of ≤ 0.05 were considered to be significant.

## RESULTS

**Identification of Phospholipid Metabolites by $^1H$ NMR.** $^1H$ NMR of perchloric acid extracts demonstrated the presence of three water-soluble, choline-containing [-$N(CH3)_3$] metabolites, *i.e.*, choline, PCho, and GPC (Fig. 2). These metabolites resonate at ~3.2 ppm downfield of the internal standard and chemical shift reference TSP. Peak assignments were performed with authentic compounds. Ten epithelial cell lines of mammary origin were characterized by this method; the phenotype and cell size of these cell lines are indicated in Table 1.

**The "GPC to PCho Switch" in Mammary Epithelial Cells.** Analysis of individual choline metabolites uncovered an early alteration in MCPM that was linked to immortalization and malignant transformation, the "GPC to PCho switch" (Fig. 3). In Fig. 3 it is evident that GPC was the major choline metabolite in the finite life span HMEC strains 48 and 184. Thus, these cells showed a low PCho:GPC ratio of <1. Immortalization of cells, however, resulted in variable effects. The spontaneously immortalized cell line MCF-12A showed a similar phenotype (PCho:GPC) as the finite life span cells; we do not have the finite life span cells from which MCF-12A was established for comparison. In contrast, the benzo(*a*)pyrene-immortalized cell lines showed a GPC to PCho switch, *i.e.*, PCho was now the major choline metabolite. Of interest, the two immortal lines derived from the 184 strain showed variable degrees of this altered MCPM; 184A1 had a higher PCho:GPC level compared with 184B5. Forced overexpression of normal *erbB2* gene into 184B5 cells dramatically increased the PCho:GPC ratio in this cell line. The altered GPC to PCho switch was detected in all breast cancer cell lines analyzed.

**Breast Cancer Cells Have a High Choline Content.** Fig. 4 shows that there was a gradual increase in both PCho levels and total choline-containing metabolite levels as cells progressed from normal to malignant phenotype (normal < immortal < oncogene-transformed < tumor-derived). GPC levels also increased, albeit to a lesser extent than PCho levels and total choline-containing metabolite levels. It is worth noting that despite the GPC to PCho switch, total choline-

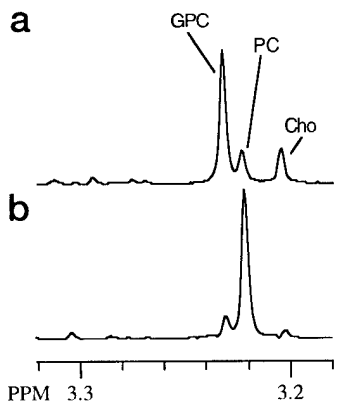


Fig. 2. Typical $^1H$ NMR spectra obtained from perchloric acid extracts of MCF-12A (*a*) and MDA-MB-231 (*b*) breast cancer cells grown in culture. The spectra, expanded to show the choline-containing metabolite region, represent qualitative differences between the two cell lines, *i.e.*, not normalized to display comparable signal-to-noise levels. Spectral assignments include GPC (3.234 ppm), PCho (3.225 ppm), and free choline (*Cho*; 3.207 ppm).

Table 1 *Phenotype and size of cell lines used in this study*

| Cell types | Phenotype[a] | Cell volume[b] ($\times 10^3$ $\mu m^3$) |
|---|---|---|
| Normal HMECs | | |
| 184 | Senescent, ADG | 36.5 ± 6.8 |
| 48 | Senescent, ADG | 11.1 ± 3.1 |
| Spontaneously immortalized HMECs | | |
| MCF-12A | Immortal, ADG | 9.8 ± 1.8 |
| Benzo(*a*)pyrene-immortalized HMECs | | |
| 184A1 | Immortal, ADG | 7.1 ± 0.9 |
| 184B5 | Immortal, ADG | 7.7 ± 0.9 |
| Oncogene-transformed HMECs | | |
| 184B5-*erbB2* | Immortal, AIG, forms low frequency, high latency tumors | 7.0 ± 0.8 |
| Breast cancer cells | | |
| SKBR3 | AIG, tumorigenic, low metastaticity | 21.9 ± 7.3 |
| MCF7 | AIG, tumorigenic, low metastaticity | 6.7 ± 1.5 |
| MDA-MB-231 | AIG, tumorigenic, highly metastatic | 8.4 ± 1.4 |
| MDA-MB-435 | AIG, tumorigenic, highly metastatic | 3.5 ± 0.4 |

[a] ADG, anchorage-dependent growth; AIG, anchorage-independent growth.
[b] Mean ± SE.

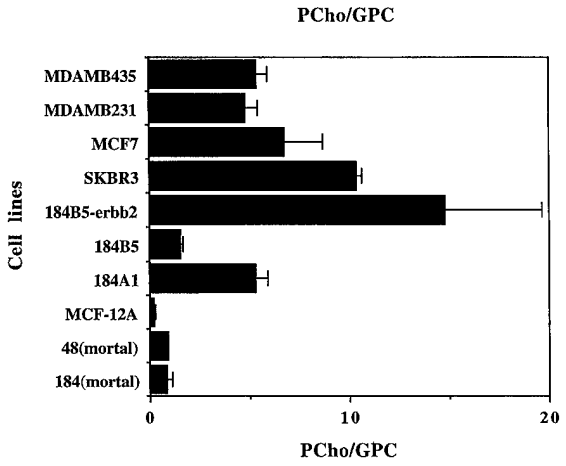


Fig. 3. PCho:GPC ratios in a panel of cell lines representing various stages of breast carcinogenesis. There was a statistically significant difference in PCho:GPC ratio ($P < 0.05$) between finite life span *versus* tumor-derived cells, 184 strain *versus* 184A1 cell line, and 184B5 *versus* 184B5-*erbB2* cell lines. The *P* for 184 strain *versus* 184B5 cell line was 0.1. *Bars,* SE.

containing metabolite levels and PCho levels in immortalized cell lines such as 184A1, which was nontumorigenic, and 184B5-erbB2, which exhibited low tumorigenicity, were significantly lower than any of the tumorigenic breast cancer cells.

**Are the High Choline Phospholipid Metabolite Levels in Breast Cancer Cells a Function of Their Rate of Cellular Proliferation?** It is generally thought that the increase in phosphomonoester (mainly PCho and phosphoethanolamine) metabolite levels in cancer cells is due to their intensified cell membrane synthesis to cope with rapid growth and proliferation (12, 25). This assertion is supported, for instance, by the work of Smith *et al.* (26), where an increase in PCho and a decrease in GPC correlated strongly with tumor growth rate. Thus, we tested the hypothesis that increased PCho:GPC levels, PCho, GPC, or total-choline containing metabolite levels may be the result of high proliferation. A systematic measurement of cell doubling time in all of the cell lines revealed that there was no overall correlation between cell doubling time and PCho:GPC ratio, PCho levels, GPC levels, or total choline-containing metabolite levels (Fig. 5; $r < 0.2$; $P > 0.1$). For instance, MCF-12A cells exhibited a doubling time in culture comparable with the tumorigenic cell line MDA-MB-435. However, MCF-12A cells exhibited a significantly lower PCho:GPC ratio, a low level of total choline-containing metabolites, and low PCho compared with MDA-MB-435 cells.

## DISCUSSION

Carcinogenesis of the mammary epithelium occurs though a multistep process involving genetic alterations, amplification of oncogenes, and loss of tumor suppressor function (27, 28). The stages of

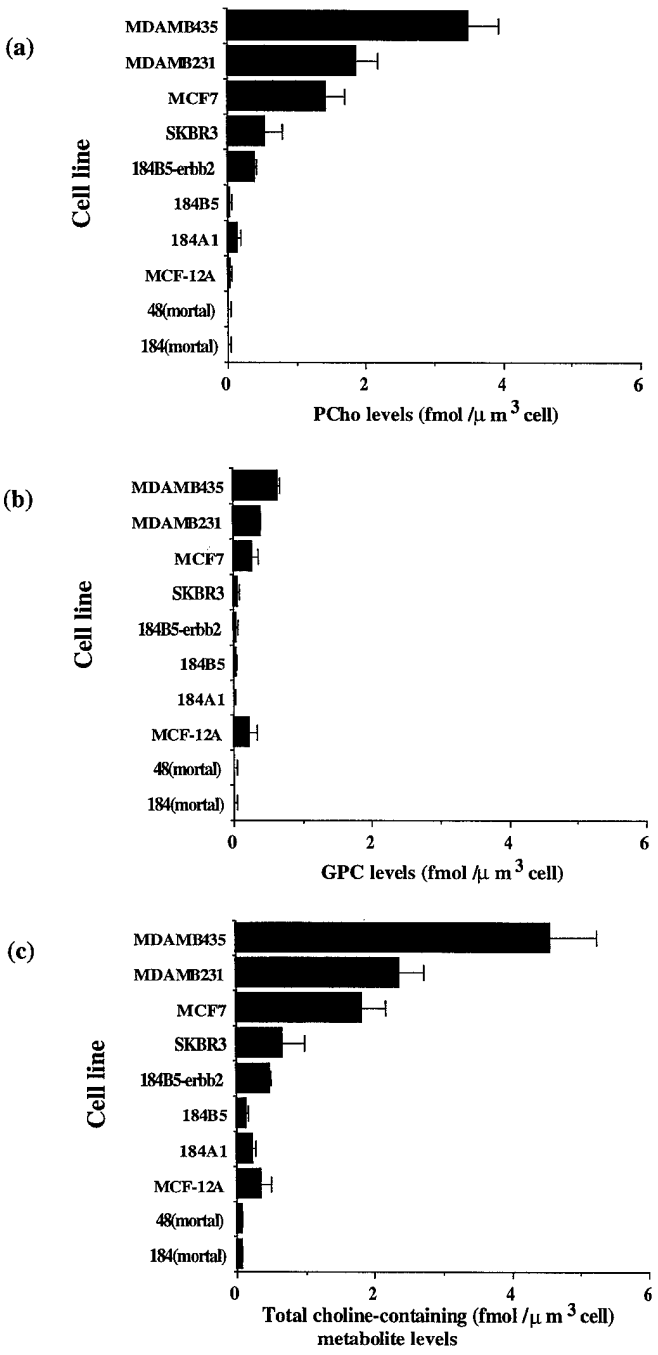


Fig. 4. PCho levels (*a*), GPC levels (*b*), and total choline-containing metabolite (PCho + GPC + choline) levels (*c*) in a panel of cell lines representing various stages of breast carcinogenesis. There was a statistically significant difference in total choline-containing metabolite levels and PCho levels ($P < 0.05$) for finite life span cells *versus* tumor-derived cells; 184 strain *versus* 184A1; 184B5 *versus* 184B5-*erbB2*; MDA-MB-435 *versus* MDA-MB-231, MCF7, and SKBR3; MDA-MB-231 *versus* SKBR3; and MCF7 *versus* SKBR3. There was a statistically significant difference in GPC levels for finite life span cells, 184A1, 184B5 and 185B5-*erbB2*, and SKBR3 *versus* MDA-MB-435, MDA-MB-231, MCF7, and MCF-12A cells. *Bars,* SE.

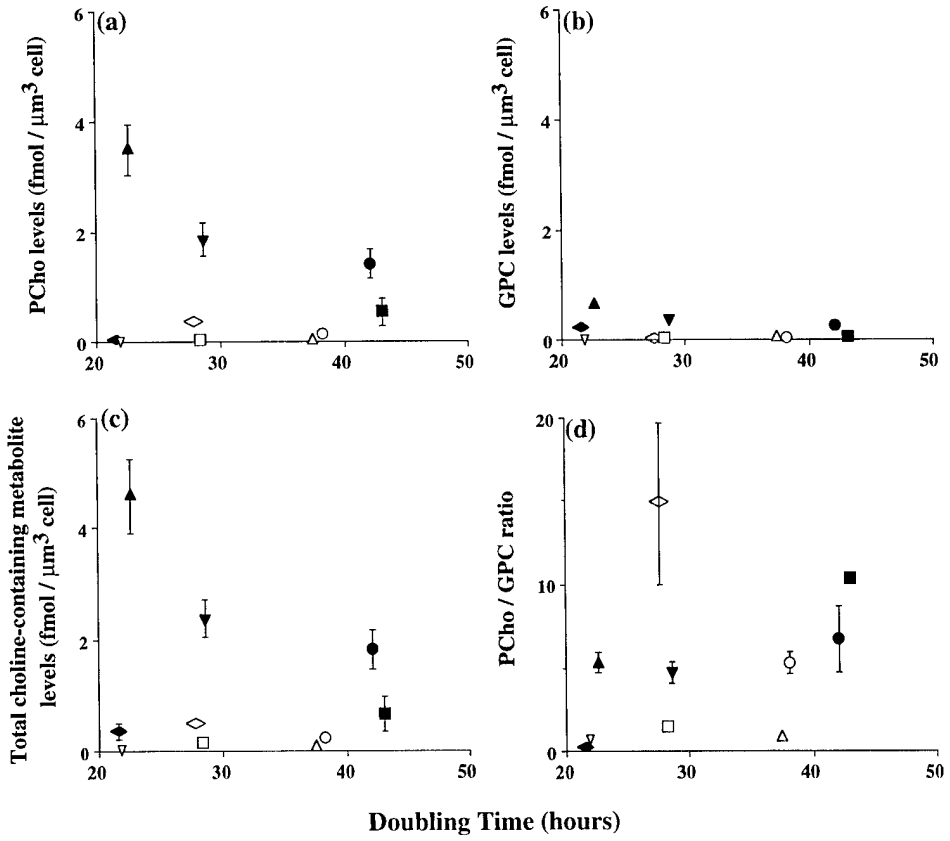


Fig. 5. The relationship between doubling time and PCho levels (*a*), GPC levels (*b*), total choline-containing metabolite levels (PCho + GPC + choline; *c*), and PCho:GPC ratio (*d*). Doubling times were measured by the MTT assay (see "Materials and Methods") and increased in the order MCF-12A > 48 (mortal) > MDA-MB-435 > 184B5-erbB2 > 184B5 > MDA-MB-231 > 184 (mortal) > 184A1 > MCF-7 > SKBR3; ▲, MDA-MB-435; ▼, MDA-MB-231; ●, MCF-7; ■, SKBR3; ♦, MCF-12A; △, 184 (mortal); ▽, 48 (mortal); ○, 184A1; □, 184B5; ◇, 184B5-*erbB2*. *Bars*, SE.

carcinogenesis can broadly be classified as transformation of normal cells to benign hyperplasia followed by atypical hyperplasia, which progresses to carcinoma *in situ* and finally to infiltrating carcinoma with or without metastasis to distant sites. *In vitro* models based on immortalization and oncogene transformation of normal HMECs have been developed to study mammary carcinogenesis (15–20). These immortalized, oncogene-transformed, and cancer cells show differences in phenotypes that differentiate normal cells from immortal/malignant cells, such as karyotype, vimentin/uvomorulin expression, responsiveness to transforming growth factor $\beta$, telomere length/telomerase expression, activating protein 1 transcription factor activity, as well as anchorage-dependent/independent growth, and ability to form tumors in immune-deficient mice.

We have investigated the association between malignant carcinogenic processes and MCPM by monitoring the three choline phospholipid metabolites (choline, PCho, and GPC) in 10 cell lines, which represent different stages of malignant progression. Our findings suggest that normal human mammary epithelium has low steady-state levels of total choline-containing metabolites. In addition to their low total choline-containing metabolite levels, we also demonstrated that GPC was the major metabolite in the normal HMECs. A GPC to PCho switch appeared to be an early phenotypic change during carcinogenesis, as observed in benzo(*a*)pyrene-immortalized cells and where instead of GPC, PCho became the major choline phospholipid metabolites. However, despite this "switch," total choline-containing metabolite levels remained low in these immortalized cells. Transformation of 184B5 immortal cells by forced overexpression of the *erbB2* oncogene, however, resulted in a dramatic increase in both PCho:GPC ratio and total choline levels compared with the benzo(*a*)pyrene-immortalized cells. However, total choline-containing metabolites and PCho levels were still less than those of tumor-derived cells. *erbB2* is an important (proto)oncogene that is amplified in 20–30% of breast cancer cases and is associated with poor prognosis; amplification of this oncogene is thought to occur late in tumor progression (27–30). Transformation of 184B5 by this gene results in the ability of these cells to form colonies in semisolid medium and to form small, low frequency tumors with high latency *in vivo* (16). Our data with *erbB2* demonstrate a new and heretofore unknown metabolic role for *erbB2* and support the possibility that growth factor-mediated activation of the tyrosine kinase cascade (involving receptor-*grb 2-sos-ras-raf-1-MEK-MAPK*) can lead to an increase in PCho levels (6–9). In general, the levels and expression of receptors and proteins involved in the growth factor receptor-tyrosine kinase pathway tend to increase with malignancy. For instance, levels of epidermal growth factor receptor are low in the 184 strain, moderately high in 184A1, 184B5, and 184B5-*erbB2* cells, and very high in MDA-MB-231 cells (19, 31). In addition, Daly *et al.* (32) reported up-regulation of *grb2* mRNA/protein and the *ras* signaling pathway in MCF-7 and MDA-MB-231 cells compared with normal HMECs.

All of the breast tumor cell lines showed the GPC to PCho switch. In addition to this switch, all breast tumor cells showed significantly higher total choline-containing metabolite levels ($P < 0.05$). The increased total choline-containing metabolite levels were mainly due to an increase in PCho levels and, to a lesser and variable extent, an increase in GPC levels. There was a gradual increase in both total choline-containing metabolite levels and PCho levels as the cells acquired malignant phenotype (normal < immortal < oncogene-transformed < tumor-derived), with the highly invasive metastatic cell lines showing the highest levels. The high total choline content in the tumorigenic cells may be related to the multiple genetic changes that are associated with the multistep process of carcinogenesis (28) and may explain the progressive ability of these cells to gain

anchorage-independent growth, form primary tumors in immune compromised mice, and finally to metastasize. Our studies confirm the work of Ting *et al.* (14), who showed for a limited number of cell lines that levels of choline-containing metabolites were low in a normal mammary epithelial strain and high in two tumor-derived cell lines. Our results also support recent clinical observations that the total choline peak is higher for malignant lesions than for benign ones (10).

It has been postulated that the rapid growth and proliferation of cancer cells and increased membrane/fatty acid requirements may be responsible for the high choline phospholipid metabolite levels in cancer *versus* normal tissues (12, 25, 26); the same argument could be made for benign lesions *versus* invasive cancers. However, the data presented here and that of Ting *et al.* (14) show that choline-containing metabolite levels remain low in normal HMECs in culture when the cells are proliferating at approximately similar rates as tumor-derived cells and suggest that although proliferation-related changes may occur (26), the rate of proliferation *per se* cannot completely account for the increased choline phospholipid metabolism. In this study, we have demonstrated that an alteration in MCPM is linked to malignant transformation and progression of mammary epithelium. Presently, the exact mechanisms underlying the altered metabolism are unknown. Possible mechanisms include activation of enzymes involved in MCPM, such as via enhanced receptor tyrosine kinase cascade (9), or differential induction of choline kinase isozymes, as reported previously for carcinogen-treated rat liver (33). Other possible mechanisms that need to be investigated include amplification of choline kinase, phospholipase C, phospholipase D, and phospholipase A genes during carcinogenesis.

To conclude, the major finding to emerge from the present study is that choline phospholipid metabolite levels progressively increase in cultured HMECs as cells become more malignant. We therefore propose that carcinogenesis in human breast epithelial cells results in progressive alteration of membrane choline phospholipid metabolism. This work is relevant to diagnosis of breast cancer and also provides a rationale for selective pharmacological intervention.

## ACKNOWLEDGMENTS

We are very grateful to Dr. Martha Stampfer of Berkeley National Laboratory (Berkeley, CA) for kindly donating the HMECs used in this study and for very useful suggestions. We gratefully acknowledge the expert technical assistance of Dr. V. P. Chacko in performing the NMR spectroscopy experiments, and we thank N. Mori for assistance with the cell doubling time measurements.

## REFERENCES

1. Cullis, P. R., and Hope, M. J. Physical properties and functional roles of lipids in membranes. *In:* D. E. Vance and J. Vance (ed.), Biochemistry of Lipids, Lipoproteins and Membranes, pp. 1–41. Amsterdam: Elsevier Science Publishers, 1991.
2. Mountford, C. E., and Wright, L. C. Organization of lipids in the plasma membranes of malignant and stimulated cells: a new model. Trends Biochem. Sci., *13:* 172–177, 1988.
3. Cuadrado, A., Carnero, A., Dolfi, F., Jimenez, B., and Lacal, J. C. Phosphorylcholine: a novel second messenger essential for mitogenic activity of growth factors. Oncogene, *8:* 2959–2968, 1993.
4. Exton, J. H. Phosphatidylcholine breakdown and signal transduction. Biochim. Biophys. Acta, *1212:* 26–42, 1994.
5. Pelech, S. L., and Vance, D. E. Signal transduction via phosphatidylcholine cycles. Trends Biochem. Sci., *14:* 28–30, 1989.
6. Cai, H., Erhardt, P., Troppmair, J., Diaz-Meco, M. T., Sithanandam, G., Rapp, U. R., Moscat, J., and Cooper, G. M. Hydrolysis of phosphatidylcholine couples Ras to activation of Raf protein kinase during mitogenic signal transduction. Mol. Cell. Biol., *13:* 7645–7651, 1993.
7. Exton, J. H. Cell signalling through guanine-nucleotide-binding regulatory proteins (G proteins) and phospholipases. Eur. J. Biochem., *243:* 10–20, 1997.
8. Carnero, A., Cuadrado, A., del Peso, L., and Lacal, J. C. Activation of type D phospholipase by serum stimulation and ras-induced transformation in NIH3T3 cells. Oncogene, *9:* 1387–1395, 1994.
9. Ratnam, S., and Kent, C. Early increase in choline kinase activity upon induction of the H-*ras* oncogene in mouse fibroblast cell lines. Arch. Biochem. Biophys., *323:* 313–322, 1995.
10. Mackinnon, W. B., Barry, P. A., Malycha, P. L., Gillett, D. L., Russell, P., Lean, C. L., Doran, S. T., Barraclough, B. H., Bilous, M., and Mountford, C. Fine-needle biopsy specimen of benign breast lesions distinguished from invasive cancer *ex vivo* with proton MR spectroscopy. Radiology, *204:* 661–666, 1997.
11. Podo, F. Detection of phosphatidylcholine-specific phospholipase C in NIH-3T3 fibroblast and H-ras transformants: NMR and immunochemical studies. Anticancer Res., *19:* 1399–1412, 1996.
12. Ruiz-Cabello, J., and Cohen, J. S. Phospholipid metabolites as indicators of cancer cell function. NMR Biomed., *5:* 226–233, 1992.
13. Rutter, A., Mackinnon, W. B., Huschtscha, L. I., and Mountford, C. E. A proton magnetic resonance spectroscopy study of aging and transformed human fibroblasts. Exp. Gerontol., *31:* 669–686, 1996.
14. Ting, Y-L. T., Sherr, D., and Degani, H. Variations in energy and phospholipid metabolism in normal and cancer human mammary epithelial cells. Anticancer Res., *16:* 1381–1388, 1996.
15. Stampfer, M. R., and Bartley, J. C. Induction of transformation in continuous cell lines from normal human mammary epithelial cells after exposure to benzo(*a*)pyrene. Proc. Natl. Acad. Sci. USA, *82:* 2394–2398, 1985.
16. Pierce, J. H., Arnstein, P., DiMarco, E., Artrip, J., Kraus, M. H., Lonardo, F., DiFiore, P. P., and Aaronson, S. A. Oncogenic potential of erbB-2 in human mammary epithelial cells. Oncogene, *6:* 1189–1194, 1991.
17. Thompson, E. W., Torri, J., Sabol, M., Sommers, C. L., Byers, S., Valverius, E. M., Martin, G. R., Lippman, M. E., Stampfer, M. R., and Dickson, R. B. Oncogene-induced basement membrane invasiveness in human mammary epithelial cells. Clin. Exp. Metastasis, *12:* 181–194, 1994.
18. Valverius, E., Bates, S. E., Stampfer, M., Clark, R., McCormick, F., Salomon, D. S., Lippman, M. E., and Dickson, R. B. Transforming growth factor $\alpha$ and its receptor in human mammary epithelial cells: modulation of epidermal growth factor receptor function with oncogenic transformation. Mol. Endocrinol., *3:* 203–214, 1989.
19. Smith, L. M., Birrer, M. J., Stampfer, M. R., and Brown, P. H. Breast cancer cells have lower activating protein 1 transcription factor activity than normal mammary epithelial cells. Cancer Res., *57:* 3046–3054, 1997.
20. Stampfer, M. R., Bodnar, A., Garbe, J., Wong, M., Pan, A., Villeponteau, B., and Yaswen, P. Gradual phenotypic conversion associated with immortalization of cultured human mammary epithelial cells. Mol. Biol. Cell., *8:* 2391–2405, 1997.
21. Stampfer, M. R. Isolation and growth of human mammary epithelial cells. J. Tissue Culture Methods, *9:* 107–116, 1985.
22. Stampfer, M. R., and Yaswen, P. Culture systems for study of human mammary epithelial cell proliferation, differentiation and transformation. Cancer Surv., *18:* 7–34, 1994.
23. Paine, T. M., Soule, H. D., Pauley, R. J., and Dawson, P. J. Characterization of epithelial phenotypes in mortal and immortal human breast cells. Int. J. Cancer, *50:* 463–473, 1992.
24. Plumb, J. A., Milroy, R., and Kaye, S. B. Effects of pH dependence of 3-(4,5-dimethylthiazole-2-yl)-2,5-diphenyltetrazolium bromide-formazan absorption on chemosensitivity determined by a novel tetrazolium-based assay. Cancer Res., *49:* 4435–4440, 1989.
25. Negendank, W. Studies of human tumors by MRS: a review. NMR Biomed., *5:* 303–324, 1992.
26. Smith, T. A. D., Eccles, S., Ormerod, M. G., Tombs, A. J., Titley, J. C., and Leach, M. O. The phosphocholine and glycerophosphocholine content of oestrogen-sensitive rat mammary tumor correlates strongly with growth rate. Br. J. Cancer, *64:* 821–826, 1991.
27. Dickson, R. B., Salomon, D. S., and Lippman, M. E. Tyrosine kinase receptor-nuclear protooncogene interaction in breast cancer. Cancer Treat. Res., *61:* 249–273, 1992.
28. Beckman, M. W., Niederacher, D., Schnurch, H. G., Guesterson, B. A., and Bender, H. G. Multistep carcinogenesis of breast cancer and tumor heterogeneity. J. Mol. Med., *1997:* 429–437, 1993.
29. Adnane, J., Gaudray, P., Simon-Lafontaine, J., Jeanteur, P., and Theillet, C. Proto-oncogene amplification and breast cancer phenotype. Oncogene, *4:* 1389–1395, 1989.
30. Slamon, D. J., Clark, G. M., Wong, S. G., Levin, W. J., Ullrich, A., and McGuire, W. L. Human breast cancer: correlation of relapse and survival with amplification of the *HER-2/neu* oncogene. Science (Washington DC), *235:* 177–182, 1987.
31. de Cremoux, P., Gauville, C., Closson, V., Linares, G., Calvo, F., Tavitian, A., and Olofsson, B. EGF modulation of the *ras*-related *rhoB* gene expression in human breast cancer cell lines. Int. J. Cancer, *59:* 408–415, 1994.
32. Daly, R. J., Binder, M. D., and Sutherland, R. L. Overexpression of the *Grb* gene in human breast cancer cell lines. Oncogene, *9:* 2723–2727, 1994.
33. Tadokoro, K., Ishidate, K., and Nakazawa, Y. Evidence for the existence of isozymes of choline kinase and their selective induction in 3-methylcholanthrene- or carbon tetrachloride-treated rat liver. Biochim. Biophys. Acta, *835:* 501–513, 1985.

*Advan. Enzyme Regul.*, Vol. 41, pp. 251–260, 2001

Printed in Great Britain
0065-2571/01/$ - see front matter

PERGAMON
www.elsevier.com/locate/advenzreg

PII: S0065-2571(00)00019-4

# EFFECT OF MALIGNANT TRANSFORMATION ON LACTATE LEVELS OF HUMAN MAMMARY EPITHELIAL CELLS

ERIC O. ABOAGYE,* NORIKO MORI and ZAVER M. BHUJWALLA

MR Oncology Section, Division of MR Research, Department of Radiology, The Johns Hopkins University School of Medicine, Rm 208C Traylor Building, 720, Rutland Avenue, Baltimore, MD 21205, USA

## INTRODUCTION

In 1930 Warburg published the first report indicating that tumors have a unique property distinct from normal tissues in undergoing aerobic glycolysis and producing lactate, the "Warburg effect" (1). Since then researchers have sought to understand why tumors acquire this phenotype (2). Lactate is produced during glycolysis from pyruvate by the action of lactate dehydrogenase (LDH; EC 1.1.1.27) (2–4). It has been observed that most of the lactate pool is metabolically active (5). Both lactate and LDH-A isozyme levels have been used as markers of malignancy, with high levels indicating a more malignant phenotype (6, 7).

Some of the regulatory mechanisms responsible for this phenotype have been characterized in tumors and cell lines. For instance, using a panel of hepatomas with different growth rates, Weber concluded that the increased glycolysis in tumors could be due to re-programming of gene expression which entails increased activities and amounts of the key glycolytic enzymes, hexokinase (EC 2.7.1.1), phosphofructokinase (EC 2.7.1.11) and pyruvate kinase (EC 2.7.1.40), with a concomitant decrease in activities of gluconeogenic enzymes (2, 3). These studies demonstrated that well differentiated tumors did not have high lactate levels (2, 3). Furthermore, lactate production was not correlated with LDH activity, suggesting that LDH was present in great excess (2). More recently, Shim and coworkers implicated the *myc* oncogene in the induction of the high lactate phenotype (8). In that study overexpression of the *c-myc* oncogene in Rat1a fibroblast cells led to transactivation of LDH-A, whose expression increases lactate production, and was necessary for *c-myc*-mediated transformation (8). *Myc*

*Corresponding author. Present address: MRC Cyclotron Unit, Hammersmith Hospital, DuCane Road, London W12 0NN, UK.

heterodimerizes with *max*, to bind the core carbohydrate response element 5′-CACGTC-3′ (9). Another important regulator of glycolysis is the basic helix–loop–helix transcription factor, hypoxia-inducible factor-1 (HIF-1) (9). HIF-1 binds to the DNA sequence 5′-RCGTG-3′ and increases the expression of genes that encode the glucose transporters GLUT I/III, and glycolytic enzymes including hexokinase, aldolase A (EC 4.1.2.13), enolase 1 (EC 4.2.1.11), phosphofructokinase L, phosphoglycerate kinase 1 (EC 2.7.2.3), pyruvate kinase M and LDH-A (9). Furthermore, a number of other oncogene and tumor suppressor gene products including von Hippel–Lindau protein (pVHL), *v-src*, and *H-ras* may act directly or via HIF-1 to activate these glycolytic enzymes (9, 10). This suggests that, in tumors, hypoxia could regulate lactate levels via activation of HIF-1. Increased oxygenation during tumor response, on the other hand, could explain the decrease in lactate levels that characterizes tumor response to therapy (11–13). Whether these gene products and transcription factors act independently or through direct/indirect interaction in tumors *in vivo* remains to be determined and is currently the subject of active research in a number of laboratories.

An important question for diagnosis and response assessment, which remains to be addressed, is when do cells acquire the high lactate phenotype? To understand the relationship between the multi-step process of carcinogenesis and regulation of lactate levels, we have studied a series of HMECs representing various stages of transformation including normal (senescent/mortal) cells, spontaneously/benzo(a)pyrene immortalized cells, *erbB2* oncogene transformed immortalized cells, and tumor-derived cells. Such models have been used previously to determine the stepwise progression in mammary epithelium from normal to malignant phenotype (14–19). We also studied the activities of LDH in selected cell lines to see if the changes in lactate levels were associated with changes in LDH activity.

## MATERIALS AND METHODS

*Cell lines.* The HMECs used in this study include finite lifespan HMEC strains 184 and 48, derived from reduction mammoplasty tissues; non-tumorigenic immortal cell lines 184A1 and 184B5, derived from benzo(a)-pyrene treated 184 cells; and the 184B5-*erbB2* cell line, derived from 184B5 by transfection with the *erbB2* oncogene. All of the above cell lines were obtained from Dr. Martha Stampfer (Lawrence Berkeley National Laboratory, Berkeley, CA) and cultured in MCDB 170 media supplemented as described previously (14, 20, 21). MCF-12A, a spontaneously immortalized cell line established from MCF-12 M mortal cells (19), was obtained from American Type Culture Collection (Rockville, MD) and cultured in

DMEM-Ham's F12 medium supplemented as described previously (22). All human breast cancer cell lines were obtained from American Type Culture Collection. The tumor-derived cell lines were cultured in DMEM-Ham's F12 medium supplemented with 10% fetal bovine serum. The phenotypic properties of all these cell lines have been described recently (14). Briefly, all the normal and immortalized cells exhibit anchorage-dependent growth. 185B5-*erbB2* and all the breast cancer cells exhibit anchorage-independent growth but whereas 185B5-*erbB2* can only form low frequency-high latency tumors, the breast cancer cells are tumorigenic and either lowly metastatic (SKBR3 and MCF7) or highly metastatic (MDA-MB-231 and MDA-MB-435) (14).

*Growth rate and cell size.* The growth rates of the cell lines used in this study were determined using the MTT assay, as previously described (14). Briefly, cells ($5 \times 10^3$) were plated in 24 well plates in 1 ml of media and incubated under normal culture conditions for 6 days. To estimate cell number, the cells were incubated with MTT (Sigma, St. Louis, MO) for 4 hr. MTT was then removed and the resulting formazan crystals were dissolved in 1 ml DMSO and 125 µl glycine buffer (pH 10.5) (14). The UV absorbance of the formazan solution was recorded at 553 nm ($\lambda$max). Four replicates were used to calculate the cell doubling time for each cell line. Since the cells had different morphologies and diameters, the cell size was determined for each cell line by trypsinizing the cells and counting the diameter of 20 random cells using an optical microscope.

*Measurement of intracellular lactate levels in HMECs.* To determine lactate levels in HMECs, cells growing in culture were fed with fresh media 24 hr before extraction and used at 70–80% confluency. Cells ($10^7$–$10^8$) were trypsinized, washed twice with normal saline, and homogenized with ice-cold 8% perchloric acid (PCA; 5 ml). The homogenates were centrifuged (15,000 rpm for 15 min at 4°C), and the supernatants were neutralized with 3 M $K_2CO_3$/1 M KOH buffer. The samples were again clarified by centrifugation, treated with~50 mg Chelex (Sigma Chemical Co., St. Louis, MO) to remove divalent ions, lyophilized, and resuspended in 0.5 ml of $D_2O$ for nuclear magnetic resonance (NMR) spectroscopy analysis. Trimethylsilylpropionate (TSP; 5 µl) was used as an internal standard. $^1$H NMR spectra of extracts were acquired on an 11.7 T Bruker NMR spectrometer with a 5-mm probe. Fully relaxed spectra (without saturation effects) were obtained using the following acquisition parameters: 30° flip angle, 6000 Hz sweep width, 4.7 s repetition time, 32 K block size, and 512 scans. The data were analyzed using an in-house software, Soft Fourier Transform (P. Barker, The Johns Hopkins University). To determine the concentration of lactate, peak amplitudes for lactate (doublet) were compared with that of the

internal standard TSP according to the equation

$$[\text{lactate}] = 3 \times \text{Amplitude}_{(\text{lactate})} \times [\text{TSP}] / \text{Amplitude}_{(\text{TSP})} \times \text{cell number} \times \text{cell volume},$$

where, [lactate] is the molar concentration of lactate, [TSP] is the molar concentration of TSP used, and cell volume was calculated as previously described (14). For this equation to be valid, it is necessary that spectra are fully relaxed, as was the case here, or to correct for saturation.

*Measurement of lactate dehydrogenase activity.* To determine LDH activity in HMECs, cells growing in culture were fed with fresh media 3 hr before lysis and used at 70–80% confluency. Cells were washed with phosphate buffered saline, lysed (lysis buffer: 100 mM Tris (pH 8.0), 150 mM NaCl, 1 mM EDTA, 1% Tween-20) and centrifuged for 5 min (14,000 rpm). The supernatants were kept on ice and used immediately for the LDH enzyme assay (Sigma diagnostic kit DG 1340-K, Sigma), which measures the change in absorbance at 340 nm due to formation of nicotinamide adenine dinucleotide (NAD) from a solution of NADH and pyruvate. Two LDH measurements were performed for each supernatant. Three independent samples were prepared for each cell line. Data were expressed as units of LDH activity per mg of protein. Protein content of supernatants was determined using the Bio-Rad DC assay (Bio-Rad, Melville, NY), which is based on the method of Lowry (23).

*Statistical analysis.* Statistical analysis of the data was performed using StatView II version 1.04 (Abacus Concepts Inc.,. Berkeley, CA). The Mann–Whitney U-test was used to evaluate the statistical significance of unpaired data sets. $P$ values of $\leq 0.05$ (95% confidence) were considered significant.

## RESULTS AND DISCUSSION

The lactate doublet was detected by $^1$H NMR of perchloric acid extracts of cells at a resonance frequency of 1.3 ppm downfield of TSP. Figure 1 represents signal to noise comparable high-resolution NMR spectra of extracts obtained from immortalized MCF12A and malignant MDA-MB-231 cells. A large difference in lactate levels is apparent between these cell lines. All epithelial cell lines were characterized by this method. Other resonances (not shown here) including creatine, phosphocreatine, choline, phosphocholine, glycerophosphocholine, taurine, alanine were also identified. A summary of lactate levels calculated for each cell line and normalized to cell number and cell size is shown in Fig. 2. The data represent three to five independent extracts per cell line. No gradual increase in lactate levels

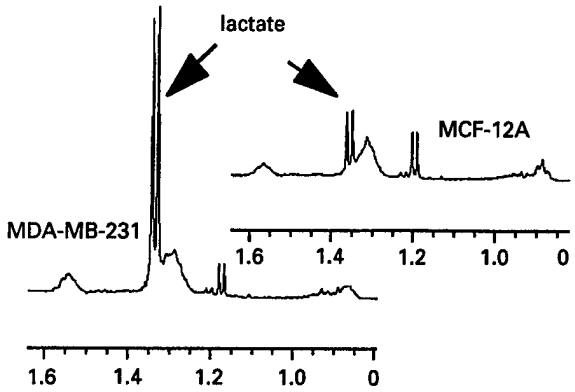


FIG. 1. Typical high-resolution $^1$H NMR spectra obtained from perchloric acid extracts of MCF12A and metastatic MDA-MB-231 HMEC's grown in culture. The spectra are expanded to show the lactate region and have been displayed with comparable signal to noise levels.

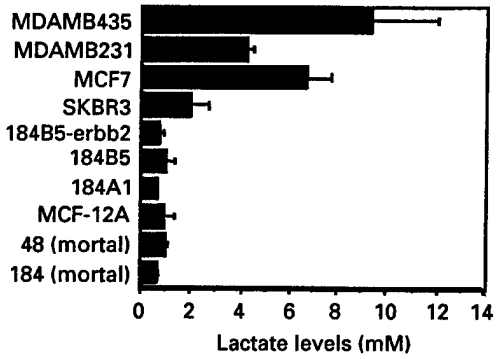


FIG. 2. Lactate levels in a panel of cell lines representing various stages of breast carcinogenesis. There was a statistically significant difference in lactate levels between the tumor-derived cells (SKBR3, MCF-7, MDA-MB-231 and MDA-MB-435) and the normal/immortalized cells (184-mortal, 48-mortal, 184A1, 184B5, and 184B5-erbB2) and between MDA-MB-435 cells and all other cells. Bars represent 1 SEM ($n=3$–5).

with increase in malignant transformation was observed in our model system. All tumor-derived cells, however, showed significantly higher levels of lactate compared to the normal, immortalized and *erbB2* oncogene transformed cells ($p \leq 0.05$). The most metastatic of the cell lines, MDA-MB-435, showed the highest lactate level. As in our previous study (14), there was no correlation between lactate levels and cell doubling time ($p \geq 0.05$) as shown in Fig. 3. Taken together, these data suggest that the high lactate phenotype presents late in carcinogenesis. It also shows that, as

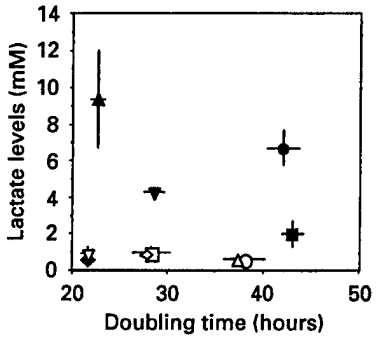


FIG. 3. The relationship between doubling time and lactate levels (mM). Doubling times were measured by the MTT assay (see Materials and Methods) and increased in the order MCF-12A > 48(mortal) > MDA-MB-435 > 184B5-erbB2 > 184B5 > MDA-MB-231 > 184 (mortal) > 184A1 > MCF-7 > SKBR3. MDA-MB-435 (▲), MDA-MB-231 (▼), MCF-7 (●), SKBR3 (■) MCF-12A (◆), 184 (mortal) (△), 48 (mortal) (▽), 184A1 (○), 184B5 (□), and 184B5-*erbB2* (◇).

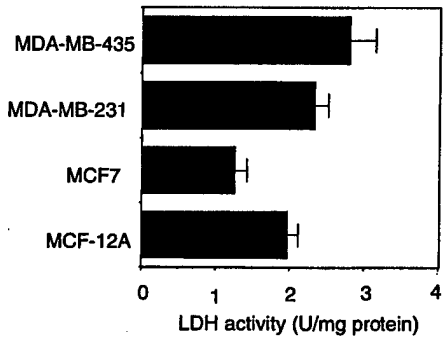


FIG. 4. LDH activities in selected HMEC's determined as described in the Material and Methods section. One unit of LDH activity is defined as the amount of enzyme which catalyzes the formation of 1 μmol/l of NAD per minute under the conditions of the assay. Bars represent 1 SEM ($n=3$).

with regenerating liver (3), growth can occur without increased glycolysis. Regarding other energy metabolites (creatine and phosphocreatine), only MDA-MB-435 showed significant levels of creatine and phosphocreatine in the cell lines.

LDH is the final enzyme involved in the conversion of glucose to lactate. Due to its association with neoplasia (6, 7) we investigated whether the differences in lactate levels could be due to upregulation of LDH enzyme activity. LDH activities for selected cells were found to increase in the order MCF7 < MCF12A < MDA-MB-231 < MDA-MB-435 (Fig. 4). Again, the

most metastatic of the cell lines, MDA-MB-435, showed the highest LDH activity. However, there was no overall association between lactate levels and LDH activities in the four cell lines studied, and the spontaneously immortalized (hyperplastic) cell line MCF12A showed relatively higher LDH activity compared to MCF7 cells.

We have characterized normal, immortalized, *erbB2* oncogene transformed and tumor-derived mammary epithelial cells to understand the relationship between malignant transformation and lactate levels. Our studies indicate that, unlike choline metabolite levels, which progressively increased with malignant transformation (14), lactate levels remained low in all normal, immortalized and *erbB2* oncogene transformed cells. Consistent with published data for human breast tumors versus uninvolved breast tissue (6), lactate levels in all the tumor-derived cell lines were significantly higher. Our data, therefore, suggests that the phenotype of increased lactate levels characteristic of human tumors probably occurs late in carcinogenesis. The exact mechanisms underlying this phenotype are unknown. The increased lactate levels could be due to a combination of factors including amplification of regulatory genes such as *c-myc* (8, 24), which occurs in 23–56% of human breast cancers (25–30) and in tumor-derived cell lines including SKBR3, MCF7 and MDA cells (31, 32). This alteration could lead to increased expression of glycolytic enzymes such as LDH and hence of lactate levels. However, in four of the cell lines, lactate levels did not correlate with LDH activity. A possible reason for this observation is that LDH is in great excess (2). A study of the activities of other enzymes involved in glycolysis will shed further light on the underlying mechanisms.

The late appearance of the increased lactate phenotype suggests that it is unlikely that the regulation of lactate levels will involve a single gene product. In this regard, our initial studies with wild-type and *c-myc*-transformed A1N4 cells ($2.54 \pm 0.05$ versus $2.33 \pm 0.13$ mM, respectively) did not show any differences in intracellular lactate levels (E. O. Aboagye, H. Shim and Z. M. Bhujwalla, unpublished). In their study, Thompson and coworkers (17) showed that *c-myc* alone did not increase the invasive phenotype of A1N4 cells, indicating the importance of previous immortalization processes on the characteristics of cell lines. The most metastatic line, MDA-MB-435, exhibited the highest lactate concentration and LDH activity. Recently, it was shown that patients with cervical cancers containing high lactate had a high risk of metastases (33) and our data support the observation that lactate may play a role in the metastatic cascade.

In summary, we have demonstrated in our model system that the phenotype of increased lactate levels occurs late in carcinogenesis and is independent of cell doubling time. These studies are important to understanding the mechanisms involved in lactate regulation in normal and

cancer cells, and in the use of lactate as a marker of malignancy or of response to therapy in patients.


## SUMMARY

Lactate is produced during glycolysis from pyruvate by the action of lactate dehydrogenase (LDH; EC 1. 1.1.27). To understand the relationship between the multi-step process of carcinogenesis of mammary epithelial cells and regulation of lactate levels, we studied a series of mammary epithelial cells representing various stages of transformation including normal (senescent/mortal) cells, spontaneously/benzo(a)pyrene immortalized cells, *erbB2* oncogene transformed immortalized cells, and tumor-derived cells. 1. In our model system, intracellular lactate levels were low in normal cells and remained low after immortalization. Further transformation of benzo(a)-pyrene immortalized cells by the *erbB2* oncogene did not increase lactate levels. In contrast, all tumor-derived cells showed significantly higher lactate levels compared to the normal, immortalized and oncogene transformed cells ($p \leq 0.05$). These studies suggest that the phenotype of increased lactate levels occurs late in carcinogenesis and supports our central hypothesis that multiple genes involved in malignant progression regulate the high lactate phenotype. 2. There was no correlation between intracellular lactate levels and cell doubling time. This suggests that increased glycolysis is not a prerequisite for growth. 3. Although the most metastatic of the cell lines had the highest lactate level and LDH activity, there was no overall association between lactate levels and LDH activity. This suggests that LDH is in great excess and may not be rate limiting. These studies are important in the use of lactate as a marker of malignancy or of response to therapy in patients.



## ACKNOWLEDGEMENTS

This work was supported by USAMRMC Grant DAMD-17-96-1-6131. We are grateful to Dr. Martha Stampfer of Berkeley National Laboratory (Berkeley, CA) for kindly donating the HMEC's used in this study and for useful suggestions. We thank Dr. V.P. Chacko, Dr. H. Shim and Mr. Gary Cromwell for expert assistance during the experiments.


## REFERENCES


1. O. WARBURG, *The Metabolism of Tumors*, Constable and Co., London, UK, 1930.
2. G. WEBER, Carbohydrate metabolism in cancer cells and the molecular correlation concept, *Naturwissenschaften* **9,** 418–429 (1968).
3. G. WEBER, Enzymology of cancer cells, *N. Engl. J. Med.* **296,** 486–493 (1977).
4. R. L. VEECH, The metabolism of lactate, *NMR Biomed.* **4,** 53–58 (1991).
5. M. TERPSTRA, R. GRUETTER, W. B. HIGH, M. MESCHER, L. DeLaBARRE, H. MERKLE and M. GARWOOD, Lactate turnover in rat glioma measured *in vivo* by nuclear magnetic resonance spectroscopy, *Cancer Res.* **58,** 5083–5088 (1998).

6. I. S. GRIBBESTAD, H. E. FJOSNE, O. A. HAUGEN, G. NILSEN, J. KRANE and S. B. PETERSEN, *In vitro* proton NMR spectroscopy of extracts from human breast tumors and non-involved breast tissue, *Anticancer Res.* **13,** 1973–1980 (1993).
7. N. YAMAMOTO, T. WATANABE, N. KATSUMATA, Y. OMURO, M. ANDO, H. FUKUDA, Y. TAKUE, M. NARABAYASHI, I. ADACHI and S. TAKASHIMA, Construction and validation of a practical prognostic index for patients with metastatic breast cancer, *J. Clin. Oncol.* **16,** 2401–2408 (1998).
8. H. SHIM, C. DOLDE, B. C. LEWIS, C. S. WU, G. DANG, R. A. JUNGMAN, R. DALLA-FAVERA and C. V. DANG, c-Myc transactivation of LDH-A: implications for tumor metabolism and growth, *Proc. Natl. Acad. Sci. USA* **94,** 6658–6663 (1997).
9. C. V. DANG and G. L. SEMENZA, Oncogenic alterations of metabolism, *Trends Biochem. Sci.* **24,** 68–72 (1999).
10. M. R. STAMPFER, A. BODNAR, J. GARBE, M. WONG, A. PAN, B. VILLEPONTEAU and P. YASWEN, Gradual phenotypic conversion associated with immortalization of cultured human mammary epithelial cells, *Mol. Biol. Cell* **8,** 2391–2405 (1997).
11. Z. M. BHUJWALLA and J. D. GLICKSON, Detection of tumor response to radiation therapy by *in vivo* proton MR spectroscopy, *Int. J. Radiat. Oncol. Biol. Phys.* **36,** 635–639 (1996).
12. E. O. ABOAGYE, Z. M. BHUJWALLA, D. C. SHUNGU and J. D. GLICKSON, Detection of tumor response to chemotherapy by $^{1}H$ nuclear magnetic resonance spectroscopy: effect of 5-fluorouracil on lactate levels in radiation-induced fibrosarcoma 1 tumors, *Cancer Res.* **58,** 1063–1067 (1998).
13. E. O. ABOAGYE, Z. M. BHUJWALLA, Q. HE and J. D. GLICKSON, Evaluation of lactate as a $^{1}H$ nuclear magnetic resonance spectroscopy index for noninvasive prediction and early detection of tumor response to radiation therapy in EMT6 tumors, *Radiat. Res.* **150,** 38–42 (1998).
14. E. O. ABOAGYE and Z. M. BHUJWALLA, Malignant transformation alters membrane phospholipid metabolism of human mammary epithelial cells, *Cancer Res.* **59,** 80–84 (1999).
15. M. R. STAMPFER and J. C. BARTLEY, Induction of transformation in continuous cell lines from normal human mammary epithelial cells, *Proc. Natl. Acad. Sci. USA* **8,** 2394–2398 (1985).
16. J. H. PIERCE, P. ARNSTEIN, E. DIMARCO, J. ARTRIP, M. H. KRAUS, F. LONARDO, P. DIFIORE and S. A. AARONSON, Oncogenic potential of erbB-2 in human mammary epithelial cells, *Oncogene* **6,** 1189–1194 (1991).
17. E. W. THOMPSON, J. TORRI, M. SABOL, C. L. SOMMERS, S. BYERS, E. M. VALVERIUS, G. R. MARTIN, M. E. LIPPMAN, M. R. STAMPFER and R. B. DICKSON, Oncogene-induced basement membrane invasiveness in human mammary epithelial cells, *Clin. Exp. Metastasis* **12,** 181–194 (1994).
18. E. VALVERIUS, S. E. BATES, M. STAMPFER, R. CLARK, F. McCORMICK, D. S. SALOMON, M. E. LIPPMAN and R. B. DICKSON, Transforming growth factor alpha and its receptor in human mammary epithelial cells: modulation of epidermal growth factor receptor function with oncogenic transformation, *Mol. Endocr.* **3,** 203–214 (1989).
19. L. M. SMITH, M. J. BIRRER, M. R. STAMPFER and P. H. BROWN, Breast cancer cells have lower activating protein 1 transcription factor activity than normal mammary epithelial cells, *Cancer Res.* **57,** 3046–3054 (1997).
20. M. R. STAMPFER, Isolation and growth of human mammary epithelial cells, *J. Tissue Culture Meth.* **9,** 107–116 (1985).
21. M. R. STAMPFER and P. YASWEN, Culture systems for study of human mammary epithelial cell proliferation, differentiation and transformation, *Cancer Surv.* **18,** 7–34 (1994).
22. T. M. PAINE, H. D. SOULE, R. J. PAULEY and P. J. DAWSON, Characterization of epithelial phenotypes in mortal and immortal human breast cells, *Int. J. Cancer* **50,** 463–473 (1992).
23. O. N. LOWRY, N. J. ROSEBROUGH, A. L. FARR and R. J. RANDALL, Protein measurement with the folin phenol reagent, *J. Biol. Chem.* **193,** 265–275 (1951).
24. C. V. DANG and G. SEMENZA, Oncogenic alterations of metabolism, *Trends Biochem. Sci.* **24,** 68–72 (1999).

25. M. BONILLA, M. RAMIREZ, J. LOPEZ-CUETO and P. GARIGLIO, *In vivo* amplification and rearrangement of c-myc oncogene in human breast tumors, *J. Natl. Cancer Inst.* **80,** 665–671 (1988).
26. Z. P. PAVELIC, L. PAVELIC, E. E. LOWER, M. GAPANY, S. GAPANY, E. A. BARKER and H. D. PREISLER, c-myc, c-erbB-2, and ki-67 expression in normal breast tissue and in invasive and noninvasive breast carcinoma, *Cancer Res.* **52,** 2597–2602 (1992).
27. C. ESCOT, C. THEILLET, R. LIDEREAU, F. SPYRATOS, M. H. CHAMPEME, J. GEST and R. CALLAHAN, Genetic alteration of the c-myc protoncogene (MYC) in human primary breast carcinomas, *Proc. Natl. Acad. Sci. USA* **83,** 4834–4838 (1986).
28. E. M. BERNS, J. G. KLIJN, W. L. van PUTTEN, I. L. van STAVEREN, H. PORTENGEN and J. A. FOEKERNS, c-myc amplification is a better prognostic factor than HER2/neu amplification in primary breast cancer, *Cancer Res.* **52,** 1107–1113 (1992).
29. M. GUERIN, M. BARROIS, M. J. TERRIER, M. SPIELMAN and G. RIOU, Overexpression of either c-myc or c-erbB-2/neu proto-oncogenes in human breast carcinomas: correlation with poor prognosis, *Oncogene Res.* **3,** 21–31 (1988).
30. H. KREIPE, H. FEIST, L. FISHER, J. FELGNER, K. HEIDORN, L. METTLER and R. PARWARESCH, Amplification of c-myc gene and amplification in human tumor cell lines, *Cancer Res.* **53,** 1956–1961 (1993).
31. S. FEO, C. LIEGRO, T. JONES, M. READ and M. FRIED, The DNA region around the c-myc gene and amplification in human tumor cell lines, *Oncogene* **9,** 955–961 (1994).
32. T. L. MILLER, Y. JIN, J. M. SUN, A. S. COUTTS, L. C. MURPHY and J. R. DAVIE, Analysis of human breast cancer nuclear proteins binding to the promoter elements for the c-myc gene, *J. Cell Biochem.* **60,** 560–571 (1996).
33. G. SCHWICKERT, S. WALENTA, K. SUNDFOR, E. K. ROFSTAD and W. MUELLER-KLIESER, Correlation of high lactate levels in human cervical cancer with incidence of metastasis, *Cancer Res.* **55,** 4757–4759 (1995).

REVIEW ARTICLE

Neoplasia • Vol. 2, Nos. 1–2, January-April 2000, pp. 139–151 139

www.nature.com/neo

# Applications of Magnetic Resonance in Model Systems: Tumor Biology and Physiology[1]

*Robert J. Gillies*, Zaver M. Bhujwalla†, Jeffrey Evelhoch‡, Michael Garwood§, Michal Neeman¶, Simon P. Robinson#, Christopher H. Sotak** and Boudewijn Van Der Sanden††*

*Department of Biochemistry, Arizona Cancer Center, University of Arizona, Tucson, AZ; †Oncology Section, Division of MR Research, Department of Radiology, The Johns Hopkins University School of Medicine, Baltimore, MD; ‡MR Center, Harper Hospital, Wayne St. Univ., Detroit, MI; §Center for Magnetic Resonance Research, University of Minnesota School of Medicine, Minneapolis, MN; ¶Department of Biological Regulation, The Weizmann Institute of Science, Rehovot 76100, Israel; #CRC Biomedical Magnetic Resonance Research Group, Department of Biochemistry and Immunology, St. George's Hospital Medical School, London, UK SW17 ORE ; **Department of Biomedical Engineering, Worcester Polytechnic Institute, Worcester, MA and Department of Radiology, University of Massachusetts Medical School, Worcester, MA and ††Department of Radiology, Academic Hospital, Nijmegen, Netherlands

## Abstract

**A solid tumor presents a unique challenge as a system in which the dynamics of the relationship between vascularization, the physiological environment and metabolism are continually changing with growth and following treatment. Magnetic resonance imaging (MRI) and magnetic resonance spectroscopy (MRS) studies have demonstrated quantifiable linkages between the physiological environment, angiogenesis, vascularization and metabolism of tumors. The dynamics between these parameters continually change with tumor aggressiveness, tumor growth and during therapy and each of these can be monitored longitudinally, quantitatively and non-invasively with MRI and MRS. An important aspect of MRI and MRS studies is that techniques and findings are easily translated between systems. Hence, pre-clinical studies using cultured cells or experimental animals have a high connectivity to potential clinical utility. In the following review, leaders in the field of MR studies of basic tumor physiology using pre-clinical models have contributed individual sections according to their expertise and outlook. The following review is a cogent and timely overview of the current capabilities and state-of-the-art of MRI and MRS as applied to experimental cancers. A companion review deals with the application of MR methods to anticancer therapy.** *Neoplasia* (2000) **2,** 139–151.

**Keywords:** Magnetic Resonance Imaging (MRI), Magnetic Resonance Spectroscopy (MRS), Tumor Perfusion, Tumor Oxygenation, Tumor pH, Tumor Metabolism.

## Introduction

A clear finding from magnetic resonance (MR) investigations into clinical and experimental tumors is that they are internally heterogeneous in terms of their perfusion, oxygenation and metabolism. This phenotype has a direct impact on the ability to cure cancers, since therapies that work in one volume of the tumor may not be effective in other volumes. The companion review (Evelhoch *et al.*, this volume) describes the use of MR to assess and improve therapeutic efficacy. The current review describes research aimed at defining the causes of this heterogeneous physiology. No comparisons are made to other methods (e.g., microelectrodes for pH or oxygen, Doppler ultrasound or nuclear medicine for perfusion). MR is able to observe many diverse aspects of tumor physiology, often simultaneously or in the same exam. Because of this, it is a peerless technology.

## Perfusion and Angiogenesis

### *Insights into Tumor Perfusion from MR Studies*

Of the myriad facets that cancer displays, its ability to establish a vascular network is one of the most dangerous. This vascular network provides cancer cells with nutrients and oxygen to grow, as well as avenues to escape from. Paradoxically, it is also the primary means through which anti-neoplastic agents can be delivered to treat solid tumors. Interest in tumor vasculature has existed since the 1920s and before [1], and it was recognized as early as 1945 that malignant cells provoked a continuous vascular proliferation [2]. The earliest indirect evidence of the existence of

Address all correspondence to: Robert J. Gillies, Arizona Cancer Center, Tucson, AZ 85724-5024. E-mail: gillies@u.arizona.edu

[1]This study was supported by PHS grants CA77575 (R.J.G.), CA83041 (R.J.G.), CA73850 (Z.B.), CA82337 (Z.B.), CA75334 (M.N.), CA64338 (M.G.) and RR08079 (M.G.); grants from the Flinn (R.J.G.), Komen (Z.B.), Whitaker (C.H.S.) and Keck (M.G.) Foundations; grant DAMD17-96-1-6131 from the US Army MRMC (Z.B.); grants from the Dutch Cancer Society (B.v.S.); and grant [SP1971/0703] from the Cancer Research Campaign, UK (S.R.).

Received 16 September 1999; Accepted 13 October 1999.

radioresistant hypoxic cells [3] in solid tumors came from observations made by Thomlinson and Gray on human specimens of bronchogenic carcinoma in 1955 [4]. Necrosis was found to occur at a distance of 160 $\mu$m or greater from the nearest vessel in the histologic sections. This distance corresponded closely to the diffusion distance calculated by them where the concentration of oxygen would approach zero.

Numerous studies, which now span almost a century (see Ref. [5] for review), have identified several features which are characteristic of tumor vasculature. Amongst these are i) spatial heterogeneity and chaotic structures, ii) arteriovenous shunts, iii) acutely collapsed vessels and transiently collapsing vessels, iv) poorly differentiated, fragile and leaky vessels lacking in smooth muscle cell lining, and v) vasculature which is frequently unable to match the rapid growth of cancer cells, resulting in areas of hypoxia and necrosis. Interest in tumor vascularization and angiogenesis has increased recently due to two findings. One is that high vascular density in histologic specimens may be predictive of the disposition of the tumor to metastasize [6,7]. The second finding is that repeated treatment cycles with the angiogenesis inhibitor, endostatin, induced tumor dormancy in experimental tumor models without inducing tumor drug resistance [8].

Neovascularization is essential for tumor growth and progression [9]. Tumor cells induce neovascularization through the release of angiogenesis factors and several factors have now been identified as angiogenic promoters and angiogenic inhibitors [9,10]. An angiogenic factor which appears to be most responsive to the abnormal physiological environments of hypoxia, extracellular acidosis and substrate deprivation occurring in solid tumors [11] is vascular endothelial growth factor (VEGF). VEGF induces angiogenesis [12–14] and is also a potent vascular permeability factor [15]. Angiogenesis continues to occur through the lifetime of the tumor since new vasculature has to be continually generated with tumor growth. Three quantities, tumor blood flow, tumor vascular volume and vascular permeability, have mainly been used to characterize tumor vasculature. Relative to the time frame of non-MR methods of studying vasculature, MR is very recent. However, both magnetic resonance imaging (MRI) and magnetic resonance spectroscopy (MRS) have provided unique and novel insights into tumor vasculature and the interaction between the vasculature and physiology and metabolism.

### *MRI of Tumor Vasculature*

Vascularization can be evaluated with MRI using intrinsic endogenous contrast [16] or with exogenous paramagnetic contrast agents. The theoretical basis and applications of these methods to studying solid tumor vasculature has been recently reviewed [17]. Gadolinium chelates are the contrast agents most frequently used for MRI. When the ion is placed in a magnetic field, the seven unpaired electrons of gadolinium produce a large magnetic moment that results in paramagnetic properties, creating contrast in an MR image. Paramagnetic agents shorten the $T_1$ (spin-lattice relaxation time), and tissues that take up a paramagnetic agent are brightened (positive enhancement). Several Gd complexes are under development or in use. Low-molecular weight GdDTPA (Gadolinium DiethyleneTriaminePentaAcetate) compounds (0.57 kDa) are used clinically for contrast enhancement of various lesions, including malignant tumors. Macromolecular contrast agents such as Gadomer-17 or albumin-GdDTPA, remain in the intravascular space with a half life of several hours because of their large molecular weights (approximately 35 or 65 kDa, respectively). Analysis of relaxivity changes induced by an intravascular agent can be used to determine blood or vascular volume and vascular permeability [18,19]. Recently, receptor-targeted contrast agents have been designed, where the contrast is derived from the density of receptor expression [20]. Of the three parameters mainly used to characterize tumor vasculature, currently, only vascular volume and vascular permeability can be quantified with contrast-enhanced proton imaging. However, quantitative blood flow measurements have been obtained using deuterium MRI with $D_2O$ as the blood flow tracer [21].

### *Assessing Features of Tumor Perfusion by Dynamic $^1$H-MRI Studies of GdDTPA Uptake*

In the context of tumor therapy, it is important to know how efficiently blood is providing oxygen, nutrients and drugs to tumor tissue and how effective it is in removing waste products from that tissue. In most tumors, only 20% to 80% of the microvessels are perfused at a given time [22], which results in a considerable spatial and temporal heterogeneity of the microcirculation. Therefore, techniques that reveal the spatial and temporal heterogeneity of the tumor microcirculation will help in the development of new treatment strategies and may predict treatment outcome.

Fast dynamic $^1$H-MRI studies of GdDTPA uptake can measure features of the *perfused* microvascular architecture with a high spatial and temporal resolution [23–25]. The regional uptake rate of this tracer into the extravascular volume of tumor tissue is related to physiological parameters that determine the supply of oxygen, nutrients and drugs, such as tumor blood perfusion (TBP) and diffusive transport across the vascular endothelium [5,26]. Different pharmacokinetic models have been developed to relate GdDTPA-uptake rates to these physiological parameters [27–29]. The most important are the single-capillary model proposed by Kety [27] or Larsson *et al.* [28] and the multi-compartment model developed by Tofts and Kermode [29]. Both models were compared in 1992 and possible differences were explained [30]. In these models, tumor tissue is considered as a volume with a vascular and extravascular compartment. The uptake of a tracer in the extravascular compartment is governed by a rate constant $k$ ($s^{-1}$) and by tracer concentration differences between both compartments. The single-capillary model is more universal than the multi-compartment model, because the tracer-uptake rate constant $k$ ($s^{-1}$) is related to both TBP (ml $s^{-1}$) and diffusive transport across the vascular endothe-

lium (ml $s^{-1}$), whereas in the multi-compartment model, $k$ is only determined by diffusive transport across the vascular endothelium [29,30]. This transport term is dominated by the permeability ($P$) of the vascular endothelium (cm $s^{-1}$) and the surface-area ($S$) of the perfused microvessels ($cm^2$). Both parameters are grouped in the so-called *PS*-product, because they are difficult to measure separately. Finally, in both models, the uptake rate constant has an inverse relationship with the distribution volume ($V_d$) (ml) of the tracer, which is the extracellular space in the case of GdDTPA.

The choice of the pharmacokinetic model depends on the physicochemical and pharmacological properties of the tracer. For instance, diffusion-limited tracer uptake across the vascular endothelium may be favored when tracers with a molecular weight larger than 20 kDa are chosen [31] (see also Tumor Perfusion Measured with High-Molecular Weight Tracers section). In the case of small tracers, such as GdDTPA, it is more difficult to correlate tracer-uptake rates directly to TBP and/or diffusive transport across the vascular endothelium, since both may influence the tracer-uptake rate simultaneously. However, detailed information on morphometric parameters of the *perfused* neovasculature of a tumor may help to solve this problem.

In pre-clinical studies on 9L-glioma growing in rat brain, the perfused vascular surface-area ($S$) was determined immunohistochemically and co-registered with images of fast dynamic GdDTPA uptake [31]. Spatial matching of $S$ with GdDTPA-uptake rates revealed a linear relationship (see Figure 1*A*). The linear relationship suggests that GdDTPA-uptake rates ($k$) are dominated by $S$ and hence, are not significantly affected by variations in TBP or vascular permeability ($P$). The molecular weight of GdDTPA is probably not large enough to discriminate between more or less leaky microvessels, because all microvessels were highly permeable to GdDTPA. Furthermore, it would be of interest to know which range of TBP values could affect the relationship between $k$ and $S$. For that purpose, relationships between $k$-values, *PS*-product and TBP were simulated using the single-capillary model. In these simulations, the TBP was varied between 0 and 4 times the maximum *PS*-product found in the study on 9L-glioma growing in rat brain [31]. In Figure 1*B*, it is shown that the relationship between $k$-values and the *PS*-product becomes linear only when the TBP is larger than the *PS*-product. Thus, the linear relationship between $k$-values and the perfused vascular surface area in Figure 1*A* suggest that TBP is larger than the *PS*-product in the different voxels. Hence, GdDTPA-uptake rates are *diffusion-limited*. If the TBP was less than the *PS*-product, the relationship between $k$ and *PS*-product would be exponential, showing that GdDTPA-uptake rates were *perfusion-limited*. When GdDTPA-uptake rates can be related to parameters of the functional neovasculature, they can be used more efficiently as a prognostic tool before or during the monitoring of a therapy. For instance, this may help to monitor non-invasively the effect of an anti-angiogenic therapy on tumor microvessels.

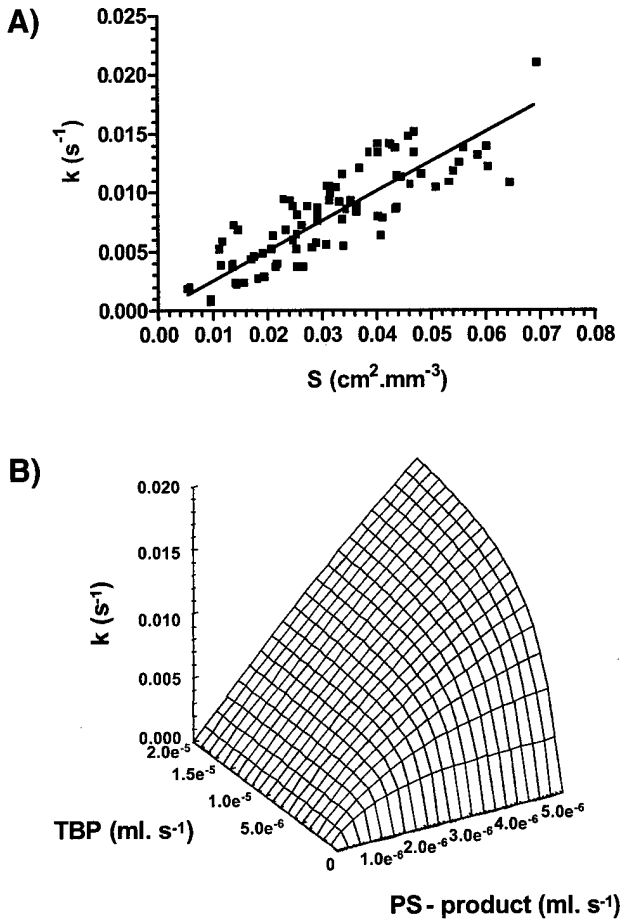


**Figure 1.** *(A) The correlation between GdDTPA-uptake rates (k) and the perfused vascular surface-areas (S) in voxels of 10 9L-gliomas. The solid line indicates the results of the least-squares linear regression analysis of the data: $k = 0.23 \pm 0.02$ SD×S, $R^2 = 0.72$ ($n = 86$). (B) Surface-plot of correlations between the PS-product (x-axis), TBP (y-axis) and GdDTPA-uptake rate constants (k) (z-axis) using the definition of the rate constant k as proposed by Kety [27] or Larsson et al. [28]. Note that the range of k-values is comparable to the range in (Figure 2A). These data are from work performed by B. van der Sanden with grateful acknowledgements to Dr. T.H. Rozijn, Dr. W.M.M.J. Bovee, P.F.J.W. Rijken, Prof. A.J. van der Kogel and Prof. A. Heerschap.*

*Tumor Perfusion Measured with High-Molecular Weight Tracers*

GdDTPA conjugated to high molecular weight tracers can be used to generate three-dimensional maps of vascular volume and permeability [32,33]. Multi-slice data obtained for a human breast cancer model (MDA-MB-435-1$\beta$) in a SCID mouse are presented in (Figure 2*a* – *f*). At the end of the imaging studies, the animals were sacrificed, 0.5 ml of blood withdrawn from the inferior vena cava, and tumors were marked for referencing to the MRI images, excised and fixed in 10% formalin for sectioning and staining.

In the MR images, the relaxation rate ($1/T_1$) was determined in each voxel as a function of time. The slopes of these relationships were used to compute (*PS*) maps (Figure 2*b*). The intercept of the line at zero time is used to compute vascular volume maps, shown in (Figure 2*c*) [34]. In this manner, vascular volumes are

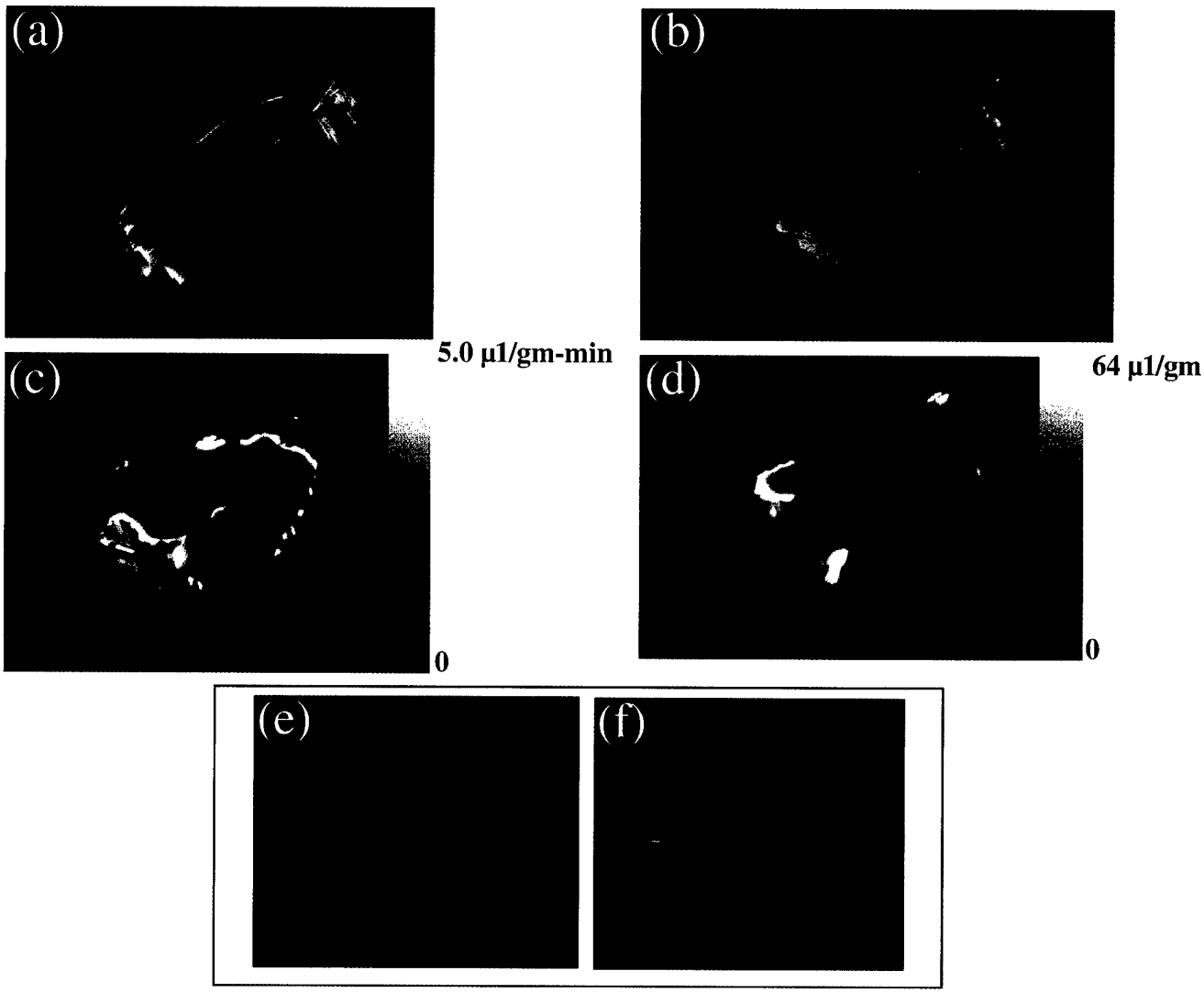


**Figure 2.** *Three-dimensional reconstructed maps obtained from a single MDA-MB-435-1β tumor. (a) Sections stained for VEGF expression using a rabbit polyclonal anti-VEGF antibody (Santa Cruz Biotechnology, Santa Cruz, CA). (b) Hematoxylin/eosin-stained histologic sections. (c) MRI map of vascular permeability. (d) MRI map of vascular volume. (e,f) Three-dimensional and triplanar views of a fused vascular image obtained by displaying vascular volume through a green channel and vascular permeability through a red channel. Multi-slice maps of relaxation rates ($T_1^{-1}$) were obtained by a saturation recovery method combined with fast $T_1$ SNAPSHOT-FLASH imaging (flip angle of 5°, echo time of 2 msec). Images of eight slices (slice thickness of 1 mm) acquired with an in-plane spatial resolution of 250 µm (64×64 matrix, 16 mm field of view, NS = 16) were obtained for three relaxation delays (100 msec, 500 msec, and 1 second) for each of the slices. Thus, 64×64×8 $T_1$ maps were acquired within 7 minutes with an $M_o$ map with a recovery delay of 7 seconds acquired once at the beginning of the experiment. Images were obtained before i.v. administration of 0.2 ml of 60 mg/ml albumin-GdDTPA in saline (dose of 500 mg/kg) and repeated every 8 minutes, starting 10 minutes after the injection, up to 32 minutes. Relaxation maps are reconstructed from data sets for three different relaxation times and the $M_o$ data set on a pixel-by-pixel basis. These data are from work performed by D. Artemov, M. Solaiyappan and Z. M. Bhujwalla.*

corrected for vessel permeability. Adjacent 5-µm-thick histologic sections obtained at 500-µm intervals through the tumor were stained with hematoxylin/eosin or for distribution of VEGF. Sections were digitized with a Sanyo CCD camera attached to an optical microscope. Three-dimensional reconstructions of both MRI and histologic sections (Figure 2*a* and *b*), were performed using the Clinical Microscope Visualization software running on Silicon Graphics Inc., Octane Workstation. Image cross-registration was performed interactively. Also shown in Figure 2*e* and *f* are the fusion of vascular volume and vascular permeability displayed as two independent colors, green and red. The absence of yellow in most of the image demonstrates visually that there is very little overlap between regions of high vascular volume and regions of high permeability. This characteristic has been consistently observed. Regions of low vascular volume often contain necrotic foci and are also the most permeable [17]. These regions are also usually associated with higher expression of VEGF. These data support earlier MRI observations made by Furman-Haran *et al.* [35] that highly permeable vessels were detected near necrotic regions for MCF-7 tumors. Another possibility is that tumor vessels appear leaky in these regions (especially in the clinic) because they have been destroyed by an advancing invasive tumor mass.

Ethylnitrosourea induces breast tumors fibroadenomas (FA), as well as low and high grade infiltrating ductal carcinomas (IDC) in the rat. Using this system, the pharmacokinetic characteristics of Gd-DTPA (<1 kD), Gadomer-17 (35 kD), and albumin-Gd-DTPA (70–90 kD) were evaluated by Dynamic Contrast Enhanced MRI in order to differentiate the different tumor types [18]. The benefits of using three different sized contrast agents is that a greater range in permeability values can be discriminated. The results indicated that vascular volume was a consistent determinant of tumor grade. Although high-grade IDC had the highest vascular permeability, this parameter was somewhat more variable in that FA had a higher vascular permeability than that of low-grade IDC. The statistical analyses showed that the clinically available small agents could be used to differentiate FA from the malignant tumors, but it could not differentiate between malignant tumors of low and high grades. GdDTPA was useful in discriminating FA from IDC but could not discriminate between low and high grade IDC. The intermediate sized agent, Gadomer-17, could differentiate between high-grade and low-grade IDC, but it could not discriminate low-grade IDC from the benign FA. The largest agent, albumin-Gd-DTPA, was capable of differentiating all three tumor grades, but the low signal to noise ratio (resulting in high variation) was a major technical concern.

*MRI Analysis of Tumor Angiogenesis*

MRI provides multiple approaches for detection of tumor angiogenesis, based on molecular, structural and physiological distinctions between normal and tumor vasculature. Tumor neovasculature is frequently highly permeable, resulting in rapid extravasation of exogenously administered contrast material into the extracellular space. Dynamic contrast enhancement and clearance curves can be used for analysis of vascular permeability, blood volume and the extracellular volume fraction (*vide supra*). Using low-molecular weight contrast material (e.g., GdDTPA), significant correlations can be found between the parameters derived from MRI and histologic analyses of microvessel densities, but not with VEGF expression [36]. With the exception of the brain, most normal capillaries are permeable to low-molecular weight compounds such as GdDTPA. However, capillary endothelial cells stimulated with the angiogenic growth factor VEGF showed enhanced extravasation of plasma proteins. MRI analysis of VEGF-induced permeability was demonstrated using albumin-GdDTPA [37]. Treatment with neutralizing anti-VEGF antibodies led to immediate and persistent inhibition of albumin-GdDTPA extravasation [37]. Permeability measured by albumin-GdDTPA correlated spatially with elevated expression of VEGF (*vide supra*).

Thus, MRI-detected hyperpermeability can be used in many cases for *in vivo* assessment of VEGF signaling. However, the large variance in vessel permeability found in normal tissues as well as in tumors, implies that hyperpermeability cannot be used as a reliable marker of neovasculature. Alternative approaches for specific evaluation of angiogenesis can be found in two recent studies, in which the MRI contrast was sensitized to molecular or structural markers of angiogenesis. In the first study, specific image enhancement of tumor neovasculature has been achieved in a model of squamous cell carcinoma in rabbit using paramagnetic polymerized liposomes conjugated with anti $\alpha_v\beta_3$ antibodies [20]. In the second study, tumor neovasculature was characterized by the increased capillary diameter. Two mechanisms of water relaxivity induced by intravascular contrast material, $\Delta R_2$ (i.e., $1/T_2$) and $\Delta R_2^*$ (i.e., $1/T_2^*$), exhibit different dependencies on the radius of the blood vessels. Thus, the ratio of relaxivities ($\Delta R_2^*/\Delta R_2$) can be used to derive maps of capillary diameter, showing excellent agreement with histology and sensitive detection of the tumor neovasculature in experimental C6 rat glioma tumors [38].

Changes in *blood volume* associated with angiogenesis can be measured using the intrinsic contrast of blood vessels arising from deoxyhemoglobin and detected by $T_2^*$-weighted gradient echo images [16,39]. This method has been applied to measure, for example, the kinetics of spheroid vascularization and growth for rapidly growing C6 glioma [39], the vascular instability during the dormant phase of implanted human epithelial ovarian carcinoma spheroids [40], wound-induced tumor growth [41] and the increased angiogenic activity of human epithelial ovarian carcinoma tumors in ovariectomized hyper-gonadotropic mice [42]. These studies demonstrate that the angiogenic potential of tumors is frequently dominated by local microenvironmental changes (such as hypoxia and injury) or by systemic perturbations (such as changes in the hormonal milieu), rather than by genetic selection for angiogenic phenotype. The primary signal for tumor angiogenesis in this system was attributed to stress-induced expression of VEGF as controlled by the hypoxia-inducible transcription factor, hif-1$\alpha$.

In summary, assessment of environmental, molecular, genetic and pharmacological perturbations of angiogenesis requires extensive *in vivo* analytical tools. MRI can be used to non-invasively access a wide range of parameters that reflect vascular expansion and regression. The ability of MRI to obtain three-dimensional information provides large freedom in the design of the biologic model. Moreover, almost any MRI method developed in experimental models is potentially transferable to the clinical assessment of tumor angiogenesis.

*MRI Tracking of Vascular Function and Maturation Using Carbogen*

Regions of active angiogenesis are often connected to regions of low blood oxygenation, due to hif-1$\alpha$-induced transcription of VEGF. These volumes show large signal enhancements during exposure to elevated oxygen [43]. This signal enhancement can be used for imaging vascular functionality without intravenous administration of contrast material [44]. Oxygen is usually provided as carbogen (95% $O_2$/5% $CO_2$). The $CO_2$ is thought to act on baroreceptors in mature vasculature and prevent hyperoxic

vasoconstriction. Maturation of vessels is a secondary process related to the recruitment of perivascular smooth muscle cells and pericytes allowing the vessels to respond to vasoactive agents. Using this approach, reduced vascular functionality was measured in hif-1α-deficient embryonic stem cell tumors [44]. MRI has been applied for detection of changes in blood flow in response to elevated $CO_2$, as a physiological measure of vascular maturation [45]. Since VEGF is an essential survival factor for immature neovasculature [46], its withdrawal should lead to collapse of immature, but not mature vasculature. This was tested in subcutaneous C6 tumors containing the VEGF gene under control of an inducible (tetracycline) promotor (pTET-VEGF), and revealed the ability of MRI to predict vascular susceptibility to VEGF withdrawal [45]. These results are shown in Figure 3. In these studies, inhalation was switched between 95% air/5% $CO_2$ and carbogen. Hence, $CO_2$ was held constant and the only variable was $O_2$.

## Tumor Oxygenation, pH and Metabolism

Tumor oxygenation and pH are important parameters of tumor physiology that are inextricably coupled. Both low pH and low $pO_2$ levels negatively impact therapy and induce maturation of more transformed phenotypes [47]. These are also coupled through metabolism such that volumes with low $pO_2$ are expected to be more glycolytic and hence, the most acidic.

### *$^{19}$F-NMR Techniques for the Study of Tumor Oxygenation and Response to Interventions*

Hypoxic cells in solid tumors are generally found in regions of poor tumor vascularization and are thought to be responsible for reducing the effectiveness of both chemo- and radiotherapy. Vascularization in neoplastic tissue can be quite heterogeneous, allowing cells to become necrotic, chronically hypoxic (diffusion limited) or acutely hypoxic (perfusion limited). Consequently, the ability to spatially resolve tumor oxygen tension in a timely fashion would allow rapid dynamic changes in local tumor oxygen values to be evaluated in response to therapeutic interventions. The ability to study and monitor tumor hypoxia would facilitate the most efficacious administration of current treatment strategies and should stimulate new developments in solid tumor therapy.

$^{19}$F-NMR spectroscopy and imaging of perfluorocarbon (PFC) emulsions has been used extensively to measure oxygen tension in biologic systems [48]. The favorable biocompatibility of PFCs allows intravenous injection of these compounds in large doses. Following PFC administration, the emulsion particles are cleared from the vasculature by the reticuloendothelial system (RES) of the liver and spleen as well as macrophages in abscesses and tumors. In tumors with "leaky" vasculature, PFC particles can pass through the fenestrations in the vascular wall and accumulate in the interstitial space [49]. Oxygen-sensitive $^{19}$F-NMR relies on the fact that the NMR spin-lattice relaxation rate, $R_1$ $(1/T_1)$, of the PFC is enhanced in direct proportion to the dissolved molecular oxygen concentration and thus allows oxygen measurements to be performed in the vicinity of the sequestered PFC. Consequently, PFC spin-lattice relaxation rates measured *in vivo* are a sensitive indicator of tumor oxygen tension and provide a powerful noninvasive method for monitoring tumor hypoxia before and during treatment.

In spite of their promise as *in vivo* oxygen probes, the molecular structure of many PFCs is not conducive to high-sensitivity $^{19}$F-MRI studies of tumor oxygenation. Short $T_2$ relaxation times, relatively long $T_1$ relaxation times, compensation for chemical shift artifacts and *J*-modulation effects can severely reduce the $^{19}$F-MRI signal intensity for many PFCs [50]. Most of these technical difficulties have been mitigated through the introduction of more NMR-compatible PFCs [50,51] and the use of time-efficient MRI-data acquisition methods [51,52]. In particular, $^{19}$F-echo-planar imaging (EPI) of perfluoro-15-crown-5-ether has proven to be a useful method for measuring tumor oxygenation in experimental tumor models [51].

$^{19}$F-NMR spectroscopy and imaging have been used extensively to monitor changes in tumor oxygenation as a function of a variety of therapeutic interventions in animal models. $^{19}$F spectroscopy measurements from RIF-1 tumors in C3H mice showed a statistically significant improvement in tumor $pO_2$ for a nicotinamide-treated group as compared with saline-treated controls [53]. As shown in Figure 4, $^{19}$F-IR-EPI of perfluoro-15-crown-5-ether can be used to map the spatial distribution of oxygen tension in RIF-1 tumors and statistically significant changes in tumor oxygenation have been measured when the breathing gas was changed from air to carbogen [51,54]. This same imaging methodology has also been used to monitor changes in tumor oxygenation following radiotherapy [55], nicotinamide administration [53,56] and chemotherapeutic treatment with 5-fluorouracil [57].

### *Carbogen-Induced Changes in Tumor Oxygenation and Blood Flow Monitored by Gradient-Recalled Echo (GRE) MRI*

Because the oxygenation status of cells in tumors can influence the response of those tumors to therapy [58], several approaches have focused on methods for modifying tumor oxygenation and blood flow. One such approach is breathing carbogen (95% $O_2$/5% $CO_2$), to increase the amount of dissolved oxygen in the plasma to provide more oxygen at the capillary level, and hence allow diffusion of oxygen into chronically hypoxic regions. Carbogen has been shown to enhance rodent tumor radiosensitivity [59] and, in combination with nicotinamide, is currently being re-evaluated in several European clinical trials [60,61].

A non-invasive technique to assess changes in oxygenation and perfusion, and their heterogeneous distribution within an individual tumor, would be of considerable prognostic and diagnostic clinical value. $^1$H-MRI methods

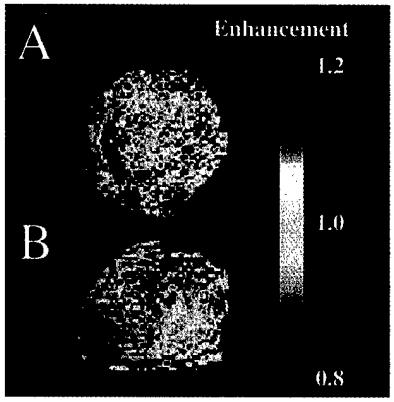


**Figure 3.** *Vascular collapse in response to VEGF withdrawal. Signal enhancement in response to hyperoxia was monitored in C6-pTET-VEGF tumors in nude mice, by switching the mice from inhalation of 95% air/5% $CO_2$ tp 95% $O_2$/5% $CO_2$ (carbogen). (A) In the absence of tetracycline, the tumors were hypervascular in accord with over-expression of VEGF. (B) Forty-eight hours after administration of tetracycline, suppressing VEGF over-expression, a significant drop in vascular function was observed (see also Refs. [20,21]). These data are from work performed by R. Abramovitch, H. Dafni, E. Smouha, L. Benjamin and M. Neeman.*

have high temporal and spatial resolution, which are sensitive to changes in deoxyhemoglobin content through the NMR relaxation time, $T_2$*. Deoxyhemoglobin is paramagnetic and creates susceptibility variations in the proximity of blood vessels, shortening the MR relaxation time, $T_2$*. GRE MRI sequences are sensitive to $T_2$* and hence reflect blood oxygenation levels. GRE MR images of tumors can thus be used to monitor changes in the tissue concentration of deoxyhemoglobin, whether due to fractional desaturation of oxygen from red blood cells, or blood flow modification causing changes in the absolute number of red blood cells. Deoxyhemoglobin thus acts as an endogenous contrast agent.

One of the first demonstrations of the potential of GRE MRI to the study of tumor physiology was by showing that carbogen breathing-induced large increases in image intensity of transplanted GH3 prolactinomas [62]. This increase in $T_2$* was consistent with a decrease in deoxyhemoglobin content within the tumor (Figure 5). Increases in both tumor blood oxygenation and blood flow have been discriminated within this response. Different GRE MRI responses to carbogen breathing have been observed in a number of other rodent tumor models (Ref. [62] and references therein), and the approach has also been successfully translated to the clinic, where differing GRE MRI responses of human tumors to carbogen breathing have been monitored [63]. This demonstrates that the effects are tumor-type-dependent and are presumably a consequence of different vascular architectures that exist within each tumor type.

The relationship of GRE MRI response and tumor $pO_2$, the critical parameter with respect to treatment outcome, has been investigated by invasive Eppendorf histography during carbogen breathing and showed a weak correlation in GH3 prolactinomas [62]. A stronger correlation of carbogen-induced increases in $T_2$* with tumor oxygen tension has

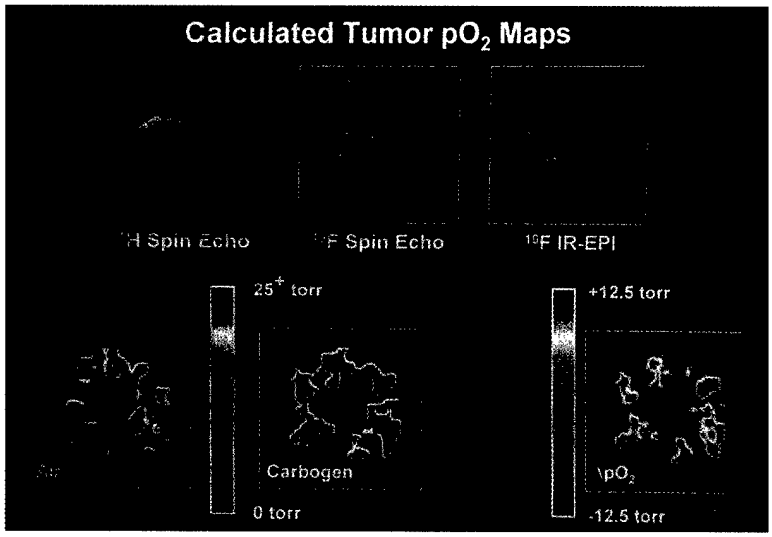


**Figure 4.** *Oxygen-tension mapping in a radiation-induced fibrosarcoma (RIF-1) tumor implanted on the lower back of a C3H mouse which received a 10 g/kg dose of perfluoro-15-crown-5-ether 4 days before imaging at 2.0 T. Upper Left: Coronal $^1$H spin-echo image of RIF-1 tumor, 256×256 pixel resolution, repetition time (TR) = 1 second, echo time (TE) = 25 msec, field of view (FOV) = 30 mm, slice thickness of 2 mm, 128 phase-encoding steps, number of averages (NEX) = 2. Upper Center: Coronal projection $^{19}$F spin-echo image of sequestered perfluoro-15-crown-5-ether in same tumor as in Upper Left, 128×128 pixel resolution, TR = 5 seconds, TE = 25 msec, FOV = 30 mm, 64 phase-encoding steps, NEX = 4, total image acquisition time = 21 minutes. Upper Right: Coronal projection $^{19}$F-inversion recovery-EPI of same tumor as in Upper Left, 64×64 pixel resolution, TR = 10 seconds, TE = 30 msec, inversion time (TI) = 80 msec, FOV = 30 mm, NEX = 8, total image acquisition time = 80 seconds. Lower Left: Calculated $pO_2$ map (from seven IR-EPIs, like that shown in Upper Right, with TI values of 0.08, 0.20, 0.50, 1.0, 2.0, 4.0, and 8.0 seconds, respectively) for animal breathing air. Color indicates $pO_2$ values from 0 to >25 Torr. Lower Center: Calculated $pO_2$ map as in Lower Left, but with animal breathing carbogen (95% $O_2$/5% $CO_2$) for 15 minutes. Lower Right: Difference in $pO_2$ map obtained by subtracting $pO_2$ map in Lower Left from $pO_2$ map in Lower Center (carbogen-air). Color scale now indicates change in $pO_2$ from − 12.5 to +12.5 Torr. Oxygen tension maps have been cropped to remove some of the background noise region shown in Upper Right. These data are from work performed by C. Sotak, with grateful acknowledgement to K. Helmer and M. Meiler.*


**Figure 5.** *GRE images obtained from two rat transplanted GH3 prolactinomas grown subcutaneously in the flank, acquired whilst the host breathed air and subsequently carbogen (95% $O_2$/5% $CO_2$). Images are typically heterogeneous, with regions of intense signal (long $T_2$* hence low [deoxyhaemoglobin]) becoming more so during carbogen breathing. Within some of these regions, intensity increases can be observed for structures that are attributed to large tumor blood vessels. Other regions giving rise to little or no signal (short $T_2$* hence higher [deoxyhaemoglobin]) are unaffected by carbogen breathing and probably correspond to areas of either low blood flow/hypoxia or necrosis, though this has still to be addressed. These data are from work performed by S. Robinson, with grateful acknowledgement to Prof. J.R. Griffiths.*

been observed in R3230Ac mammary adenocarcinomas [64]. Preliminary data using a novel MR-compatible fiber-optic oxygen electrode have demonstrated the simultaneous acquisition of tumor GRE MR images and $pO_2$, and increases in both signal intensity and oxygenation status with carbogen breathing [65].

The effects of carbogen breathing on the tumor metabolic phenotype have been monitored by GRE MRI interleaved with $^{31}$P-MRS, an indicator of the tumor bioenergetic state [66]. Carbogen increased both tumor GRE MR image intensity and $\beta$NTP/$P_i$. Host carbogen breathing did not change intracellular pH, whereas extracellular pH became more acidic (*vide infra*). Tissue and plasma glucose increased in response to carbogen, whilst intra- and extracellular lactate decreased, consistent with a switch to a more oxidative tumor metabolism.

Carbogen, in combination with nicotinamide, is being re-evaluated as a clinical radiosensitizer with some encouraging results [60,61]. However, breathing carbogen in the clinic has proven problematical, as such high levels of hypercapnia induce sensations of breathlessness and heat. In support of these trials and the development of appropriate gas mixtures for routine clinical use, both 1% and 2.5% $CO_2$ in oxygen were found to elicit a GRE MRI response in rat GH3 prolactinomas, the latter to a similar extent as carbogen [67]. This supports the concept that levels of hypercapnia can be reduced without loss of enhanced oxygenation and hence radiotherapeutic benefit [68].

Additionally, carbogen-induced increases in tumor blood flow have been used to enhance the uptake and efficacy of the chemotherapeutic agents ifosfamide and 5-fluorouracil, monitored by MRS [69,70]. The underlying hypothesis is that carbogen dilates the tumor blood vessels, due to $CO_2$-induced vasodilatation, resulting in improved drug delivery, with the resumption of air breathing closing down these vessels and trapping the drug.

The exact relationship between the GRE MRI response to carbogen and tumor blood oxygenation and flow is complicated, being a function of blood volume, blood vessel morphology, vascular density and blood flow. A similar approach is now being used to probe vascular maturation and function in tumor angiogenesis [16]. There is now a large amount of evidence suggesting that the increase in GRE MR image intensity of tumors with carbogen breathing is consistent with a decrease in deoxyhemoglobin, i.e., an improvement in tumor *blood* oxygenation (decrease in $\Delta T_2$*). A number of issues now need to be addressed, namely: 1) What are the precise mechanisms underlying this response? 2) Are carbogen non-responding regions indicative of areas of tumor hypoxia or necrosis? 3) Does a decrease in $T_2$* reflect an increase in *tissue* $pO_2$?, and 4) Can any prognostic/diagnostic indices be identified from this response that will be ultimately useful in the clinic?

*Tumor pH*

Tumors have long been known to generate notable amounts of lactic acid even in the presence of oxygen [71]. This has led many to postulate that tumors are acidic. Indeed, early studies with microelectrodes appeared to confirm this hypothesis, since pH values as low as 6.2 were measured in many tumors [72]. However, $^{31}$P-MRS of inorganic phosphate ($P_i$) in tumors measured pH values that were neutral-to-alkaline [73–75]. This apparent discrepancy was resolved when it was determined that the pH measured by MRS ($pH_{MRS}$) was actually measuring intracellular pH [76], and by extrapolation, microelectrodes were measuring the extracellular pH. Such reversal of pH gradients can negatively impact therapy, and this is discussed in more detail in the companion manuscript. Additionally, the apparent reversal of the pH gradient (with acid outside) has physiological and metabolic consequences to the tumor cells [77]. Low pH can also affect carcinogenesis itself. For example, culturing of primary diploid Syrian hamster embryo cells at pH 6.7 induces them to spontaneously transform to a tumorigenic phenotype [78,79]. This may occur because low pH is clastogenic, causing chromosomal strand breaks and rearrangements [80,81]. At a later stage of carcinogenesis, low pH also induces invasive, migratory behavior *in vitro* [82] as well as metastasis *in vivo* [83], apparently through the activation and release of proteases [84–87].

MR provides an almost ideal technology with which to monitor tumor pH, since it is non-invasive and non-destructive. Additionally, the resonant frequencies and behaviors of many compounds are pH-sensitive. The most

common pH indicator in use by MRS is that of endogenous $P_i$, which is sensitive primarily to the intracellular pH [88]. A number of $^{19}F$-labeled pH indicators have been developed, which report both the intra- and extracellular pH values [89–91]. These are advantageous in that there are no endogenous $^{19}F$ signals to interfere with the measurement. A $^{31}P$ indicator has also been developed which is non-toxic and is confined to the extracellular space (Ref. [92], see also companion manuscript). This is advantageous in that it allows simultaneous measurements of intracellular pH and tumor bioenergetics. More recently, $^{1}H$-labeled pH indicators based on imidazoles have been imaged in tumors to report pH "maps" of localized pH heterogeneity [93]. Methods of the future will likely be based on pH-sensitive relaxivity of contrast agents, which will allow true "pH imaging." A number of these compounds are being developed [94–97].

*Perfusion and Metabolism*

One of the unique contributions of MR methods is its ability to investigate the relationship between tumor blood flow, physiology and metabolism and to understand how the abnormal vasculature impacts on physiology and metabolism. One of the first attempts to relate tumor perfusion to metabolism was by Evelhoch *et al.* [98]. These authors observed a correlation between the well-perfused fraction (or the fraction of viable cells) and $pH_{MRS}$ and $NTP/P_i$, but not between the perfusion rate in the well-perfused fraction and $^{31}P$-NMR spectral parameters. They concluded the probable existence of a threshold in perfusion rate beyond which metabolism as measured by $^{31}P$-NMR was not significantly coupled to perfusion. Similarly, Terpstra *et al.* [99] have observed a threshold for blood flow ranging from 4.8 to 20.8 ml/100 g per minute, above which lactate was constant in a C6 rat glioma model. These putative thresholds will, however, also depend on the energy requirements and oxygen and nutrient consumption rates of the cells.

Abnormal tumor vasculature manifests itself as heterogeneity in metabolism and pH. Localized proton spectra obtained from a single tumor, frequently demonstrate heterogeneity in the distribution of lactate for $2\times2\times2$ $mm^3$ voxels through the tumor (Ref. [100], see below). This heterogeneity of lactate distribution likely translates into a heterogeneity in pH (Ref. [93], Figure 6). The versatility of current MR techniques will allow evaluation of multiparametric relationships, e.g., lactate, extracellular pH, vascular volume and permeability, non-invasively within a single tumor. Spectroscopy has also shown that interventions which acutely alter blood flow alter metabolism. For example, administration of the vasoactive agent hydralazine which reduces tumor blood flow resulted in a significant increase in lactate as detected by localized proton spectroscopy [100]. In contrast, single doses of radiation or chemotherapy can increase tumor blood flow. A single dose of 20 Gy, which significantly increased tumor blood flow as measured by $^{14}C$ iodoantipyrene [101], produced a significant increase of $NTP/P_i$, pH and a significant decrease in lactate [101,102] as measured by MR spectroscopy. Similar changes were observed with single doses of 5-fluorouracil [103,104]. These spectroscopic data provide evidence that although the physiological environment can regulate angiogenesis, vascularization can, in turn, regulate physiology and metabolism.

*Quantitative MR Studies of Glycolysis In Vivo*

Under hypoxic conditions, cells in tumors derive energy primarily from glycolysis. Even in the presence of oxygen, however, an increased capacity for glycolytic metabolism is a well-established property of neoplastic cells. Many studies of experimental tumors have provided evidence of reduced respiratory capacity and increased reliance on glycolysis for energy production. Consequently, the concentration of lactic acid in tumors is usually higher than in normal tissues. Recent human studies have revealed a positive correlation between the incidence of metastasis and the mean lactate concentration in biopsies [105,106].

*In vivo* lactate levels can be measured with $^{1}H$-MRS [107–111]. In studies of rat C6 glioma, a positive correlation has been observed between the tumor lactate level as measured *in vivo* with $^{1}H$-MRS and the neoplastic cell density as determined *ex vivo* by histopathology [112]. Several groups have also demonstrated the ability to follow glycolytic breakdown of $^{13}C$-enriched glucose to lactate. $^{13}C$ is a special NMR-active nucleus. Because it is only 1.1% naturally abundant, its consumption and conversion in tissues can be monitored in real time with tracer kinetic analyses. These MRS measurements were performed either by direct $^{13}C$ detection [113–117] or by more sensitive indirect detection of internuclear ($^{13}C$-$^{1}H$) coupling [109,111,112,118]. The incorporation of the $^{13}C$ label into glutamate, which exchanges with the TCA cycle intermediate $\alpha$-ketoglutarate, has permitted detection of respiratory metabolism in some tumors [113–117]. By supplying [1-$^{13}C$]glucose and applying the appropriate kinetic models, dynamic MRS measurements of [4-$^{13}C$]glutamate have allowed determinations of TCA cycle flux in cultured glioma cells [119]. Hence, *in vivo* MRS can provide kinetic parameters (e.g., metabolic fluxes and rate constants) to characterize neoplastic metabolism and to potentially help predict metabolic responsiveness to treatments.

Here we show results from a study of a rat C6 glioma in which $^{1}H$-MRS was used to monitor the formation of [3-$^{13}C$]lactate using inverse-detection as a function of time while infusing [1-$^{13}C$]glucose. Figure 7 shows an image of a rat brain with rectangles drawn to indicate the tissue volumes from which the $^{1}H$ spectra originated. The top panel on the right shows the time-course of [3-$^{13}C$]lactate buildup in the tumor, with an expanded view of a spectrum acquired late in the [1-$^{13}C$]glucose infusion period. For comparison, the lower panel shows a spectrum from predominantly normal brain, which was also acquired long after the [1-$^{13}C$]glucose infusion had begun. In the tumor, detectable $^{13}C$ enrichment was observed only in lactate, whereas the brain exhibited the expected $^{13}C$-labeling of glutamate, which indicated that the label cycled through the TCA cycle. Previously, low lactate levels have been observed in tissues

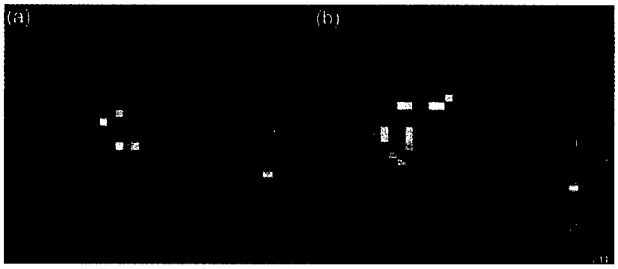


**Figure 6.** *(a) Intensity map of the H2 resonance of IEPA in a coronal slice through an MDA$^{mb}$-435 human breast cancer tumor growing in an SCID mouse. (b) Corresponding extracellular pH map, calculated from the chemical shift of the IEPA resonance (Ref. [93]) (reprinted with permission from Wiley-Liss). These data are from work performed by R. van Sluis, with grateful acknowledgement to Prof. R.J. Gillies and Dr. N. Raghunand.*

surrounding these tumors [111], and thus, the presence of [3-$^{13}$C]lactate in this brain region was most likely due to some inclusion of tumor tissue in the volume.

A kinetic model can be applied to calculate metabolic fluxes from dynamic MRS data like those shown above. For C6 glioma, the rate constant describing lactate turnover was determined to be 0.043 ± 0.007 min$^{-1}$ (mean ± SD, $n$ = 12) and the average lactate efflux was 0.41 μmol/g wet weight per minute [118], which is in reasonable agreement with autoradiographic determinations of glucose utilization. In summary, *in vivo* MRS detection of wn>13C enrichment of metabolites could conceivably become a valuable tool to monitor metabolic responsiveness of tumors to therapies over time in single subjects. Such MRS measurements may also provide important clinical information regarding metabolic properties, and possibly malignancy, of lesions that are difficult to diagnose or biopsy.

## Conclusions

Animal studies, in addition to providing important basic data on tumor physiology and metabolism, can also pave the way for advanced clinical applications. For example, Gd-based contrast agents are used in virtually every Radiological Center, although the use of time course data

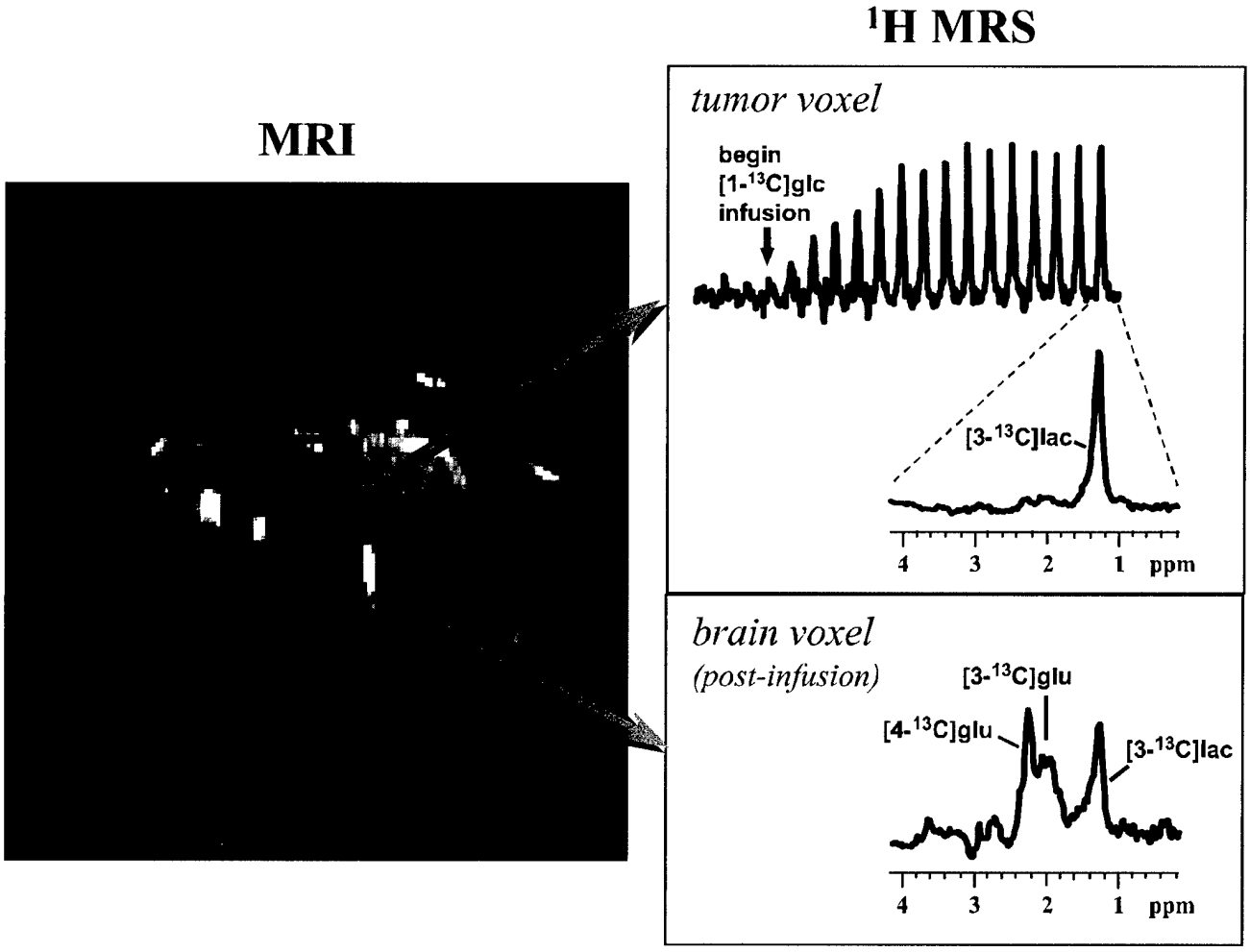


**Figure 7.** *The left panel shows a $T_2$-weighted image of a C6 glioma (coronal view). Rectangles outline two dimensions of the tissue volumes selected from tumor and the contralateral hemisphere for the spectroscopic measurements. $^{1}$H spectra from tumor (b) and contralateral hemisphere (c) were acquired while infusing [1-$^{13}$C]glucose intravenously. These spectra were acquired with a special $^{1}$H-MRS technique that detects signals from $^{13}$C-labeled compounds only. These data are from work performed by M. Garwood.*

(dynamic contrast enhancement) is not as widespread. The use of higher-molecular weight contrast agents, being developed in animals, will likely find clinical utility. BOLD experiments to assess relative deoxyhemoglobin content, can be readily applied to human tumors. Finally, even though specific indicators of physiology, such as $^{13}C$ glucose and indicators for $pO_2$ and pH, will take longer to develop, they have great clinical potential. The power of MR as a translational research tool is high, because most physical determinants of signal intensity are readily scaled from animal models to humans.

## References


[1] Goldmann E (1907). The growth of malignant disease in man and the lower animals, with special reference to the vascular system. *Proc R Soc Med* **1**, 1–13.

[2] Algire GH, Chalkley HW, Legallais FY, and Park HD (1945). Vascular Reactions of normal and malignant tissues *in vivo*: I. Vascular reactions of mice to wounds and to normal and neoplastic transplants. *J Natl Cancer Inst* **6**, 73–85.

[3] Alper T, and Howard-Flanders P (1956). Role of oxygen in modifying the radiosensitivity of *E. coli* B. *Nature* **178**, 978–979.

[4] Thomlinson RH, and Gray LH (1955). The histological structure of some human lung cancers and the possible implications for radiotherapy. *Br J Cancer* **9**, 539–549.

[5] Jain RK (1988). Determinants of tumor blood flow: a review. *Cancer Res* **48**, 2641–2658.

[6] Weidner N, Semple JP, Welch WR, and Folkman J (1991). Tumor angiogenesis and metastasis—correlation in invasive breast carcinoma. *N Engl J Med* **324**, 1–8.

[7] Horak ER, Leek R, Klenk N, LeJeune S, Smith K, Stuart N, Greenal M, Stepniewska K, and Harris AL (1992). Angiogenesis, assessed by platelet/endothelial cell adhesion molecule antibodies, as indicator of node metastases and survival in breast cancer. *Lancet* **340**, 1120–1124.

[8] Boehm T, Folkman J, Browder T, and O'Reilly MS (1997). Antiangiogenic therapy of experimental cancer does not induce drug resistance. *Nature* **390**, 404–407.

[9] Folkman J, Watson K, Ingber D, and Hanahan D (1989). Induction of angiogenesis during the transition from hyperplasia to neoplasia. *Nature* **339**, 58–61.

[10] Moses MA (1991). The Role of Vascularization in Tumor Metastasis. In: *Microcirculation in Cancer Metastasis*. F William, MR Orr Buchanan and L Weiss (Eds). CRC Press, Boca Raton, FL, pp. 257–276.

[11] Vaupel P, Kallinowski F, and Okunieff P (1989). Blood flow, oxygen and nutrient supply, and metabolic microenvironment of human tumors: a review. *Cancer Res* **49**, 6449–6465.

[12] Neufeld G, Cohen T, Gengrinovitch S, and Poltorak Z (1999). Vascular endothelial growth factor (VEGF) and its receptors. *FASEB* **13**, 9–22.

[13] Gospodarowicz D, Abraham JA, and Schilling J (1989). Isolation and characterization of a vascular endothelial cell mitogen produced by pituitary-derived folliculo stellate cells. *Proc Natl Acad Sci* **86**, 7311–7315.

[14] Ferrara N, and Henzel WJ (1989). Pituitary follicular cells secrete a novel heparin-ninding growth factor specific for vascular endothelial cells. *Biochem Biophys Res Commun* **161**, 851–858.

[15] Senger DR, Galli SJ, Dvorak AM, Perruzzi CA, Harvey VS, and Dvorak HF (1983). Tumor cells secrete a vascular permeability factor that promotes accumulation of ascites fluid. *Science* **219**, 983–985.

[16] Abramovitch R, Frenkiel D, and Neeman M (1998). Analysis of subcutaneous angiogenesis by gradient echo magnetic resonance imaging. *Magn Reson Med* **39**, 813–824.

[17] Bhujwalla ZM, Artemov D, and Glockner JF (1999). Tumor angiogenesis, vascularization, and contrast-enhanced magnetic resonance imaging. *Topics in Magnetic Resonance Imaging*, 10.

[18] Su M-Y, Wang Z, Carpenter P, Lao X, Muhler A, and Nalcioglu O (1999). Characterization of N-ethyl-N-nitrosurea induced malignant and benign breast tumors in rats using three mR contrast agents. *J Magn Reson Imag* **9**, 177.

[19] Schwarzbauer C, Syha J, and Haase A (1993). Quantification of regional blood volume by rapid T1 mapping. *Magn Reson Med* **29**, 709–712.

[20] Sipkins DA, Cheresh DA, Kazemi MR, Nevin LM, Bendarski MD, and Li KCP (1998). Detection of tumor angiogenesis *in vivo* by $\alpha_v\beta_3$-targeted magnetic resonance imaging. *Nat Med* **4**, 623–626.

[21] Larcombe McDouall JB, and Evelhoch JL (1990). Deuterium nuclear magnetic resonance imaging of tracer distribution in D2O clearance measurements of tumor blood flow in mice. *Cancer Res* **50**, 363–369.

[22] Bernsen HJJA, Rijken PFJW, Oostendorp T, and Van der Kogel AJ (1995). Vascularity and perfusion of human glioma xenografted in the athymic nude mouse. *Br J Cancer* **71** (4), 721–726.

[23] Degani H, Gusis V, Weinstein D, Fields S, and Strano S (1997). Mapping pathophysiological features of breast tumors by MRI at high spatial resolution. *Nat Med* **13** (7), 780–782.

[24] Buadu LD, Murakami J, Murayama S, Hashiguchi N, Sakai S, Masuda K, Toyoshima S, Kuroki S, and Ohno S (1996). Breast lesions: correlation of contrast medium enhancement patterns on MR images with histopathologic findings and tumor angiogenesis. *Radiology* **200**, 639–649.

[25] Hulka CA, Edmister WB, Smith BL, Tan L, Sgroi DC, Campbell T, Kopans DB, and Weiskoff RM (1997). Dynamic echo-planar imaging of the breast: experience in diagnosing breast carcinoma and correlation with tumor angiogenesis. *Radiology* **205**, 837–842.

[26] Jain RK (1987). Transport of molecules across tumor vasculature. *Cancer Metastasis Rev* **6**, 559–593.

[27] Kety SS (1951). The theory and applications of the exchange of inert gas at lungs and tissues. *Pharmacol Rev* **3**, 1–41.

[28] Larsson HBW, Stubgaard M, Frederiksen JL, Jensen M, Henriksen O, and Paulson OB (1990). Quantitation of blood-brain barrier defect by magnetic resonance imaging and gadolinium-DTPA in patients with multiple sclerosis and brain tumors. *Magn Reson Med* **16**, 117–131.

[29] Tofts PS, and Kermode AG (1991). Measurement of the blood-brain barrier permeability and leakage space using dynamic mr imaging: 1. Fundamental concepts. *Magn Reson Med* **17**, 357–367.

[30] Larsson HBW, and Tofts PS (1992). Measurements of blood-brain barrier permeability using dynamic GdDTPA scanning—a comparison of methods. *Magn Reson Med* **24**, 174–176.

[31] van der Sanden BPJ, Rozijn TH, Rijken PFJW, HPW Peters, Heerschap A, van der Kogel AJ, and Bovée WMMJ (1999). GdDTPA uptake rates are linearly related to the perfused microvessel density and surface-area in 9L-glioma growing in rat brain. *Proc Int Soc Magn Reson Med* **7**, 147.

[32] Bhujwalla ZM, Artemov D, Solaiyappan M, Mao D, and Backer JP (1999). Comparison of vascular volume and permeability for tumors derived from metastatic human breast cancer cells with and without the metastasis suppressor gene *nm23*. *Proc Int Soc Magn Reson Med* **7**, 146.

[33] Artemov D, and Bhujwalla ZM (1997). 3-Dimensional MRI quantitation of tumor vascular volume and permeability. *Proc Int Soc Magn Reson Med* **5**, 491.

[34] Braunschweiger P, and Schiffer LM (1986). Effect of dexamethasone on vascular function in RIF-1 tumors. *Cancer Res* **46**, 3299–3303.

[35] Furman-Haran E, Margalit R, Grobgeld D, and Degani H (1996). Dynamic contrast-enhanced magnetic resonance imaging reveals stress-induced angiogenesis in MCF7 human breast tumors. *Proc Natl Acad Sci U S A* **93**, 6247–6251.

[36] Hawighorst H, Weikel W, Knapstein PG, Knopp MV, Zuna I, Schonberg SO, Vaupel P, and Van Kaick G (1998). Angiogenic activity of cervical carcinoma: assessment by functional magnetic resonance imaging-based parameters and a histomorphological approach in correlation with disease outcome. *Clin Cancer Res* **4**, 2305–2312.

[37] Pham CD, Roberts TP, Van Bruggen N, Melnyk O, Mann J, Ferrara N, Cohen RL, and Brasch RC (1998). Magnetic resonance imaging detects suppression of tumor vascular permeability after administration of antibody to vascular endothelial growth factor. *Cancer Invest* **16**, 225–230.

[38] Dennie J, Mandeville JB, Boxerman JL, Packard SD, Rosen BR, and Weisskoff RM (1998). NMR imaging of changes in vascular morphology due to tumor angiogenesis. *Magn Reson Med* **40**, 793–799.

[39] Abramovitch R, Meir G, and Neeman M (1995). Neovascularization induced growth of implanted C6 glioma multicellular spheroids: magnetic resonance microimaging. *Cancer Res* **55**, 1956–1962.

[40] Gilead A, and Neeman M (1999). Dynamic remodeling of the vascular bed precedes tumor growth: MLS ovarian carcinoma spheroids implanted in nude mice. *Neoplasia* **1** (3), 226–230.

[41] Abramovitch R, Marikovsky M, Meir G, and Neeman M (1998). Stimulation of tumor angiogenesis by proximal wounds: spatial and temporal analysis by MRI. *Br J Cancer* **77**, 440–447.

[42] Schiffenbauer YS, Abramovitch R, Meir G, Nevo N, Holzinger M, Itin A, Keshet E, and Neeman M (1997). Loss of ovarian function promotes angiogenesis in human ovarian carcinoma. *Proc Natl Acad Sci U S A* **94**, 13203–13208.

[43] Robinson SP, Rodrigues LM, Ojugo AS, McSheehy PM, Howe FA, and Griffiths JR (1997). The response to carbogen breathing in experimental tumor models monitored by gradient-recalled echo magnetic resonance imaging. *Br J Cancer* **75**, 1000–1006.

[44] Carmeliet P, Dor Y, Herbert J-M, Fukumara D, Brusselmans K, Dewerchin M, Neeman M, Bono F, Abramovitch R, Maxwell P, Koch CJ, Ratcliffe P, Moons L, Jain RK, Collen D, and Keshet (1998). E Role of HIF-1a in hypoxia-mediated apoptosis, cell proliferation and tumor angiogenesis. *Nature* **394**, 485–490.

[45] Abramovitch R, Dafni H, Smouha E, Benjamin LE, and Neeman M (1999). *In vivo* prediction of vascular susceptibility to VEGF withdrawal: MRI of C6 rat glioma in nude mice. *Cancer Res*, **59**, 5012–5016.

[46] Benjamin LE, Golijanin D, Itin A, Pode D, and Keshet E (1998). Selective ablation of immature blood vessels in established human tumors follows vascular endothelial growth factor withdrawal. *J Clin Invest* **103**, 159–165.

[47] Gillies RJ, Schornack PA, Secomb TW, and Raghunand N (1999). Causes and effects of heterogeneous perfusion in tumors. *Neoplasia* **1** (3), 197–207.

[48] Mason RP (1994). Non-invasive physiology: $^{19}F$ NMR of perfluorocarbons. *Art Cells, Blood Subs, and Immob Biotech* **22**, 1141–1153.

[49] Ratner AV, Muller HH, Simpson B-B, Johnson DE, Hurd RE, Sotak C, and Young SW (1988). Detection of tumors with 19F magnetic resonance imaging. *Invest Radiol* **23**, 361–364.

[50] Sotak CH, Hees PS, Huang H-N, Hung M-H, Krespan CG, and Raynolds S (1993). A new perfluorocarbon for use in fluorine-19 magnetic resonance imaging and spectroscopy. *Magn Reson Med* **29**, 188–195.

[51] Dardzinski BJ, and Sotak CH (1994). Rapid tissue oxygen tension mapping using 19F inversion-recovery echo-planar imaging of perfluoro-15-crown-5-ether. *Magn Reson Med* **32**, 88–97.

[52] Barker BR, Mason RP, and Peshock RM (1993). Echo planar imaging of perfluoro-carbons. *Magn Reson Imaging* **11**, 1165–1173.

[53] Hees PS, and Sotak CH (1993). Assessment of changes in murine tumor oxygenation in response to nicotinamide using 19F NMR relaxometry of a perfluorocarbon emulsion. *Magn Reson Med* **29**, 303–310.

[54] Helmer KG, Han S, and Sotak CH (1998). On the correlation between the water diffusion coefficient and oxygen tension in RIF-1 tumors. *NMR Biomed* **11**, 120–130.

[55] Dardzinski BJ, Sotak CH, Isabelle A, Murray J, and Stojadinovic P (1994). Mapping the tissue oxygen tension in RIF-1 tumors following radiation therapy using inversion recovery echo planar imaging and 19F relaxometry of perfluoro-15-crown-5-ether. *Proc Int Soc Magn Reson Med* **1**, 427.

[56] Dardzinski BJ, and Sotak CH (1994). Evaluating change in murine tumor oxygenation in response to nicotinamide by using 19F echo-planar imaging and spectroscopy. *J Magn Reson Imaging* **4**, 55.

[57] Meiler MR (1999). *In vivo* characterization of RIF-1 tumors via diffusion and Fluorine-19 NMR methods, PhD Thesis, Worcester Polytechnic Institute.

[58] Horsman MR (1998). Measurement of tumor oxygenation. *Int J Radiat Oncol Biol Phys* **42**, 701–704.

[59] Rojas A (1991). Radiosensitisation with normobaric oxygen and carbogen. *Radiother Oncol (Suppl.)* **20**, 65–70.

[60] Hoskin PJ, Saunders MI, Phillips H, Cladd H, Powell MEB, Goodchild K, Stratford MRL, and Rojas A (1997). Carbogen and nicotinamide in the treatment of bladder cancer with radical radiotherapy. *Br J Cancer* **76**, 260–263.

[61] Kaanders JHAM, Pop LAM, Marres HAM, Liefers J, Van den Hoogen FJA, Van Daal WAJ, and Van der Kogel AJ (1998). Accelerated radiotherapy with carbogen and nicotinamide (ARCON) for laryngeal cancer. *Radiother Oncol* **48**, 115–122.

[62] Robinson SP, Howe FA, Rodrigues LM, Stubbs M, and Griffiths JR (1998). Magnetic resonance imaging techniques for monitoring changes in tumor oxygenation and blood flow.*Semin Radiat Oncol* **8**, 197–207.

[63] Griffiths JR, Taylor NJ, Howe FA, Saunders MI, Robinson SP, Hoskin PJ, Powell MEB, Thoumine M, Caine LA, and Baddeley H (1997). The response of human tumors to carbogen breathing, monitored by gradient-recalled echo magnetic resonance imaging. *Int J Radiat Oncol Biol Phys* **39**, 697–701.

[64] Al-Hallaq HA, River JN, Zamora M, Oikawa H, and Karczmar GS (1998). Correlation of magnetic resonance and oxygen microelectrode measurements of carbogen-induced changes in tumor oxygenation. *Int J Radiat Oncol Biol Phys* **41**, 151–159.

[65] Maxwell RJ, Robinson SP, McIntyre DJO, Griffiths JR, Young WK, and Vojnovic B (1998). Simultaneous measurement of gradient-echo $^{1}H$ MR images and $pO_2$ using a fibre-optic oxygen sensor in rodent tumors and their response to carbogen breathing. *Proc Int Soc Magn Reson Med* **3**, 1665.

[66] Robinson SP, Rodrigues LM, Griffiths JR, and Stubbs M (1999). Response of hepatoma 9618a and normal liver to host carbogen (95% $O_2$/5% $CO_2$) and carbon monoxide breathing. *Neoplasia* **1** (6), 537–543.

[67] Robinson SP, Rodrigues LM, Stubbs M, and Griffiths JR (1999). Effects of different levels of hypercapnic hyperoxia on tumor GRE MR image intensity and arterial blood gases. *Proc Int Soc Magn Reson Med* **7**, 1372.

[68] Hill SA, Collingridge DR, Vojnovic B, and Chaplin DJ (1998). Tumor radiosensitization by high oxygen content gases: influence of the inspired carbon dioxide content on pO2, microcirculatory function and radiosensitivity. *Int J Radiat Oncol Biol Phys* **40**, 943–951.

[69] Rodrigues LM, Maxwell RJ, McSheehy PMJ, Pinkerton CR, Robinson SP, Stubbs M, and Griffiths JR (1997). *In vivo* detection of ifosfamide by $^{31}P$ MRS in rat tumors: increased uptake and cytotoxicity induced by carbogen breathing in GH3 prolactinomas. *Br J Cancer* **75**, 62–68.

[70] McSheehy PMJ, Robinson SP, Ojugo ASE, Aboagye EO, Cannell MB, Leach MO, Judson IR, and Griffiths JR (1998). Carbogen breathing increases 5-fluorouracil uptake and cytotoxicity in hypoxic murine RIF-1 tumors: a magnetic resonance study *in vivo*. *Cancer Res* **58**, 1185–1194.

[71] Warburg O (1956). On the origin of cancer cells. *Science* **123**, 309–314.

[72] Wike-Hooley JL, Haveman J, and Reinhold HS (1984). The relevance of tumour pH to the treatment of malignant disease. *Radiother Oncol* **2**, 343–366.

[73] Hwang YC, Kim SG, Evelhoch JL, and Ackerman JJH (1992). Nonglycolytic acidicification of murine radiation-induced fibrosarcoma 1 tumor via 3-O-methyl-d-glucose monitored by 1H, 2H, 13C, and 31P magnetic resonance spectroscopy. *Cancer Res* **52**, 1259–1266.

[74] Bhujwalla ZM, Blackband SJ, Wehrle JP, Grossman S, Eller S, and Glickson JD (1990). Metabolic heterogeneity in RIF-1 tumours detected *in vivo* by $^{31}P$ NMR spectroscopy. *NMR Biomed* **3**, 233–238.

[75] Raghunand N, Altbach MI, Van Sluis R, Baggett B, Taylor CW, Bhujwalla ZM, and Gillies RJ (1998). Plasmalemmal pH-gradients in drug-sensitive and drug-resistant MCF-7 human breast carcinoma xenografts measured by $^{31}P$ MR spectroscopy. *Biochem Pharmacol* **57**, 309–312.

[76] Griffiths JR (1991). Are cancer cells acidic? *Br J Cancer* **64**, 425–427.

[77] Stubbs M, Rodrigues L, Howe FA, Wang J, Jeong KS, Veech RL, and Griffiths JR (1994). Metabolic consequences of a reversed pH gradient in rat tumors. *Cancer Res* **54**, 4011–4016.

[78] LeBoeuf RA, and Kerckaert GA (1987). Enhanced morphological transformation of early passage syrian hamster embryo cells cultured in medium with a reduced bicarbonate concentration and pH. *Carcinogenesis* **8**, 689–697.

[79] LeBoeuf RA, Lin P, Kerckaert G, and Gruenstein E (1992). Intracellular acidification is associated with enhanced morphological transformation in syrian hamster embryo cells. *Cancer Res* **52**, 144–148.

[80] Morita T, Nagaki T, Fukuda I, and Okumura K (1992). Clastogenicity of low pH to various cultured mammalian cells. *Mutat Res* **268**, 297–305.

[81] Morita T, Takeda K, and Okumura K (1990). Evaluation of clastogenicity of formic acid, acetic acid, and lactic acid on cultured mammalian cells. *Mutat Res* **240**, 195–202.

[82] Martinez-Zaguilan R, Seftor EA, Seftor REB, Chu YW, Gillies RJ, and Hendrix MJC (1996). Acidic pH enhances the invasive behavior of human melanoma cells. *Clin Exp Metastasis* **14**, 176–186.

[83] Schlappack OK, Zimmermann A, and Hill RP (1991). Glucose

starvation and acidosis: effect on experimental metastasic potential, DNA content and MTX resistance of murine tumour cells. *Br J Cancer* **64**, 663–670.

[84] Montcourrier P, Silver I, Farnoud R, Bird I, and Rochefort H (1995). Breast cancer cells have a high capacity to acidify extracellular milieu by a dual mechanism. *Clin Exp Metastasis* **15**, 382–392.

[85] Rozhin J, Sameni M, Ziegler G, and Sloane BF (1994). Pericellular pH affects distribution and secretion of cathepsin B in malignant cells. *Cancer Res* **54**, 6517–6525.

[86] Cuvier C, Jang A, and Hill RP (1997). Exposure to hypoxia, glucose starvation and acidosis: effect on invasive capacity of murine tumor cells and correlation with cathepsin (L+B) secretion. *Clin Exp Metastasis* **15**, 19–25.

[87] Jang A, and Hill RP (1997). An examination of the effects of hypoxia, acidosis, and glucose starvation on the expression of metastasis-associated genes in murine tumor cells. *Clin Exp Metastasis* **15**, 469–483.

[88] Stubbs M, Bhujwalla ZM, Tozer GM, Rodrigues LM, Maxwell RJ, Morgan R, Howe FA, and Griffiths JR (1992). An assessment of 31P MRS as a method of measuring pH in rat tumors. *NMR Biomed* **5**, 351–359.

[89] Taylor JS, and Deutsch C (1983). Fluorinated-methylamino acids as 19-F NMR indicators of intracellular pH. *Biophys J* **43**, 261–267.

[90] Mason RP (1999). Transmembrane pH gradients *in vivo*: measurements using fluorinated vitamin B6 derivatives. *Curr Med Chem* **6** (6), 481–499.

[91] Aoki Y, Akagi K, Tanaka Y, Kawai J, and Takahashi M (1996). Measurement of intratumor pH by pH indicator used in 19F-magnetic resonance spectroscopy. Measurement of extracellular pH decrease caused by hyperthermia combined with hydralazine. *Invest Radiol* **31** (11), 680–689.

[92] Gillies RJ, Liu Z, and Bhujwalla ZM (1994). 31P MRS measurements of extracellular pH of tumors using 3-aminopropylphosphonate. *Am J Physiol* **267** (36), C195–C203.

[93] Van Sluis R, Bhujwalla Z, Raghunand N, Ballesteros P, Alvarez J, Cerdan S, and Gillies RJ (1999). Imaging of extracellular pH of tumors using 1H MRSI. *Magn Reson Med* **41**, 743–750.

[94] Zhang S, Wu K, and Sherry AD (1999). A novel pH-sensitive MRI contrast agent. *Angew Chem, Int Ed Engl*, in press.

[95] Ward KM, and Balaban RS (1999). Determination of pH using water proton chemical exchange: potential pH sensitive MRI contrast agents. *Proc Int Soc Magn Reson Med* **7**, 1197.

[96] Rowland IJ, Murphy PS, Schwarz A, Botta M, Aime S, and Leach MO (1998). *In vivo* extracellular pH mapping at 1.5 T using proton CSI. *Proc Int Soc Magn Reson Med* **6**, 54.

[97] Beauregard DA, Parker D, and Brindle KM (1998). Relaxation-based mapping of tumour pH. *Proc Int Soc Magn Reson Med* **6**, 53.

[98] Evelhoch JL, Sapareto SA, Nussbaum GH, and Ackerman JJH (1986). Correlation between 31P NMR spectroscopy and 15O perfusion measurements in the RIF1 murine tumor *in-vivo*. *Radiat Res* **106**, 122–131.

[99] Terpstra M, High WB, dGRA LY, Merkle H, and Garwood M (1996). Relationships among lactate concentration, blood flow and histopathologic profiles in rat C6 glioma. *NMR Biomed* **9**, 185–194.

[100] Bhujwalla ZM, Shungu DC, and Glickson JD (1996). Effects of blood flow modifiers on tumor metabolism observed *in vivo* by proton magnetic resonance spectroscopic imaging. *Magn Reson Med* **36**, 204–211.

[101] Tozer GM, Bhujwalla ZM, Griffiths JR, and Maxwell RJ (1989). Phosphorus-31 magnetic resonance spectroscopy and blood perfusion of the RIF-1 tumor following X-irradiation. *Int J Radiat Oncol Biol Phys* **16**, 155–164.

[102] Bhujwalla ZM, and Glickson JD (1996). Detection of tumor response to radiation therapy by *in vivo* proton MR spectroscopy. *Int J Radiat Oncol Biol Phys* **36** (3), 635–639.

[103] Bhujwalla ZM, McCoy CL, Glickson JD, Gillies RJ, and Stubbs M (1998). Non-invasive measurements of intra- and extracellular spaces and pH of tumors, before and after 5-fluorouracil, by 31P MR spectroscopy. *Br J Cancer* 606–611.

[104] Aboagye EO, Bhujwalla ZM, Shungu DC, and Glickson JD (1998). Detection of tumor response to chemotherapy by 1H nuclear magnetic resonance spectroscopy: effect of 5-fluorouracil on lactate levels in radiation-induced fibrosarcoma 1 tumors. *Cancer Res* **58**, 1063–1067.

[105] Schwickert G, Walenta S, Sundfor K, Rofstad EK, and Mueller-Klieser W (1995). Correlation of high lactate levels in human cervical cancer with incidence of metastasis. *Cancer Res* **55**, 4757–4759.

[106] Walenta S, Salameh A, Lyng H, Evensen JF, Mitze M, Rofstad EK, and Mueller-Klieser W (1997). Correlation of high lactate levels in head and neck tumors with incidence of metastasis. *Am J Pathol* **150**, 409–415.

[107] Hurd RE, and Freeman DM (1989). Metabolite specific proton magnetic resonance imaging. *Proc Natl Acad Sci U S A* **86**, 4402–4406.

[108] De Graaf AA, Luyten PR, Den Hollander JA, Heindel W, and Bovee WMMJ (1993). Lactate imaging of the human brain at 1.5 T using a double-quantum filter. *Magn Reson Med* **30**, 231–235.

[109] Schupp DG, Merkle H, Ellermann JM, Ke Y, and Garwood M (1993). Localized detection of glioma glycolysis using edited $^{1}$H MRS. *Magn Reson Med* **30**, 18–27.

[110] He Q, Shungu DC, Van Zijl PCM, Bhujwalla ZM, and Glickson JD (1995). Single-scan *in vivo* lactate editing with complete lipid and water suppression by selective multiple-quantum-coherence transfer (Sel-MQC) with application to tumors. *J Magn Reson, Ser B* **106**, 203–211.

[111] De Graaf RA, Luo Y, Terpstra M, and Garwood M (1995). Spectral editing with adiabatic pulses. *J Magn Reson, Ser B* **109**, 184–193.

[112] Terpstra M, High WB, Luo Y, de Graaf RA, Merkle H, and Garwood M (1996). Relationships among lactate concentration, blood flow, and histopathologic profiles in rat C6 glioma. *NMR Biomed* **9**, 185–194.

[113] Ross BD, Higgins RJ, Boggan JE, Willis JA, Knittel B, and Unger SW (1988). Carbohydrate metabolism of the rat C6 glioma. An *in vivo* $^{13}$C and *in vitro* $^{1}$H magnetic resonance spectroscopy study. *NMR Biomed* **1**, 20–26.

[114] Lyon RC, Tschudin RG, Daly PF, and Cohen JS (1988). A versatile multinuclear probe designed for *in vivo* NMR spectroscopy: applications to subcutaneous human tumors in mice. *Magn Reson Med* **6**, 1–14.

[115] Constantinidis I, Chatham JC, Wehrle JP, and Glickson JD (1991). *In vivo* $^{13}$C NMR spectroscopy of glucose metabolism of RIF-1 tumors. *Magn Reson Med* **20**, 17–26.

[116] Ronen SM, Volk A, and Mispelter J (1994). Comparative NMR study of a differentiated rat hepatoma and its dedifferentiated subclone cultured as spheroids and as implanted tumors. *NMR Biomed* **7**, 278–286.

[117] Artemov D, Bhujwalla ZM, and Glickson JD (1995). *In vivo* selective measurement of {1-$^{13}$C}-glucose metabolism in tumors by heteronuclear cross polarization. *Magn Reson Med* **33**, 151–155.

[118] Terpstra M, Gruetter R, High WB, Mescher M, DelaBarre L, Merkle H, and Garwood M (1998). Lactate turnover in rat glioma measured by *in vivo* nuclear magnetic resonance spectroscopy. *Cancer Res* **58**, 5083–5088.

[119] Portais J-C, Schuster R, Merle M, and Canioni P (1993). Metabolic flux determination in C6 glioma cells using carbon-13 distribution upon [1-$^{13}$C] glucose incubation. *Eur J Biochem* **217**, 457–468.

Magnetic Resonance in Medicine 41:743–750 (1999)

# In Vivo Imaging of Extracellular pH Using $^1$H MRSI

Robert van Sluis,[1] Zaver M. Bhujwalla, [2] Natarajan Raghunand, [1] Paloma Ballesteros, [3] José Alvarez, [4] Sebastián Cerdán, [4] Jean-Philippe Galons, [1] and Robert J. Gillies[1]*

**Tumor pH is physiologically important since it influences a number of processes relevant to tumorigenesis and therapy. Hence, knowledge of localized pH within tumors would contribute to understanding these processes. The destructiveness, poor spatial resolution, and poor signal-to-noise ratio (SNR) of current technologies (e.g., microelectrodes, $^{31}$P magnetic resonance spectroscopy) have limited such studies. An extrinsic chemical extracellular pH ($pH_e$) probe is described that is used in combination with $^1$H magnetic resonance spectroscopic imaging to yield $pH_e$ maps with a spatial resolution of 1 × 1 × 4 mm$^3$. The principle of the technique is demonstrated on a phantom. Further data are shown to demonstrate its application in vivo, and results agree with previously reported pH values. The accuracy of the reported pH measurements is <0.1 pH units, as derived from a detailed analysis of the errors associated with the technique, the description of which is included. Magn Reson Med 41:743–750, 1999.** © 1999 Wiley-Liss, Inc.

**Key words: cancer; imidazole; MRSI; pH; tumor**

Since the discovery of lactic acid production in tumors more than 50 years ago (1), it has generally been assumed that the pH of tumors is acidic. Indeed, numerous microelectrode measurements have shown that extracellular tumor pH ($pH_e$) is acidic (2). This acidic $pH_e$ of tumors has been confirmed with less invasive $^{31}$P magnetic resonance spectroscopy (MRS) measurements (3). Although the intracellular pH ($pH_i$) of tumors remains neutral to alkaline (4,5), it is somewhat influenced by the $pH_e$ (6).

An acidic $pH_e$ of tumors is physiologically important since it influences a number of processes relevant to carcinogenesis and therapy. Knowledge of localized pH within tumors, both intra- and extracellular, would allow more detailed study of these processes and relate them to intratumoral pH heterogeneity. For example, it has been found that low $pH_e$ in vitro causes tumorigenic transformation of primary Syrian hamster embryo cells (7) and can lead to chromosomal rearrangements in Chinese hamster embryo cells (8,9). Furthermore, culturing cells at low pH causes them to be more invasive in vitro (10) and metastatic in vivo (11). Finally, the orientation of the pH gradient across the cell membrane may influence cell drug resistance (6,12)

Previously reported measurements of extracellular pH using either microelectrodes or $^{31}$P MRS of 3-aminopropylphosphonate (3-APP) (3) have drawbacks. Microelectrodes are invasive and can destroy the membrane integrity, thereby disrupting the mechanism for maintaining the $pH_e$. $^{31}$P MRS does not suffer this drawback and has the additional advantage of permitting simultaneous measurements of intracellular pH. However, the limited sensitivity of $^{31}$P MRS allows measurements of $pH_e$ only from relatively large tissue volumes. Hence, $^{31}$P MRS provides measurements of pH ranges rather than different pH values for discrete spatial locations (13).

The use of $^1$H MRS, inherently more sensitive than $^{31}$P MRS, would allow measurements of pH over smaller tissue volumes. For example, the imidazole protons of histidine have long been useful as intracellular pH indicators in NMR (14,15).

Rabenstein and Isab (16) first proposed using imidazoles as extrinsic $pH_e$ indicators. Gil et al (17) suggested several modifications of the basic structure of the imidazole molecule to improve its performance as an extrinsic pH probe. To date, the most promising candidate for a $^1$H nuclear magnetic resonance (NMR)-sensitive $pH_e$ indicator is the H2 resonance of (±) 2-imidazole-1-yl-3-ethoxycarbonyl propionic acid (IEPA), which has been shown to remain in the extracellular environment (17) Results from toxicity studies and preliminary in vivo data using IEPA have been reported previously (18,19).

Here, we present both phantom and in vivo data that demonstrate the feasibility of localized, multi-voxel $pH_e$ measurements using $^1$H magnetic resonance spectroscopic imaging (MRSI). Furthermore, a detailed discussion of the sources and (where possible) the quantification of errors associated with the proposed measurement technique is included.

## MATERIALS AND METHODS

### Titration of IEPA

Titration data for IEPA were obtained from bovine serum containing 20 mM IEPA, to which 20 mM EDTA and 10% v/v deuterium oxide ($D_2O$) were added for preservation and shimlock purposes, respectively. As a chemical shift reference, 10 mM 3-(trimethylsilyl) tetradeutero sodium propionate (TSP) was also added. The pH of the solution was adjusted at 37°C using 5 N solutions of NaOH and HCl to 19 pH values between 4.7 and 8.0 and the chemical shift of the H2 IEPA resonance was measured at 37°C in the spectrum for each pH value. Figure 1 shows the chemical structure and a high-resolution (9.4 T) $^1$H spectrum of IEPA at pH 7.0.

[1]Departments of Biochemistry and Radiology, The University of Arizona, Tucson, Arizona.

[2]Department of Radiology, Johns Hopkins University School of Medicine, Baltimore, Maryland.

[3]Department of Chemistry, UNED, Madrid, Spain.

[4]Magnetic Resonance Laboratory, IIB CSIC, Madrid, Spain.

Grant sponsor: US Army Breast Cancer Initiative; Grant numbers: DAMD17–94-J-4368, DAMD17–96–1-6131, PB93–0037, and PB94–011.

Presented in part at the 1998 meeting of the ISMRM, Sydney, Australia, poster #1642.

*Correspondence to: Robert J. Gillies, The University of Arizona Health Sciences Center, PO Box 245042, Tucson, AZ 85724–5042.
E-mail: gillies@u.arizona.edu

Received 19 June 1998; revised 5 October 1998; accepted 5 October 1998.

The Henderson-Hasselbalch equation for IEPA is given by

$$pH = pK_a - \log_{10}\left(\frac{\delta_{obs} - \delta_{acid}}{\delta_{base} - \delta_{obs}}\right), \qquad [Eq.1]$$

where pH is the observed pH, $pK_a$ is the negative $\log_{10}$ of the acid dissociation constant, and $\delta_{obs}$, $\delta_{acid}$, and $\delta_{base}$ are the chemical shifts of the observed, the fully protonated, and the fully deprotonated IEPA peaks, respectively. The experimental data were fitted to Eq.[1] through nonlinear regression (Sigmaplot 3.0, Jandel), and the results are shown in Fig. 2. The fit is characterized by the following set of parameters and their respective standard errors:

$$pK_a = 6.49 \pm 0.02;$$

$$\delta_{acid} = 8.92 \pm 0.01;$$

$$\delta_{base} = 7.77 \pm 0.01.$$

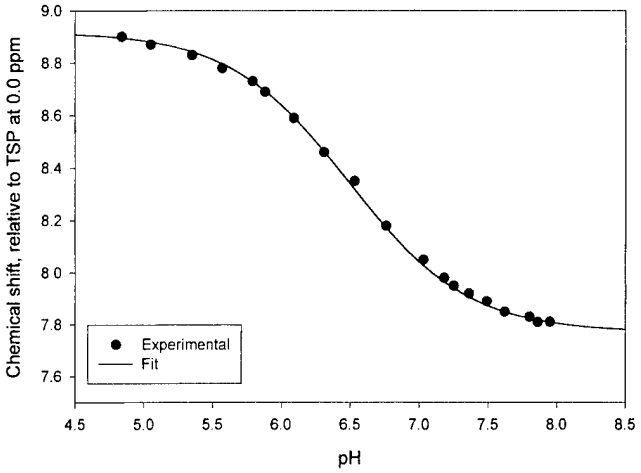


FIG. 2. Chemical shift of the H2-IEPA resonance relative to TSP, as a function of pH in bovine serum at 37°C. Measured data are shown as points, and the curve results from a nonlinear regression of the experimental data to Eq. [2].

### MRSI Experiments

All MRSI experiments were performed on a 4.7 T GE Omega scanner, using the BASSALE sequence (20) and a two-turn $^1H$ surface coil. Two-dimensional (2D) water-suppressed MRSI data were obtained from a 4 mm coronal slice, phase-encoding dimensions of $2 \times 2$ mm$^2$ and $16 \times 16$ steps. The fields of view (FOVs) in all imaging and MRSI studies were $32 \times 32$ mm$^2$.

A three-compartment phantom was constructed, consisting of two 5 mm NMR tubes inside a larger, 12 mm glass cylinder. The two inner tubes were filled with 20 mM IEPA at pH values of 6.5 and 7.5, respectively. The third, outer compartment was filled with saline. $^1H$ MRSI data were acquired with a TE of 100 msec, TR of 2 sec, 512 points, spectral width (SW) of 6000 Hz, 4 averages. A separate data set was obtained without water suppression to correct for susceptibility effects.

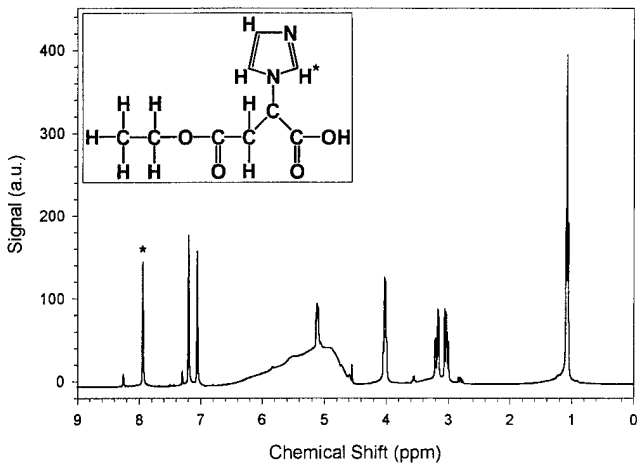


FIG. 1. Structure and 9.4 T $^1H$ NMR spectrum of IEPA in solution (pH 7.0). The pH-sensitive resonance and the C2 proton from which it originates are indicated by asterisks. The broad resonance in the center of the spectrum is due to residual water.

In vivo studies were performed on human breast cancer cells (MCF-7 and MDA$^{mb}$-435), grown in the mammary fat pad of severe combined immunodeficient (SCID) mice. Tumor volumes studied were 300–600 mm$^3$. The mice were anesthetized with ketamine (50 mg/kg) and acepromazine (5 mg/kg), and 0.15 ml of a 310 mM IEPA solution was injected intra-peritoneally. The animals were immobilized on a home-built MR cradle, and body temperature was maintained using a warm water blanket. $^1H$ MRSI data were acquired with a TE of 32 msec, TR of 2 sec, 128 points, SW of 6000 Hz, and 8 averages. The total measurement time was 34 min. A separate data set was obtained without water suppression to correct for susceptibility effects.

All data were processed using an MRSI processing program, developed in-house and written in Interactive Data Language (IDL, Research Systems, Boulder, CO). The raw $^1H$ MRSI data were Hanning filtered in *k*-space, and zero filled once in both *k*-space and in the time domain prior to 3D Fourier transformation.

## RESULTS AND DISCUSSION

### Phantom Data

The chemical shift of the H2 resonance of IEPA was determined for the maximum peak occurring between 7.77 and 8.92 ppm (the H2 proton titratable range) in each of the MRSI spectra. Chemical shifts in each voxel were referenced to unsuppressed water at 4.7 ppm to correct for susceptibility effects, and converted to pH values using Eq. [1]. The pH values from each voxel were color-encoded. Peaks lower than 10% of the maximum IEPA intensity were discarded, and results are shown in Fig. 3.

It is clear from Fig. 3b that the pH imaging technique allows the two compartments of the phantom to be distinguished. Furthermore, the reported pH values are in good agreement with the calibration values of 6.5 and 7.5 pH units. Note that the pH 6.5 compartment is spread over more voxels than the pH 7.5 compartment. Over the pH range 5–8, the $T_2$ of the C2 proton of IEPA decreases from 101 ± 12 msec to 61 ± 4 msec. In spin-echo sequences like

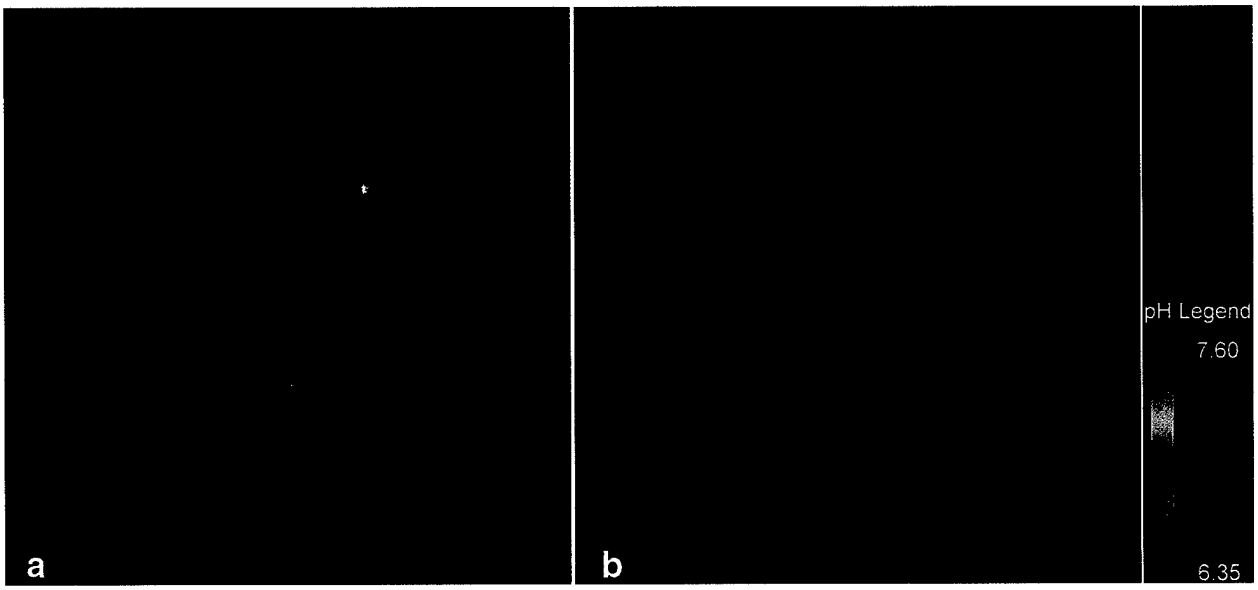


FIG. 3. **a:** Coronal image through the three compartment phantom, showing the two tubes with pH 6.5 (bottom left) and pH 7.5 (top right). The bright spot is a capillary filled with Gd-DTPA, used for orientation purposes. **b:** pH map and legend for the phantom. The pixel size in the pH map is 1 $mm^2$.

BASSALE, resonances with a longer $T_2$ will have a higher signal intensity than resonances with a shorter $T_2$. Since the $T_2$ of the C2 proton of IEPA decreases with increased pH, the H2-IEPA resonance from the lower pH compartment will have a higher intensity than the H2-IEPA resonance from the higher pH compartment. The degree of contamination due to the point spread function (PSF) is proportional to the intensity of the signal from which the contamination arises (21). As a result the contamination for the pH 6.5 compartment extends over more neighboring voxels compared with the pH 7.5 compartment. Furthermore, this $T_2$ weighting could lead to an underestimate of the reported pH value. The decrease of $T_2$ with increasing pH is consistent with the known increase in the exchange rate with solvent of protons from primary and secondary amines and amides (22). Increasing solvent exchange rate would tend to decrease $T_2$ values of the imidazolic protons because of an increased magnetization transfer to the surrounding solvent. Regardless of the exact underlying mechanisms of the $T_2$ dependence on pH, it is clear that $^1H$ MRSI of the H2 proton of IEPA allows us to produce a pH map of the phantom and distinguish between the two compartments, as shown in Fig. 3.

### In Vivo Data

An illustration of the quality of our in vivo MRSI data, an array of 7 × 7 spectra, is shown in Fig. 4. These data demonstrate that the H2 resonance of IEPA is observable with good SNR in 15–20 voxels in the tumor. Pre-injection spectra contain a small resonance in the 7–9 ppm region corresponding to endogenous imidazole (data not shown). This resonance was smaller than that in, for example, voxel (9,12), and did not affect subsequent measurements.

Some voxels, in particular [10,8], [10,9], and [10,10], bracketed in Fig. 4, show the presence of a complex H2-IEPA resonance, which may result from the presence of two or more pools of distinct $pH_e$ values. In all spectra, the H2-IEPA resonance is rather broad. The short $T_2^*$ of this resonance in vivo does not allow a finer sampling of the spectrum without ramifications for the SNR. At present, the optimum spectral sampling interval is 0.23 ppm/point, which is coarse. Clearly, this is an aspect of the work that needs improvement.

For construction of the $pH_e$ map from the in vivo data, the chemical shift of the H2 resonance of IEPA was determined using a center of gravity (COG) calculation (23) over the titratable chemical shift range for this proton. The calculation was weighted by the shape of the titration curve to correct for its non-linearity (24). Over the titratable range of the IEPA C2 proton, the weighting function is the partial derivative of the observed chemical shift with respect to the pH for Eq. [1], and is given by:

$$\frac{\partial \delta_{obs}}{\partial pH} = \frac{2.3(\delta_{acid} - \delta_{obs})(\delta_{obs} - \delta_{base})}{(\delta_{acid} - \delta_{base})} \qquad \text{[Eq. 2]}$$

Outside the titratable range, the weighting function is zero. As before, chemical shift values were references to unsuppressed water at 4.7 ppm to correct for susceptibility effects and the calculated pH values were color-encoded. Peaks lower than 10% of the maximum IEPA intensity were discarded. Results are shown in Fig. 5.

The intensity of the H2-IEPA resonance is the largest in the center of the tumor (Fig. 5a). Since tumor perfusion is generally worse in the center of a tumor than in the periphery, one would expect to find a higher concentration of IEPA in the periphery of the tumor compared with the center. However, the observed intensity distribution is likely to be caused by the application of the Hanning filter to the raw data. This filter reduces the signal intensity at the edges of the FOV, to reduce ringing artifacts. As a result, data in the center of the FOV appear to be at a higher intensity.

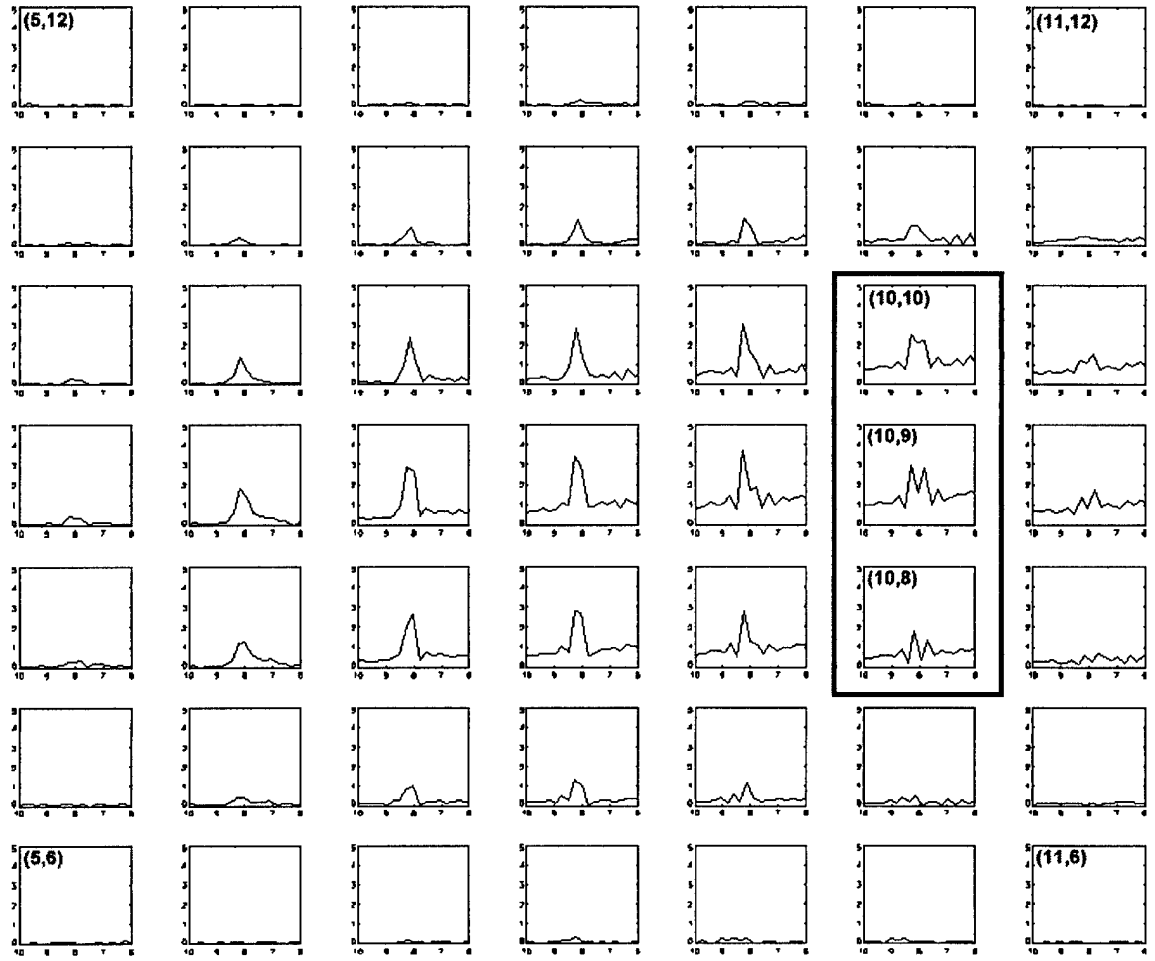


FIG. 4. Array of 7 × 7 in vivo $^1$H MRSI spectra used for the determination of $pH_e$ in the tumor. The H2-IEPA resonance is clearly visible in the majority of the spectra. The displayed chemical shift range is 10–6 ppm. Note that for these spectra, the voxel size is 2 × 2 mm$^2$. For construction of the $pH_e$ map, data were interpolated in *k*-space to yield a voxel size of 1 mm$^2$. The boxed spectra, [10,8], [10,9], and [10,10] are discussed in detail in the text.

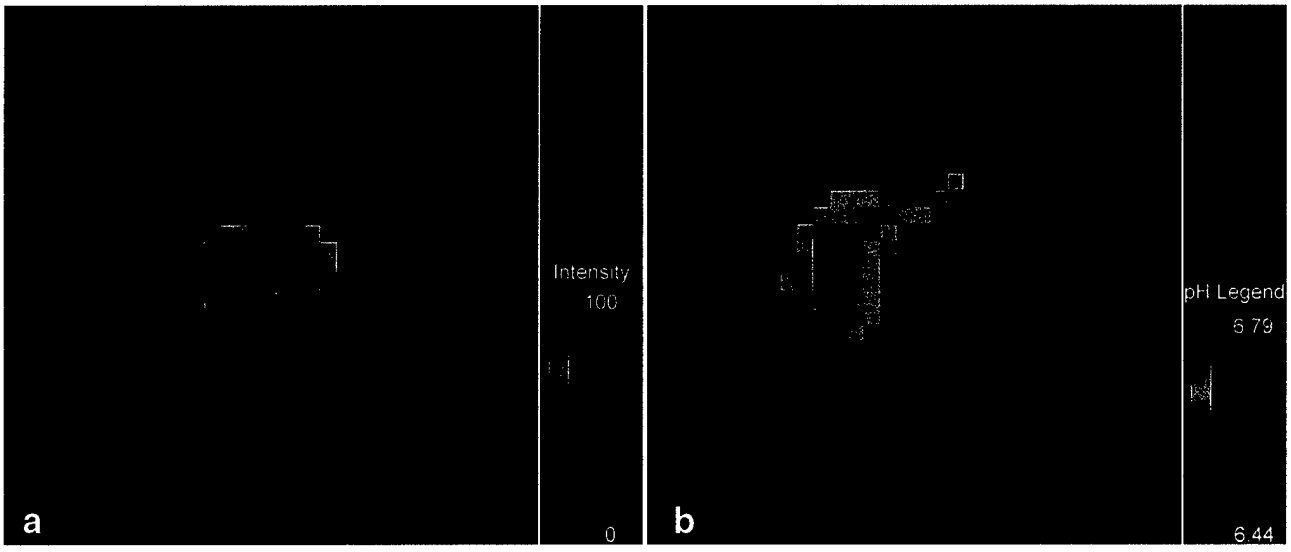


FIG. 5. **a:** Intensity map of the H2-resonance of IEPA in a coronal slice through an MDA$^{mb}$-435 tumor. **b:** Corresponding $pH_e$ map. In both the intensity and $pH_e$ map, the pixel size is 1 mm$^2$.

As expected, the data show a good correlation between the signal intensity distribution and the extent of the $pH_e$ map (cf. Fig. 5a and b). Across the tumor, the observed extracellular pH in the tumor is heterogeneous and acidic ($6.44 < pH_e < 6.79$), with a volume average $pH_e$ of $6.64 \pm 0.07$. This is in good agreement with previous studies (13). Furthermore, it is seen that there are several discrete areas of fairly homogeneous $pH_e$ within the tumor, with areas between 4 and 9 $mm^2$ (Fig. 5b). The largest continuous area within the tumor appears to have an average $pH_e$ of 6.6, as read from the legend.

## Error Analysis

The pH ranges as reported in Figs. 3b and 5b have associated errors resulting from artifacts in the measurement technique. The errors associated with the calibration of the $pH_e$ are relatively small (see above), so that the measurement technique proposed above has two remaining sources of error to be considered. First, the COG method used in determining the peak position will have an accuracy dependent on the linewidth and SNR of the peak under observation. Second, signal modulation due to the PSF, an inherent source of error in any MRSI measurement (21), will cause signals to "bleed" into adjacent voxels. This voxel bleed artifact depends on the intensity and chemical shift differences existing between adjacent voxels. Intensity differences may be caused by changes in the IEPA relaxation times with pH or by differences in IEPA concentration between adjacent voxels. Chemical shift differences between voxels may be caused by $pH_e$ differences. These sources of error will be described in more detail below.

### *Accuracy of the COG Method*

To study the accuracy of the COG method for determination of pH from our spectra, we simulated C2 IEPA resonances for pH values 6.0, 6.5, 7.0, and 7.5, with a spectral resolution of 0.23 ppm/point. Resonances were simulated with different linewidths as defined by the full width at half-maximum (FWHM). Gaussian noise was added to the IEPA resonance to yield SNRs of approximately 20, 10, and 5. The pH as determined by the COG method was compared with the pH as entered into the simulation and the absolute error gives a measure of the accuracy of the COG method in determining the pH. Results are shown in Fig. 6.

The error in the reported pH increases with decreasing SNR, for all linewidths, as expected. Furthermore, the pH is reported more accurately near the $pK_a$ of the C2 IEPA proton, which is 6.49. This is due to the nonlinearity of the titration curve.

It is also observed that the error in the reported pH increases as the H2-IEPA resonance linewidth decreases (see Fig. 6a and 6c). This is directly related to the spectral resolution in the simulated data (0.23 ppm/point). As peaks narrow, the lines are defined by fewer and fewer points, and with the FWHM approaching the spectral resolution, the determination of the position of the maximum peak intensity by the COG method becomes stochastic. However, for reasonable SNRs (>5) and broader peaks (FWHM > 0.16 ppm), as observed in our in vivo spectra, the accuracy of the COG method is better than 0.1 pH units in the range from pH 6.0 to pH 7.0.

### *Modeling PSF Artifacts*

Wang et al (25) have proposed a model to calculate voxel bleed artifacts due to concentration differences alone. Here, we have modified their model to study the combined effects of inhomogeneities in both $pH_e$ and IEPA concentration.

For simulations, an $8 \times 8$ grid of IEPA free induction decays (FIDs) was established, with voxel coordinates running from [0,0] to [7,7]. In the descriptions below, voxel [4,4] was used as the "center voxel". Initial simulations demonstrated that the worst contamination occurs in the center voxel when the signal intensity ratio is maximum, i.e., an empty voxel surrounded by voxels of non-zero IEPA concentration. Also, the contamination is worst between nearest neighbor voxels, i.e., the main contributors to the contamination in the center voxel are the 8 voxels immediately surrounding it. These results are in agreement with those of Wang et al (25).

Quantitative estimates of the actual degrees of IEPA concentration and $pH_e$ inhomogeneities in vivo are required before continuing analysis of their effects on the precision of the proposed pH imaging technique.

### *Estimating IEPA Concentration Inhomogeneity*

Since voxel bleed artifacts prevent direct derivation of quantitative information on IEPA concentration inhomogeneity from the MRSI data, studies of the uptake of dimeglumine gadopentetate (Gd-DTPA, Schering, Germany) in MCF-7 tumors were monitored by $T_2$-weighted imaging as a model for the IEPA concentration distribution. IEPA and Gd-DTPA are comparable in terms of partition coefficient and charge. Both molecules are about the same size, and their charges are -2 for Gd-DTPA (Gd +3, DTPA -5) and 0 to -1 for IEPA (acid group -1, imidazolic nitrogen +0 to +1).

One precontrast ($t = 0$) and 16 Gd-DTPA-enhanced images (17 mm surface coil, FOV 25 $mm^2$, $128 \times 128$ pixels, slice thickness 4 mm) were obtained at regular intervals over the course of 110 min from three consecutive sagittal slices through MCF-7 tumors. Gd-DTPA-enhanced images were subtracted from the precontrast image to yield images of the Gd-DTPA enhancement only, which to a first approximation is linear with Gd-DTPA concentration (26). These subtraction images were rebinned to $16 \times 16$ pixels to yield a pixel size of 1.56 $mm^2$, approximating the 2 $mm^2$ spatial resolution used when acquiring the IEPA MRSI data. Examples of a high-resolution ($128 \times 128$) and rebinned ($16 \times 16$) images of Gd-DTPA enhancement are shown in Fig. 7.

In each of the rebinned subtraction images, 6 pixels were identified that represent the Gd-DTPA distribution in the tumor and, for these 6 pixels, the intensity ratios between nearest neighbors were calculated. The highest and the average nearest neighbor intensity ratios were determined for each image and plotted as a function of time, as shown in Fig. 8. It can be seen that once a steady-state Gd-DTPA concentration has been reached (after 6–8 min), the highest and average intensity ratios stabilize at about 1:3.0 and 1:1.5, respectively. Using these values as a measure of the

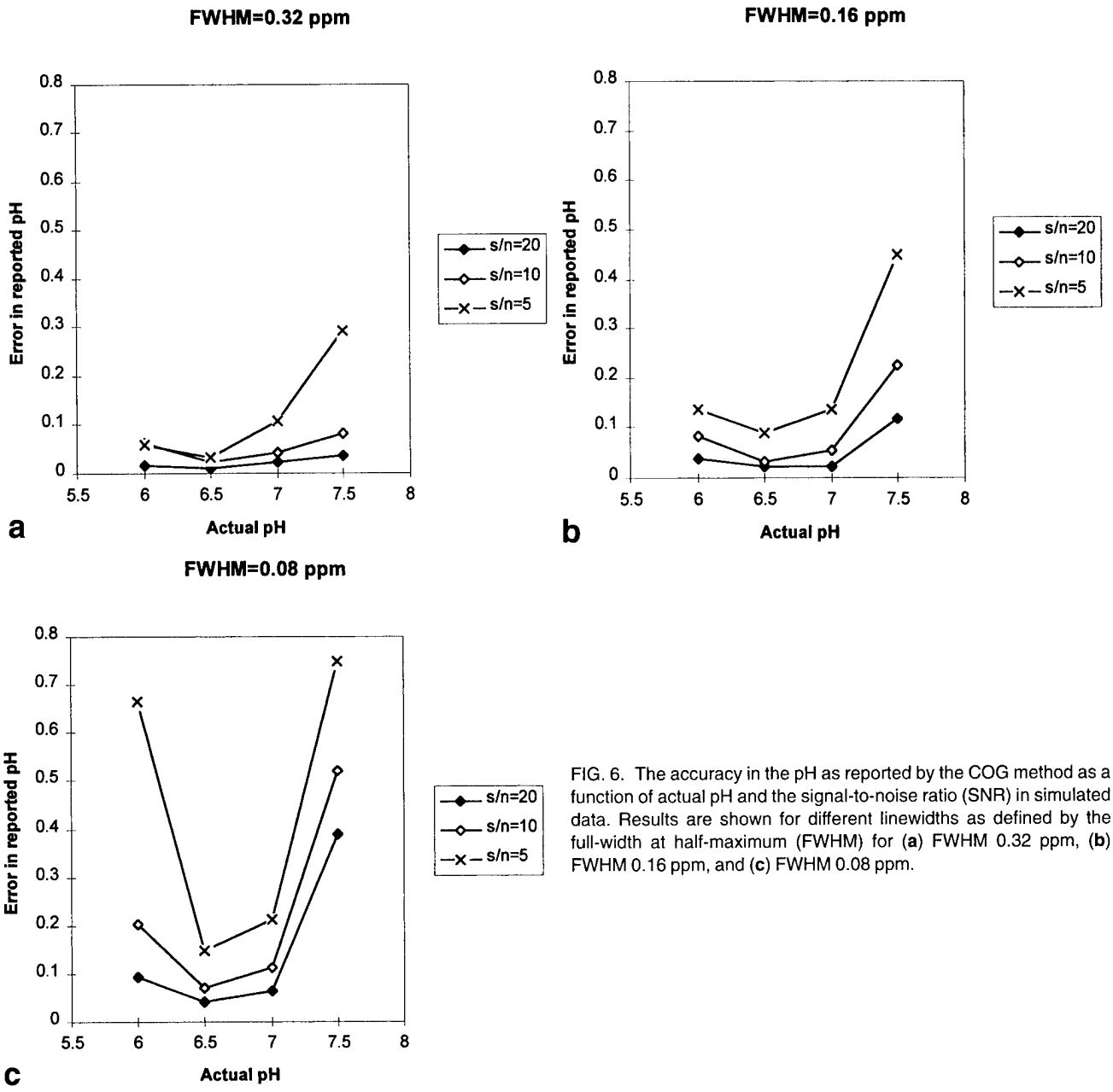


FIG. 6. The accuracy in the pH as reported by the COG method as a function of actual pH and the signal-to-noise ratio (SNR) in simulated data. Results are shown for different linewidths as defined by the full-width at half-maximum (FWHM) for (**a**) FWHM 0.32 ppm, (**b**) FWHM 0.16 ppm, and (**c**) FWHM 0.08 ppm.

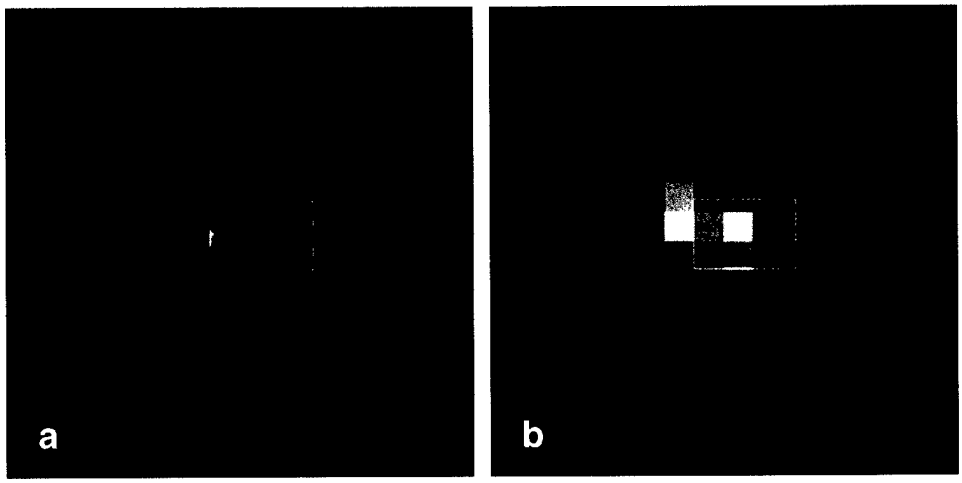


FIG. 7. **a:** High-resolution (128 × 128 pixels) subtraction image of Gd-DTPA uptake in an MCF-7 tumor in vivo. **b:** The same image, rebinned to 16 × 16 pixels. The resulting pixel size (1.56 $mm^2$) approximates the 2 $mm^2$ spatial resolution used when acquiring IEPA MRSI data. In both images, the white box indicates the location of the tumor. The six pixels entirely within the tumor in b were used to calculate concentration differences between adjacent voxels.

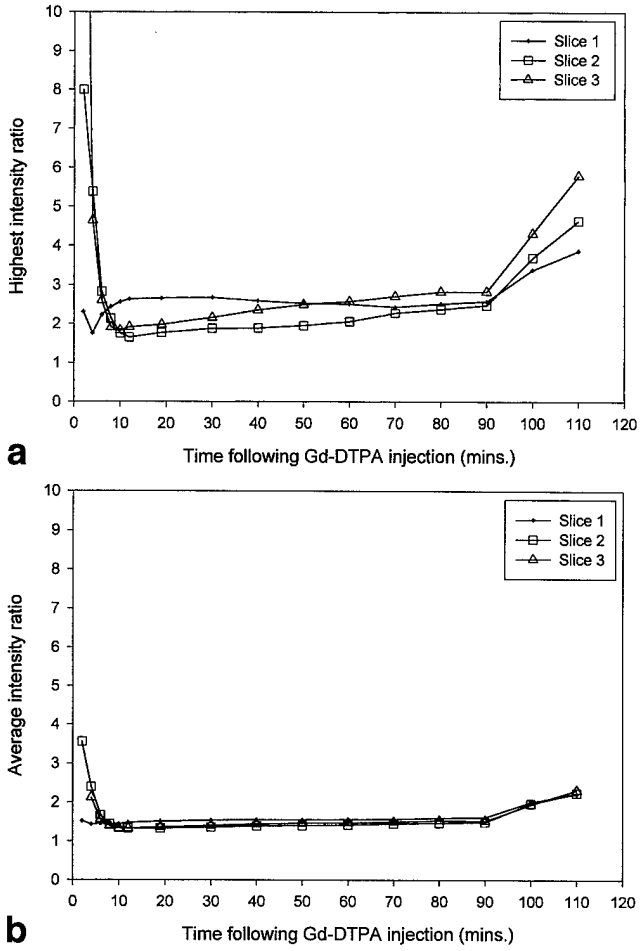


FIG. 8. The nearest neighbor highest (**a**) and average (**b**) intensity ratio as a function of time following Gd-DTPA injection in MCF-7 tumors.

IEPA intensity ratios between adjacent voxels, a simulated IEPA distribution was set up over the previously mentioned grid of 8 × 8 voxels.

### *Quantifying $pH_e$ Inhomogeneity*

Information on the maximum spatial $pH_e$ gradient expected for adjacent voxels in the MRSI data was obtained through the work of Helmlinger et al (27), who reported a 0.7 unit $pH_e$ difference between well-oxygenated (near the blood vessel) and nonoxygenated regions (away from the blood vessel) in tumors, over a distance of 400 μm. This is in good agreement with work by Raghunand et al (13), who found that 85% of tumor $pH_e$ values are within ±0.4 pH units of the mean $pH_e$. To observe a pH difference of 0.7 pH units between adjacent 16 $mm^3$ voxels in our MRSI data, it is necessary to have a fully oxygenated voxel (i.e., full of capillaries) immediately next to nonoxygenated voxels (i.e., no capillaries). It would be possible to find completely nonoxygenated voxels in vivo, for example, in necrotic areas. However, since in general tumor cells divide faster than their surrounding vasculature, the presence of a voxel consisting entirely of capillaries would be less likely. Therefore, we have chosen to work with the average $pH_e$ range observed by both Helmlinger et al and Raghunand et al (i.e., 0.4 pH unit), as the maximum pH gradient between adjacent voxels.

### *Combined Effect of IEPA Concentration and $pH_e$ Inhomogeneity on COG Precision*

The maximum pH differences, with signal intensity ratios of either 1:3.0 or 1:1.5, were inserted into the simulation program. The reported pH for the center and surrounding voxels were compared with the actual values. The difference between the actual pH value and the pH value reported by the simulation program expresses the error due to the voxel bleed artifact, as shown in Fig. 9. As expected, when the center voxel is surrounded by more acidic voxels, the reported pH for the center voxel is underestimated and vice versa.

The error in the reported pH for the center voxel over the physiological pH range (6.8–7.6 pH units) is less than 0.15 pH units for a *maximum* intensity ratio of 1:3.0, and less than 0.10 pH units for an *average* intensity ratio of 1:1.5, as shown in Fig. 9. This is an encouraging result for the

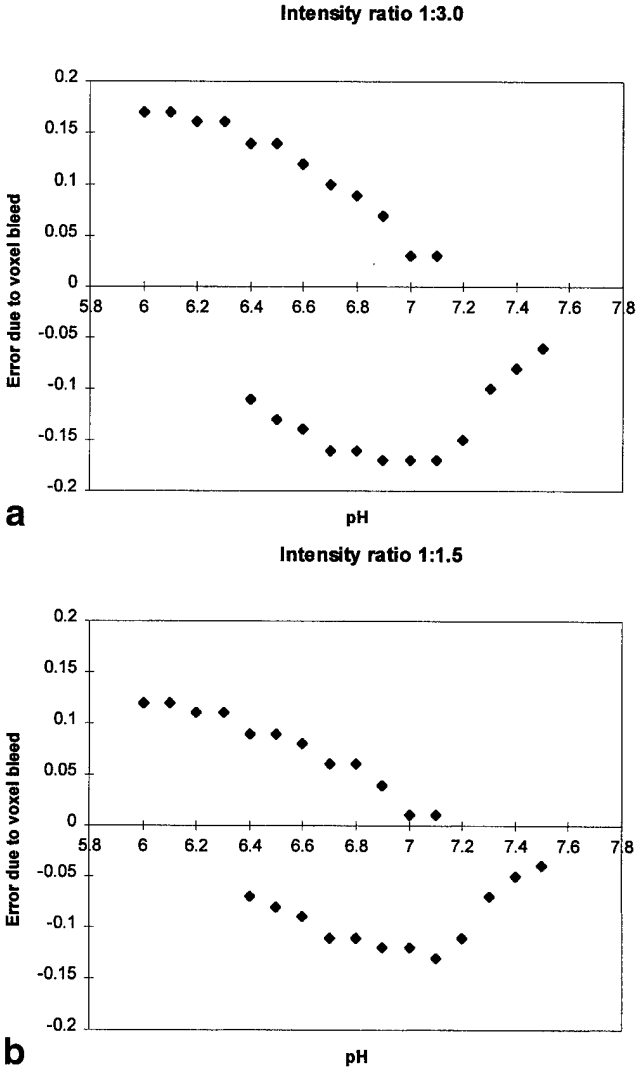


FIG. 9. The error due to the voxel bleed artifact for the center voxel as a function of pH and signal intensity ratio for (**a**) a signal intensity ratio of 1:3.0 and (**b**) 1:1.5.

precision of the proposed technique. Additionally, it must be remembered that these are worst-case scenarios. In practice, it is likely that the pH difference between adjacent voxels is less than 0.4 pH units, thus further reducing the error due to the voxel bleed artifact.

## CONCLUSIONS AND FUTURE DIRECTIONS

Using phantom and in vivo data, we have demonstrated the feasibility of imaging extracellular pH using $^1$H MRSI. The possible sources of error associated with the technique were analyzed in detail. It was found that the COG method leads to an error of <0.1 pH units for broader lines and reasonable SNR. For narrower lines, the poor spectral resolution increasingly reduces this accuracy. From simulations, it was found that artifacts due to voxel bleed in MRSI will introduce a maximum error of 0.1 pH units in the reported pH values. Finally, it was observed that the $T_2$ of the proposed $pH_e$ indicator is pH dependent. This dependence, its cause, and the effect on reported pH values are currently under investigation.

## ACKNOWLEDGMENTS

The authors thank D.C. Shungu, V.P. Chacko, and B. Baggett for their invaluable help with this work. Support from the US Army Breast Cancer Initiative DAMD17–94-J-4368 (to R.J.G.) and DAMD17–96–1-6131 (to Z.M.B.) and grants PB93–0037 (to P.B.) and PB94–011 (to S.C.) is gratefully acknowledged.

## REFERENCES

1. Warburg O. On the metabolism of tumors. Cambridge: Cambridge University Press; 1930.
2. Wike-Hooley JL, Haveman J, Reinhold HS. The relevance of tumor pH to the treatment of malignant disease. Radiother Oncol 1984;2:343–366.
3. Gillies RJ, Liu Z, Bhujwalla Z. $^{31}$P MRS measurement of extracellular pH of tumor using 3-aminopropylphosphonate. Am J Physiol 1994;267: C195–C203.
4. Negendank W. Studies of human tumors by MRS: a review. NMR Biomed 1992;5:303–324.
5. Griffiths JR. Are cancer cells acidic? Br J Cancer 1991;64:425–427.
6. Raghunand N, He X, van Sluis R, Bhujwalla ZM, Gillies RJ. Plasmalemmal pH gradients in drug-sensitive and drug-resistant MCF-7 human breast carcinoma tumors measured by $^{31}$P MRS. In: Proceedings of the ISMRM 6th Annual Meeting, Sydney, 1998. p 1644.
7. LeBoeuf RA, Kerckaert GA, Aardema MJ, Gibson DP. Multistage neoplastic transformation of Syrian hamster embryo cells cultured at pH 6.70. Cancer Res 1990;50:3722–3729.
8. Morita T, Takeda K, Okumura K. Evaluation of clastogenicity of formic acid, acetic acid and lactic acid on cultured mammalian cells. Mutat Res 1990;240:195–202.
9. Morita T, Nagaki T, Fukuda I, Okumura K. Clastogenicity of low pH to various cultured mammalian cells. Mutat Res 1992;268:297–305.
10. Martínez-Zaguilán R, Seftor EA, Seftor REB, Chu Y-W, Gillies RJ, Hendrix MJC. Acidic pH enhances the invasive behavior of human melanoma cells. Clin Exp Metast 1996;14:176–186.
11. Schlappack OK, Zimmermann A, Hill RP. Glucose starvation and acidosis: effect on experimental metastatic potential, DNA content and MTX resistance of murine tumour cells. Br J Cancer 1991;64:663–670.
12. Gerweck LE, Seetharaman K. Cellular pH gradient in tumor versus normal tissue: potential exploitation for the treatment of cancer. Cancer Res 1996;56:1194–1198.
13. Raghunand N, Altbach MI, Bhujwalla ZM, Gillies RJ. Extracellular pH excursions in drug-sensitive and drug-resistant MCF-7 human breast carcinoma cells: a $^{31}$P MRS study. In: Proceedings of the ISMRM 5th Annual Meeting, Vancouver, 1997. p 1096.
14. Brown FF, Campbell ID, Kuchel PW, Rabenstein DL. Human erythrocyte metabolism studies by $^1$H spin echo NMR. FEBS Lett 1977;82:12–16.
15. Pan JW, Hamm JR, Rothman DL, Shulman RG. Intracellular pH in human skeletal muscle by $^1$H NMR. Proc Natl Acad Sci USA 1998;85: 7836–7839.
16. Rabenstein DL, Isab AA. Determination of the intracellular pH of intact erythrocytes by 1H NMR spectroscopy. Anal Biochem 1992;121:423–432.
17. Gil S, Zaderenzo P, Cruz F, Cerdán S, Ballesteros P. Imidazol-1-ylalkanoic acids as extrinsic 1H NMR probes for the determination of intracellular pH, extracellular pH and cell volume. Bioorg Med Chem 1994;2:305–314.
18. Gillies RJ, Raghunand N, Bhujwalla ZM, Ballesteros P, Alvarez J, Cerdán S. Measurement of extracellular pH in tumors by $^1$H MRSI. In: Proceedings of the Proc. ISMRM, 5th Annual Meeting, Vancouver, 1997. p 1099.
19. van Sluis R, Bhujwalla ZM, Raghunand N, Ballesteros P, Alvarez J, Cerdán S, Gillies RJ. Imaging of extracellular pH using $^1$H MRSI. In: Proceedings of the ISMRM 6th Annual Meeting, Sydney, 1998. p 1642.
20. Shungu DC, Glickson JD. Band-selective spin echoes for in vivo localized $^1$H NMR spectroscopy. Magn Reson Med 1994;32:277–284.
21. Brown TR. Practical applications of chemical shift imaging. NMR Biomed 1992;5:238–243.
22. Wüthrich K, Wagner G. Nuclear magnetic resonance of labile protons in the basic pancreatic trypsin inhibitor. J Mol Biol 1979;130:1–18.
23. Madden A, Leach MO, Sharp JC, Collins DJ, Easton D. A quantitative analysis of the accuracy of in vivo pH measurements with $^{31}$P NMR spectroscopy: assessment of pH measurement methodology. NMR Biomed 1991;4:1–11.
24. Graham RA, Taylor AH, Brown TR. A method for calculating the distribution of pH in tissues and a new source of pH error from the $^{31}$P NMR spectrum. Am J Physiol 1994;266:R638–R645.
25. Wang Z, Bolinger L, Subramanian VH, Leigh JS. Errors of Fourier chemical shift imaging and their corrections. J Magn Reson 1991;92: 64–72.
26. Roberts TPL. Physiologic measurements by contrast-enhanced MR imaging: expectations and limitations. J Magn Reson Imaging 1997;7: 82–90.
27. Helmlinger G, Yuan F, Delian M, Jain RK. Interstitial pH and $pO_2$ gradients in solid tumors in vivo: high-resolution measurements reveal a lack of correlation. Nature Med 1997;3:177–182.

Neoplasia • Vol. 3, No. 2, 2001, pp. 143–153 

www.nature.com/neo

# Vascular Differences Detected by MRI for Metastatic Versus Nonmetastatic Breast and Prostate Cancer Xenografts[1]

*Zaver M. Bhujwalla, Dmitri Artemov, Kshama Natarajan, Ellen Ackerstaff and Meiyappan Solaiyappan*

MR Oncology Section, Division of MR Research, Department of Radiology, The Johns Hopkins University School of Medicine, Baltimore, MD 21205

**Abstract**

**Several studies have linked vascular density, identified in histologic sections, to "metastatic risk." Functional information of the vasculature, not readily available from histologic sections, can be obtained with contrast-enhanced MRI to exploit for therapy or metastasis prevention. Our aims were to determine if human breast and prostate cancer xenografts preselected for differences in invasive and metastatic characteristics established correspondingly different vascular volume and permeability, quantified here with noninvasive MRI of the intravascular contrast agent albumin–GdDTPA. Tumor vascular volume and permeability of human breast and prostate cancer xenografts were characterized using MRI. Parallel studies confirmed the invasive behavior of these cell lines. Vascular endothelial growth factor (VEGF) expression in the cell lines was measured using ELISA and Western blots. Metastasis to the lungs was evaluated with spontaneous as well as experimental assay. Metastatic tumors formed vasculature with significantly higher permeability or vascular volume ($P<.05$, two-sided unpaired $t$ test). The permeability profile matched VEGF expression. Within tumors, regions of high vascular volume usually exhibited low permeability whereas regions of low vascular volume exhibited high permeability. We observed that although invasion was necessary, without adequate vascularization it was not sufficient for metastasis to occur.** *Neoplasia* (2001) **3,** 143–153.

**Keywords:** vascular MRI, metastasis, invasion, breast and prostate cancer xenografts.

## Introduction

The relationship between tumor vascularization and metastasis has attracted significant interest since the initial observation in melanoma by Srivastava et al. [1] and in breast cancer by Weidner et al. [2] that the vascular density measured in histologic sections of human breast cancer was predictive of the disposition of the patient to present with metastases. This relationship has been evaluated for different types of cancers using different immunohistochemical markers such as Factor VIII, vascular endothelial growth factor (VEGF) expression, and CD34 [3]. Among the various types of cancers studied, the relationship appears to be most evident for melanoma [1], breast [2,4], and prostate [5,6] cancer although results to the contrary have also been reported in colorectal cancer [3,7].

Noninvasive high-resolution MRI of macromolecular contrast agents provides a unique means of evaluating tumor vascular volume and permeability of human tumor models transplanted in immune suppressed mice [8–10]. Because vascular volume and permeability is obtained from the same spatial regions it is also possible to investigate the spatial relationship between these two parameters. Our interest in using noninvasive MRI to investigate the relationship between vascular characteristics and metastasis was to determine if macromolecular contrast-enhanced MRI could detect significant differences in vascular characteristics of human breast and prostate cancer lines preselected for differences in metastatic outcomes. If established, such an observation would allow the development of an MRI test to provide an additional prognostic marker to evaluate breast and prostate lesions. This is of particular importance for prostate cancer because leading health centers are investigating "watchful waiting" as an option for prostate cancer management. Because histologic sections cannot provide functional information, our aim was also to relate the functional MRI data to histologic findings to further understand the relationship between vascularization and metastasis. For our studies we selected three well-established human breast cancer lines (MCF-7, MDA-MB-231, MDA-MB-435), one rat (MatLyLu), and two human (DU-145, PC-3) prostate cancer cell lines. Additional studies were performed to determine VEGF secreted by cells for the six tumor models examined here. Because changes in phenotype may occur for the same cells in different laboratories, we also evaluated the invasiveness of the cell lines using an MR-compatible invasion assay we have recently developed [11]. Both spontaneous and experimental metastasis assays were also performed for the six tumor models.

Address all correspondence to: Dr. Zaver M. Bhujwalla, PhD, MR Oncology Section, Division of MR Research, Department of Radiology, The Johns Hopkins University School of Medicine, Baltimore, MD 21205. E-mail: zaver@mri.jhu.edu

[1]This work was supported by USAMRMC DAMD17-96-1-6131, a grant from the Susan G. Komen Foundation, and by NCI R01 CA73850 and NCI R01 CA82337.
Received 6 November 2000; Accepted 1 December 2000.

## Methods

*Tumor Models and Inoculations*

Human breast cancer cells were inoculated in the left upper thoracic mammary fat pad (mfp) of female severe combined immune deficient (SCID) mice. Prostate cancer cells were inoculated subcutaneously in the right flank of male SCID mice, because the surgical procedure for orthotopic implantation into the prostate would have introduced additional complications such as the proximity of a wound near the inoculum [12]. Tumor cells were inoculated in a volume of 0.05 ml Hanks balanced salt solution (HBSS, Sigma, St. Louis, MO) at a concentration of $10^6$ cells/0.05 ml. Cells in culture were maintained according to the protocols and growth media described in Refs. [11,13] and had similar doubling times of the order of 17 to 24 h. The experimental protocol was approved by the Institutional Animal Care and Use Committee. All three breast cancer lines were originally derived from pleural effusions of patients with breast cancer. Because the growth of the MCF-7 line is estrogen dependent, a 17$\beta$-estradiol pellet (0.72 mg/pellet, 60-day release, Innovative Research of American, Sarasota, FL) was inserted in the right flank using a trochar needle, 1 week before inoculation of the cells. All three prostate cancer lines used were androgen independent. The DU-145 and PC-3 human prostate cancer lines were isolated from metastasis to the brain and bone. The MatLyLu rat prostate cancer cell line was originally cloned from the Dunning rat prostate cancer line and is highly invasive and metastatic for the lymph nodes and lungs [14].

*Kinetics of Albumin–GdDTPA in Blood*

Albumin–GdDTPA (gadolinium diethylenetriamine pentaacetic acid, molecular weight approximately 90,000) was synthesized in our laboratory based on the procedure originally described by Ogan et al. [15]. The albumin–GdDTPA complex was dialyzed thrice against a citrate buffer and thrice against deionized water to dialyze any free GdDTPA in the preparation. Each dialysis was performed overnight in a cold room maintained at 4°C using a dialysis membrane of MW 12 to 14 kDa (SPECTRA/POR 4, Cole Parmer, Niles, IL). A separate set of experiments were performed to establish the kinetics of albumin–GdDTPA in blood. In these experiments, mice were anaesthetized and both the tail vein and the common carotid artery were cannulated. Blood samples of 20 $\mu$l were obtained from the carotid before and up to 60 minutes after intravenous administration of albumin–GdDTPA (0.2 ml of 60 mg/ml albumin–GdDTPA in saline) delivered through the tail vein. Albumin–GdDTPA concentration in blood was obtained from the $T_1$ relaxation times of blood samples measured at 4.7 T using a special microcoil designed by V. P. Chacko (JHU), with high signal-to-noise ratio. Although in this study animals were sacrificed at the end of each imaging experiment to obtain tumors for sectioning, and therefore 0.5 ml of blood was withdrawn from the inferior vena cava, the availability of the microcoil now allows us to perform repeated measurements of vascular volume and permeability on the same animal over a period of time, because blood $T_1$ can be determined from a couple of drops of blood obtained from the tail vein. A comparison of $T_1$ values from such a sample with $T_1$ obtained 3 minutes later from 0.5 ml of blood from the vena cava provided almost identical values (data not shown).

*Multislice MR Imaging Studies*

Imaging studies were performed on a GE CSI 4.7T instrument equipped with shielded gradients. Images were obtained with a 1-cm solenoid coil placed around the tumor. A small capillary filled with water doped with GdDTPA was attached to the side of the coil to (a) serve as an intensity reference, (b) ensure that spatial registration was identical for all images and, (c) reference histologic sections with images. The tail vein of the animal was catheterized before it was placed in the magnet; a home-built catheter system using a small T-junction (T-Connectors, 1/16 in., Cole-Parmer) was devised to minimize the dead volume, which was less than 0.04 ml. Animal body temperature was maintained at 37° C by heat generated from a pad circulating with warm water.

Multislice relaxation rates ($T_1^{-1}$) were obtained by a saturation recovery method combined with fast $T_1$ SNAPSHOT-FLASH imaging (flip angle of 10°, echo time of 2 msec). Images of four to eight slices (slice thickness of 1 mm) acquired with an in-plane spatial resolution of 0.125 mm (128×128 matrix, 16-mm field of view, NS=8) were obtained for three relaxation delays (100 msec, 500 msec, and 1 second) for each of the slices. Thus $T_1$ maps from eight slices could be acquired within 7 minutes. An $M_o$ map with a recovery delay of 7 seconds was acquired once at the beginning of the experiment. Images were obtained before intravenous administration of 0.2 ml of 60 mg/ml albumin–GdDTPA in saline (dose of 500 mg/kg) and repeated, starting 3 minutes after the injection, up to 32 minutes. Relaxation maps were reconstructed from data sets for three different relaxation times and the $M_o$ data set on a pixel by pixel basis. At the end of each imaging study, the animal was sacrificed, 0.5 ml of blood was withdrawn from the inferior vena cava, and tumors were marked for referencing to the MRI images, excised, and fixed in 10% buffered formalin for sectioning and staining. The lungs of the animal were also excised and fixed in 10% buffered formalin for sectioning and staining.

Vascular volume and permeability–surface area product (PSP) maps were generated from the ratio of $\Delta(1/T_1)$ value in the tumor image to $\Delta(1/T_1)$ of blood versus time. The slope of the $\Delta(1/T_1)$ ratio versus time in each pixel was used to compute PSP, whereas the intercept of the line at zero time was used to compute vascular volume [16–18]. Thus, vascular volumes were corrected for permeability of the vessels. 3D reconstruction of MRI data was performed using our custom-built volumetric visualization software. Adjustment of transfer functions that control the voxel transparency and intensity characteristics of various structures of interest can be performed with the software to

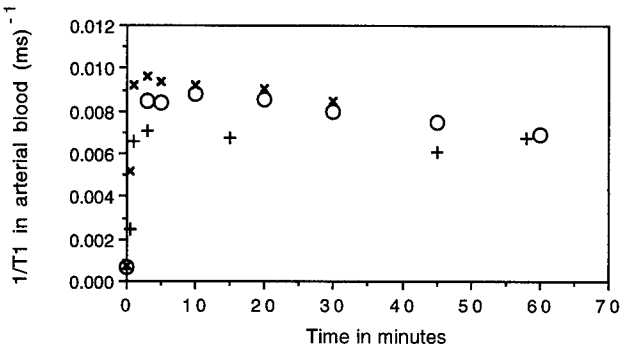


**Figure 1.** *Kinetics of albumin–GdDTPA in mouse blood for normal mouse (+), mouse with MDA-MB-231 tumor (○) and mouse with DU-145 tumor (×). Blood levels of albumin–GdDTPA remain constant up to 30 minutes and longer.*

delineate structures of interest from surrounding structures. The visualization software is developed around Silicon Graphics workstation systems, taking full advantage of the hardware accelerated graphics capabilities such as 2- and 3D textures to provide interactive rendering results. Furthermore, by displaying the image for each parameter through a unique color channel, e.g., vascular volume as red and vascular permeability as green, it is feasible to visually inspect the relationship between two parameters by fusing the two color maps.

### *Analysis of MRI Tumor Vascular Characteristics*

In addition to deriving average vascular volume and permeability over the entire tumor, we separately analyzed regions of high vascular volume or high vascular permeability

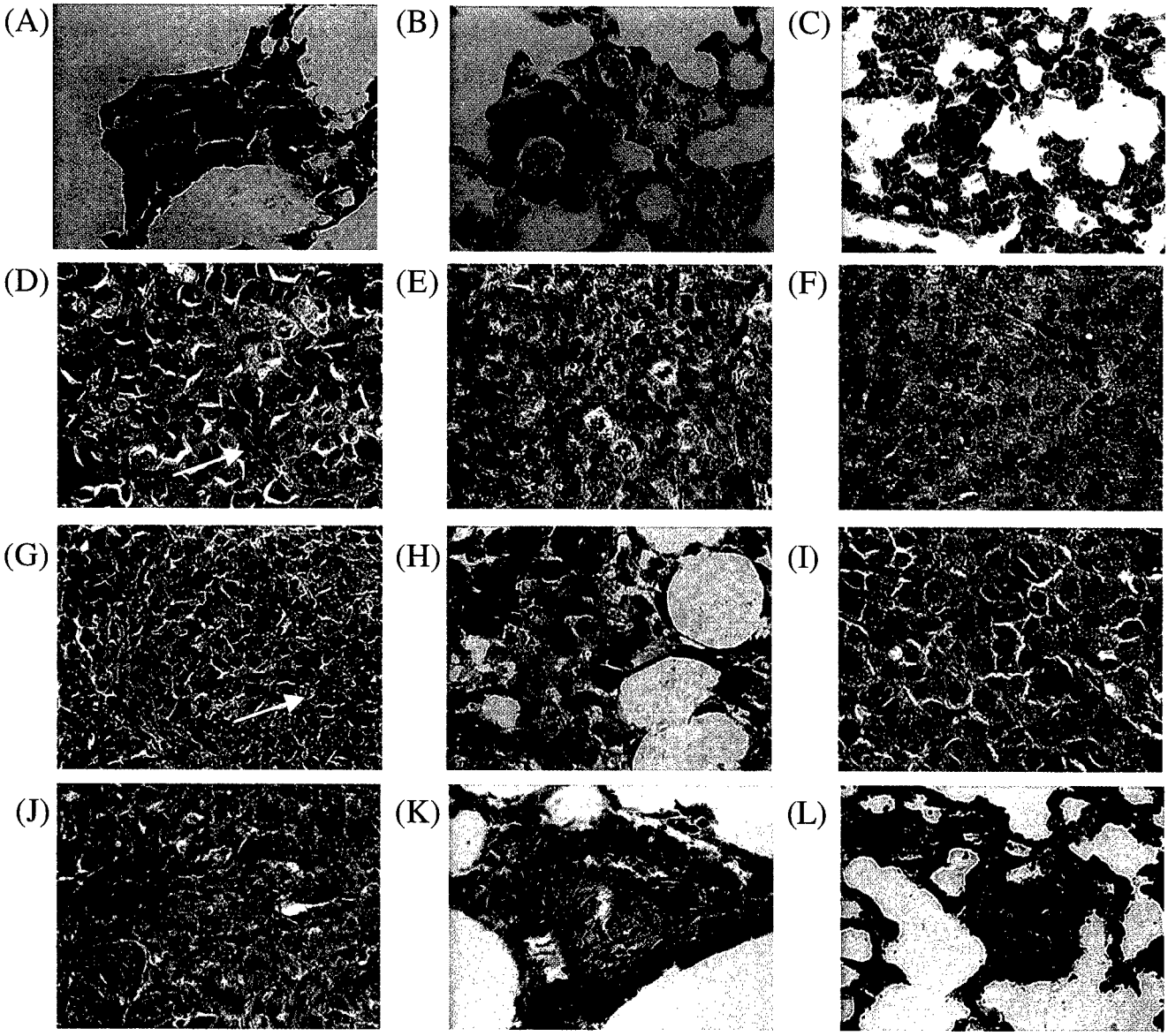


**Figure 2.** *High-power micrographs (×400) of 5-μm-thick histologic sections stained with hematoxylin and eosin. Sections D, E, F, G, H, and I are primary tumor sections obtained from MDA-MB-435, MDA-MB-231, MCF-7, MatLyLu, PC-3, and DU-145 tumors. Arrows indicate tumor vessels. Sections A, B, C, J, K, and L are lung sections demonstrating metastasis of MDA-MB-435 (spontaneous metastasis), MDA-MB-231 (spontaneous metastasis), MCF-7 (experimental metastasis), MatLyLu (spontaneous metastasis), PC-3 (experimental metastasis), and DU-145 (experimental metastasis) cancer cells.*

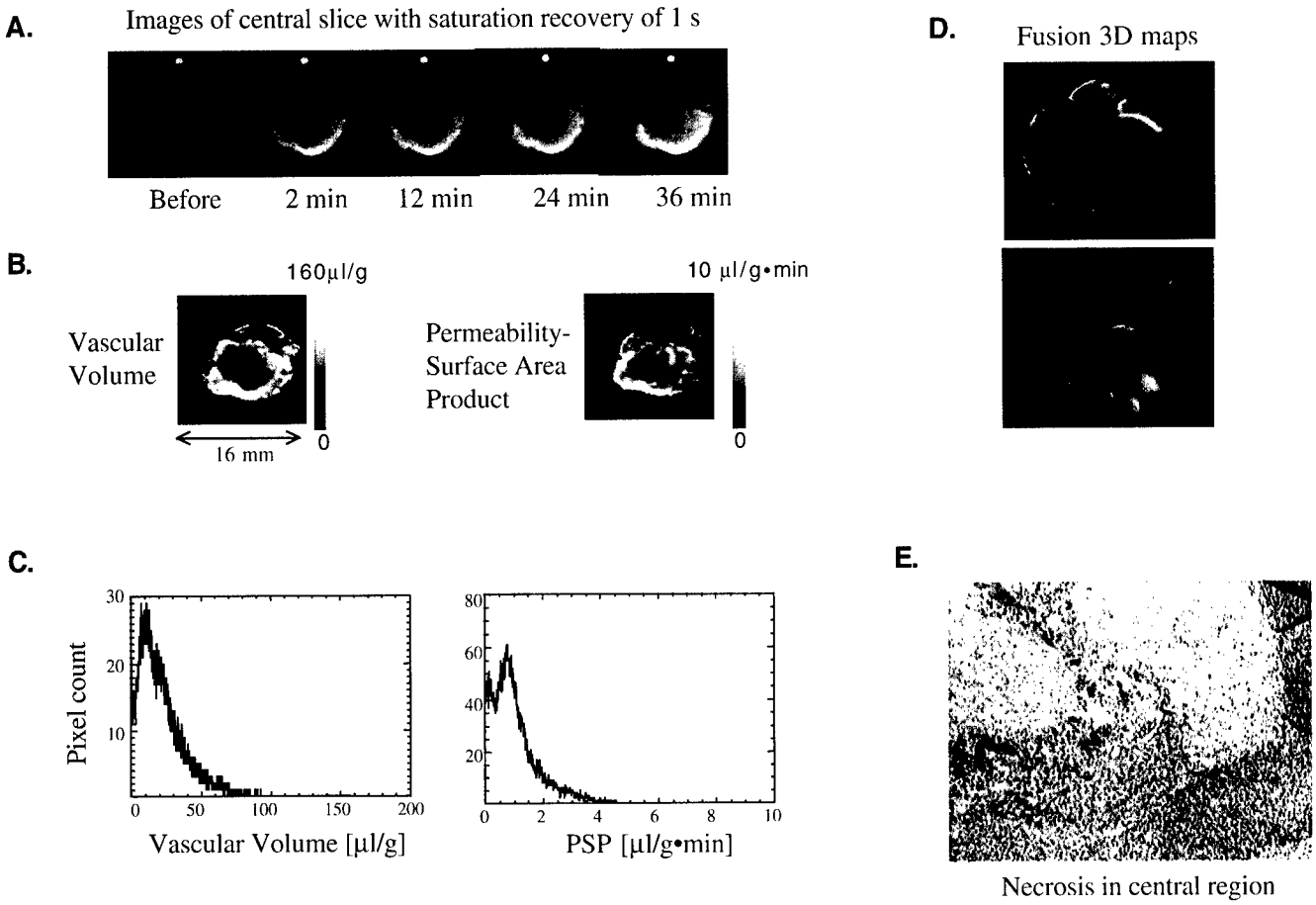


**Figure 3.** *(A) Raw images from a central slice of a MatLyLu tumor (180 mm$^3$) presented to show the actual distribution of the contrast agent; the corresponding maps of vascular volume and permeability-surface area product (PSP) are shown in (B). The frequency distribution of vascular volume and PSP for this tumor are shown in (C). 3D reconstructed fusion maps of vascular volume (red channel) and permeability (green channel) obtained from multislice data for this tumor are displayed in (D). The 3D fusion images show triplanar and volume rendered views of the fused maps. A histologic section stained with hematoxylin and eosin of the central slice of this tumor is shown in (E). Hematoxylin and eosin staining revealed necrosis and edema in the central region of this tumor.*

using a selected threshold for the highest 10% or 25% of the distribution. One reason for this approach is that the original histologic observations relating vessel density to disposition to metastasize was obtained by counting the number of vessels in the regions of high vascular density [2]. The other reason was to investigate the relationship between vascular volume and vascular permeability in regions of high vascular volume and regions of high vascular permeability. For our analyses, we therefore determined mean values of vascular volume in regions of high vascular volume as well as high permeability. Corresponding analyses were performed for permeability. In addition, the percent fractional tumor volume containing high vascular volume or high vascular permeability was also determined. Our rationale for picking two thresholds — "highest"(10%) and "high" (25%) was to ensure that we did not miss trends in the data. However, as shown subsequently, analyses of the "highest" and "high" regions provided concordant results. 3D volume data were processed with an operator independent computer program which enabled selection, mapping and display of the regions within a specified range of parameter values. For example, the vascular volume defined for the highest 10% (or 25%) values of the histogram was the median of vascular volume values for voxels within the first 10% (or 25%) of the area under the frequency distribution curve. The latter was determined by integrating the histogram, starting at the maximum value of vascular volume, with a cut off at 10% (or 25%) of the total area under the curve (see Figure 3*C*). The corresponding volume fractions of the regions were determined from the number of voxels with vascular volumes in the range defined from the histogram analysis of the data. The routine is written with IDL programming language (Research Systems, Boulder, CO) and is compatible with most operation systems.

### *Statistical Methods*

Four to eight tumors were studied for each group. All tumors were volume matched with volumes of 200 to 300 mm$^3$. Statistical analyses were performed using Statview II version 1.04, 1991 (Abacus Concepts, Berkeley, CA). Statistically significant differences were established using a two-sided unpaired *t* test for 95% confidence levels or higher ($P<.05$).

**Table 1.** (A) Vascular Volume and (B) Permeability Data Summarized for the Six Tumor Models.

(A) Vascular Volume Data Summarized for the Six Tumor Models

| Cancer Model | | Highest 10% Values of Histogram ("Highest") | | Highest 25% Values of Histogram ("High") | | All Nonzero Values of Histogram | |
|---|---|---|---|---|---|---|---|
| Breast | Tumor Volume ($mm^3$) | % Volume | Mean Value ($\mu l/g$) | % Volume | Mean Value ($\mu l/g$) | % Volume | Mean Value ($\mu l/g$) |
| MDA-MB-435 ($n$=8) | 212±31 | 8.2±0.4 | 67.7±12.4* | 20.4±0.9 | 45.6±7.0* | 81.3±3.6 | 18.4±3.1 |
| MDA-MB-231 ($n$=4) | 287±62 | 8.6±0.4 | 36.8±5.2 | 21.3±1.0 | 27.2±3.7 | 85.1±3.8 | 11.0±2.7 |
| MCF-7 ($n$=6) | 270±44 | 8.8±0.5 | 32.7±4.8 | 22.1±1.2 | 24.5±3.4 | 88.1±4.9 | 12.5±2.5 |
| Prostate | | % Volume | Value in $\mu l/g$ | % Volume | Value in $\mu l/g$ | % Volume | Value in $\mu l/g$ |
| MatLyLu ($n$=7) | 241±37 | 9.2±0.2† | 45.4±4.9‡ | 23±0.6† | 34.1±3.1†‡ | 91.3±2.4† | 19.0±1.8†‡ |
| PC-3 ($n$=5) | 310±60 | 6.5±0.6‡ | 36.4±3.4 | 16.2±1.5‡ | 21.7±1.2‡ | 63.8±6.2‡ | 6.7±0.8‡ |
| DU-145 ($n$=6) | 289±49 | 9.0±0.2 | 34.0±1.7 | 22.5±0.5 | 26.4+1.1 | 89.5±1.8 | 13.1±0.6 |

(B) Permeability Data Summarized for the Six Tumor Models

| Breast | | % Volume | Mean Value ($\mu l/g \cdot min$) | % Volume | Mean Value ($\mu l/g \cdot min$) | % Volume | Mean Value ($\mu l/g \cdot min$) |
|---|---|---|---|---|---|---|---|
| MDA-MB-435 ($n$=8) | 212±31 | 7.5±0.8 | 4.2±0.6* | 19.0±2.1 | 2.6±0.3* | 74.6±8.2 | 0.91±0.1* |
| MDA-MB-231 ($n$=4) | 287±62 | 9.2±0.2* | 3.5±1.1* | 23.0±0.5* | 2.4±0.7* | 91.3±1.8* | 1.24±0.4* |
| MCF-7 ($n$=6) | 270±44 | 7.6±0.6 | 1.5±0.3 | 19.0±1.5 | 1.1±0.2 | 75.4±6.1 | 0.5±0.1 |
| Prostate | | % Volume | Value in $\mu l/g \cdot min$ | % Volume | Value in $\mu l/g \cdot min$ | % Volume | Value in $\mu l/g \cdot min$ |
| MatLyLu ($n$=7) | 241±37 | 9.2±0.1†‡ | 2.9±0.5† | 23±0.4†‡ | 2.2±0.3† | 91.0±1.5†‡ | 1.1±0.1†‡ |
| PC-3 ($n$=5) | 310±60 | 3.7±1.1‡ | 1.3±0.2 | 9.3±2.8‡ | 0.8±0.15 | 36.6±11‡ | 0.26±0.06‡ |
| DU-145 ($n$=6) | 289±49 | 8.0±0.3 | 2.1±0.5 | 20.0±0.8 | 1.5±0.3 | 79.1±3.3 | 0.6±0.1 |

Nonzero values and the corresponding regions represent values with detectable levels of albumin–GdDTPA where the pattern of enhancement followed the algorithm used to derive vascular volume and permeability.
Values are mean±1 SEM; $n$ represents the number of tumors studied per model with at least four to six slices per tumor.
*Significantly different from MCF-7.
†Significantly different from PC-3.
‡Significantly different from DU-145.

*Histologic Analysis of Tumors*

Adjacent 5-$\mu$m-thick histologic sections obtained at 500-$\mu$m intervals through the tumor were stained with hematoxylin and eosin. Sections were digitized with a CCD camera (Sanyo, CA) attached to an optical microscope.

*Assays for Spontaneous and Experimental Metastasis*

Spontaneous metastasis from the cell lines was evaluated by determining the size and number of nodules in the lungs of animals sacrificed following MRI. Nodules were identified by microscopic examination of at least three 5-$\mu$m-thick lung sections stained with hematoxylin and eosin.

A separate assay was performed to evaluate experimental metastasis from these cell lines. For this assay, $2\times10^6$ cells were injected into the tail vein in a volume of 0.05 ml HBSS. Five animals were used for each cell line. The animals were sacrificed 2 weeks later and lung sections were examined as described before.

*Assays for VEGF Expression for Cells Used in the Study*

*Quantitation of VEGF in conditioned media of breast cancer* VEGF was measured by the Quantikine (R&D Systems, Minneapolis, MN) enzyme-linked immunosorbent assay. Cells ($10^6$) were seeded in a 100 mm petri dish overnight. Conditioned media from each of the cell lines were collected, centrifuged, and diluted as per manufacturer's instructions before performing the assay. The assay was repeated thrice using duplicate samples each time.

*VEGF expression in prostate cell lines* Because the MatLyLu cell line is not of human origin, a comparative study of VEGF expression for the three prostate cell lines was performed using Western blot analysis with a rabbit polyclonal antibody cross reactive for human, rat, and mouse VEGF (sc-507, Santa Cruz Biotechnology, Santa Cruz, CA). Serum-free RPMI-1640 was conditioned by subconfluent cultures of DU-145, PC-3, and MatLyLu for 18 hours. Ten milliliters of media was collected and concentrated to a final volume of 0.5 ml. For analysis of VEGF, the amount of conditioned medium from each cell line was normalized to cell number. The proteins in the conditioned media were resolved using both nonreducing and reducing 15% SDS-polyacrylamide gel electrophoresis [19]. The proteins were then transferred to a nitrocellulose membrane (Millipore, Bedford, MA) according to Towbin et al. [20]. After blocking in 5% skim milk, a rabbit polyclonal antibody (sc-507, Santa Cruz Biotechnology) was used to probe the membrane. The membrane was incubated with a horseradish peroxidase conjugated anti-rabbit antibody (from donkey, Amersham Pharmacia Biotech, Piscataway, NJ). The blots were developed using an enhanced chemilumi-

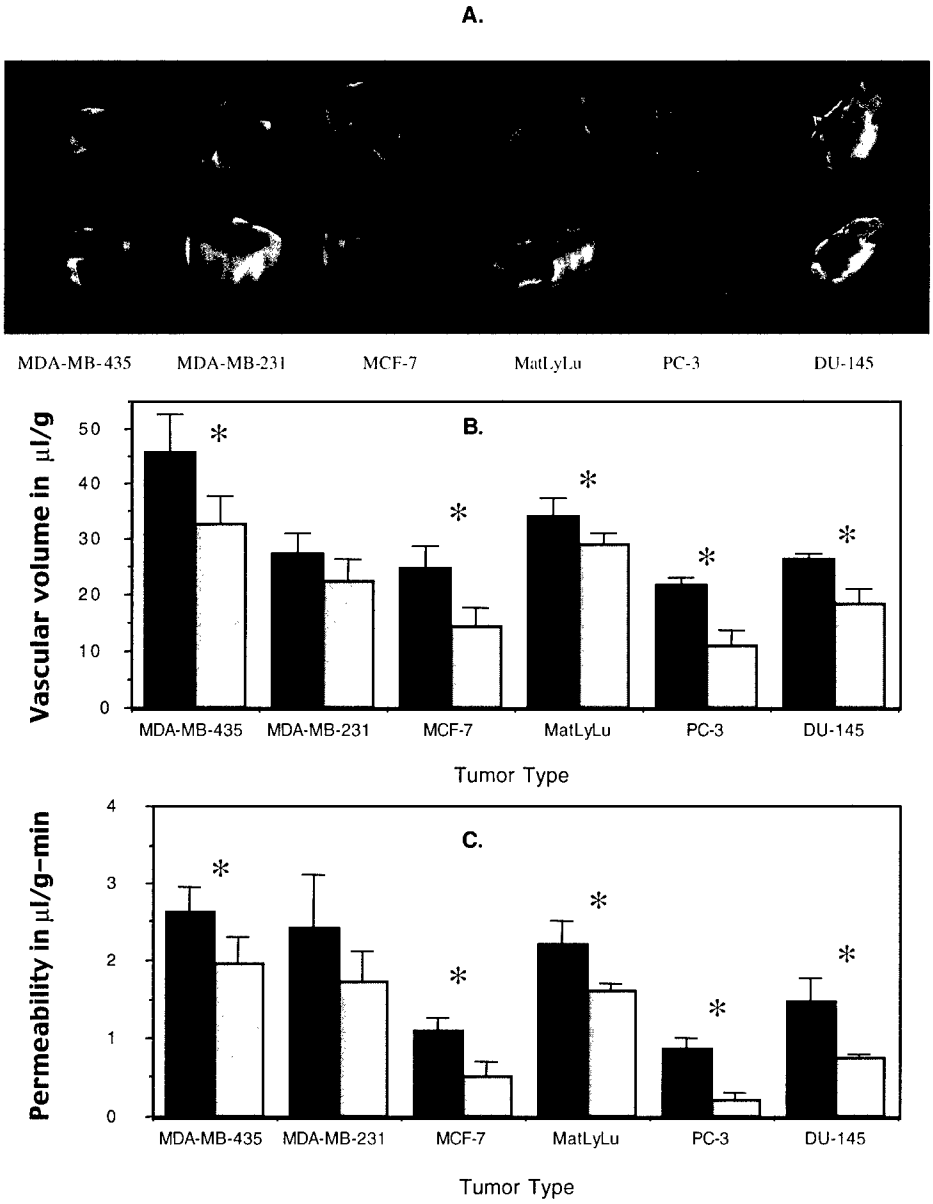


**Figure 4.** *Vascular volume and permeability "mismatch" characteristics of breast and prostate cancer tumor models. Representative red and green fusion maps for each of the tumor models are shown in (A); red corresponds to vascular volume, green to permeability. The mean value of the highest 25% values of vascular volume (■), and the mean vascular volumes spatially corresponding to the highest 25% values of permeability ( ) are shown in (B). The mean value of the highest 25% of permeability values (■), and the permeability spatially corresponding to the highest 25% values of vascular volume ( ) are shown in (C). A significant difference (P<.05) was observed for all the tumor models. The only exception to this was for the MDA-MB-231 tumor group.*

nescence (ECL-plus) system (Amersham Pharmacia Biotech) and exposed to Kodak biomax light film. Recombinant VEGF (Santa Cruz Biotechnology) was used as a standard. The intensity of VEGF staining, expressed in arbitrary units, between the prostate cell lines was quantified using NIH Image 1.62.

*MRI Invasion Assays to Determine Invasive Characteristics of the Cell Lines Used in This Study*

A comparison of the invasive behavior of the six cell lines used in this study was performed using our MR compatible invasion assay system. A detailed description of the assay can be found in Pilatus et al. [11]. Briefly, the assay system consists of a layer of Matrigel (Sigma) sandwiched between cells perfused under well-controlled conditions of temperature and oxygenation. The assay is stable over a period of at least 3 days and allows dynamic measurements of invasion over this time. In the study here, the assay was used to confirm previously established observations regarding the invasiveness of the six cell lines studied.

## Results

The kinetics of albumin–GdDTPA over a period of time for one normal and two tumor-bearing animals are shown in

**Table 2.** VEGF Secretion by Cell Lines.

| Tumor Model | VEGF* in pg/$10^6$ cells (in Culture) | Optical Density of Western Blots (in Arbitrary Units) |
|---|---|---|
| *Breast cancer* | | |
| MDA-MB-435 | 161.8±9.8 | not determined |
| MDA-MB-231 | 422.7±156 | not determined |
| MCF-7 | 66.5±5.0 | not determined |
| *Prostate cancer* | | |
| MatLyLu | not determined | 6198 |
| PC-3 | 65.0±5.6 | 1228 |
| DU-145 | 559.0±49.5 | 4961 |

Characterization of VEGF in cell lines for breast cancer xenografts using ELISA or Western blotting (prostate cells only). Values for the ELISA assay represent mean±1 SEM from a minimum of three independent sets of cell experiments per cell line plated at separate times.

Figure 1. These data confirm previous observations that the concentration of albumin–GdDTPA remains constant in the vasculature up to at least 30 minutes. Representative histologic sections stained with hematoxylin and eosin together with lung sections demonstrating metastatic nodules for the respective tumor are shown in (Figure 2, *A – L*). The arrows mark blood vessels in the histologic sections that typically consist of a single layer of endothelial cells. Representative images obtained before and at four time points after intravenous administration of albumin–GdDTPA from the central slice of a multislice data set of a MatLyLu tumor, and the corresponding maps of vascular volume and permeability are shown in Figure 3, *A* and *B*. The frequency distribution of vascular volume and permeability for this tumor are displayed in Figure 3*C*. Also shown in Figure 3, are two views of 3D reconstructed red and green color fusion images of vascular volume and permeability obtained for this tumor, where spatially coincident regions of red and green should appear as yellow (Figure 3*D*). However, these fusion images exhibit very little yellow and provide visual support for our observations that spatially there is little overlap between regions of high vascular volume and high permeability. A histologic section stained with hematoxylin and eosin, obtained from the central region of this tumor, is shown in Figure 3*E*, and demonstrates that the areas of necrosis are associated with low to nondetectable vascular volume.

Data of vascular volume and permeability for the six different tumor models are summarized in Table 1(A) and (B). Volumetric analyses were performed for the highest 10% ("highest") and 25% ("high") histogram values of vascular volume and permeability as well as mean vascular volume and permeability for size-matched tumors. For the panel of breast tumor models, MDA-MB-435 demonstrated significantly higher vascular volume compared to MDA-MB-231 and MCF-7 tumors for the highest 10% and 25% analyses. This difference disappeared when analyzing values averaged over the entire tumor. For the prostate tumor models, MatLyLu tumors demonstrated significantly higher vascular volume compared to PC-3 and DU-145 tumors. Interestingly MatLyLu tumors exhibited a higher volumetric fraction in some categories as well as actual value compared to PC-3 and DU-145 tumors.

Both MDA-MB-435 and MDA-MB-231 breast tumor models were significantly more permeable in terms of mean values than MCF-7 tumors for the highest 10% and 25% analyses. In addition, volumetrically, MDA-MB-231 tumors were also significantly more permeable than MCF-7 tumors. For the prostate tumor models, MatLyLu was significantly more permeable, in terms of volumetric fraction as well as values of permeability compared to PC-3 and DU-145 tumors.

Another facet of vasculature, revealed from these analyses, was that regions of high vascular volume were not spatially coincident with regions of high permeability. These results are summarized in Figure 4. Representative red and green fusion images for the six tumor models are displayed in Figure 4*A*. The mean value of the highest 25% values of vascular volume, and the mean vascular volumes spatially corresponding to the highest 25% values of permeability are shown in Figure 4*B*. The mean value of the highest 25% of permeability, and the permeability spatially corresponding to the highest 25% values of vascular volume are shown in Figure 4*C*. A significant difference was observed for all the tumor models. The only exception to this was observed for the MDA-MB-231 tumor group. When three larger tumors of approximately 500- to 600-$mm^3$ volume, which were excluded from the size-matched data, were added to the MDA-MB-231 group, the mismatch for the vascular volume was significant but there was still no significant difference in permeability.

**Table 3.** Assays of Spontaneous and Experimental Metastasis for the Tumor Models Used in the Study.

| Tumor Model | Spontaneous metastasis* (Number of Animals with Lung Nodules/Total Number of Animals Studied) | Experimental Metastasis† (Number of Animals with Lung Nodules/Total Number of Animals Studied) |
|---|---|---|
| *Breast cancer* | | |
| MDA-MB-435 | 4/9 | 6/7 |
| MDA-MB-231 | 2/7 | 4/6 |
| MCF-7 | 0/8 | 1/7 |
| *Prostate cancer* | | |
| MatLyLu | 2/8 | 4/5 |
| PC-3 | 0/6 | 2/5 |
| DU-145 | 0/6 | 2/5 |

Characterization of spontaneous and experimental metastasis for the six tumor models used in the study. For the spontaneous metastasis assay the average time from inoculation of cancer cells to excision of tumor and lungs was approximately 5 weeks for the human breast and prostate cancer model whereas MatLyLu tumors and lungs from MatLyLu tumor-bearing animals were excised at approximately 10 days. For experimental metastasis, lungs were excised 2 weeks after injecting $10^6$ cells into the tail vein.

*Average time from inoculation of cancer cells to excision of tumor and lungs was approximately 5 weeks for the breast and prostate cancer models with the exception of 10 days for the MatLyLu model.

†Lungs excised 2 weeks after injecting $10^6$ cells in the tail vein.

Analyses of VEGF expression for the cell lines are presented in Table 2. In the breast tumor models, MDA-MB-231 cells secreted the highest levels of VEGF, followed by MDA-MB-435 cells. MCF-7 cells secreted the lowest amount of VEGF. In the prostate tumor models, MatLyLu cells secreted the highest levels of VEGF followed by DU-145, whereas PC-3 cells secreted low levels of VEGF.

Results from the assays of spontaneous and experimental metastasis are presented in Table 3. MDA-MB-435, MDA-MB-231, and MatLyLu tumors exhibited spontaneous metastases in their respective groups. Neither MCF-7 nor PC-3 and DU-145 tumors resulted in the formation of spontaneous metastasis. Although all six cell lines were capable of forming experimental lung metastasis, again as for the spontaneous metastasis assay, MCF-7 cells induced the fewest lung nodules followed by PC-3 and DU-145 cells.

To maintain matched tumor sizes for MRI, the average time from inoculation of primary tumors to excision of lungs was only 10 days for the MatLyLu, whereas it was of the order of 5 weeks for the human tumor xenografts. Animals bearing MatLyLu tumors in excess of 20 days frequently showed almost complete lung destruction by tumor growth. Thus MatLyLu tumors appeared to be the most lethal of the six tumor models in terms of lung metastasis.

Although our cancer cell lines were preselected for literature-established differences in invasive characteristics, the phenotypic characteristics of cell lines can vary among laboratories. We therefore performed studies to confirm the invasion patterns of the six cell lines. These data are presented in Figure 5. From these images it is apparent that the Matrigel layer is significantly degraded by MDA-MB-435, MDA-MB-231, MatLyLu and PC-3 cells, whereas in comparison neither DU-145 nor MCF-7 cells degrade the Matrigel layer. The invasion index (mean±1 SEM), determined as previously described [11], for $n$ separate experiments at approximately 47 hours for the six cell lines was as follows: MatLyLu, 2.78±0.6 at 45.6 hours, $n$=6; PC-3, 2.57±0.3 at 49.3 hours, $n$=3; DU-145, 0.22±0.1 at 48 hours, $n$=5; MDA-MB-435, 2.65 at 49 hours, $n$=1; MDA-MB-231, 1.4±0.3 at 49.1 hours, $n$=2; MCF-7, 0.04±0.1 at 49.3 hours, $n$=2. These data demonstrate that, as anticipated, MDA-MB-435 and MDA-MB-231 cells were invasive for the breast tumor group, and MatLyLu and PC-3 cells were invasive for the prostate tumor group. Both DU-145 and MCF-7 exhibited hardly any invasiveness for this assay.

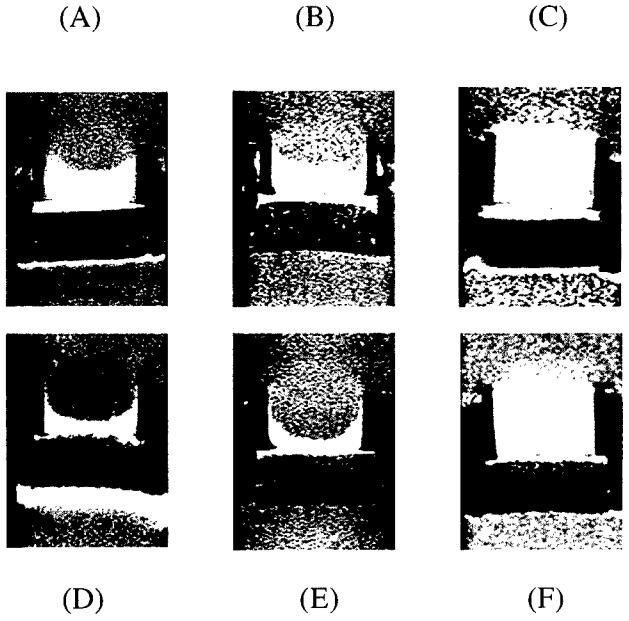


**Figure 5.** *(A–F): "Metabolic Boyden chamber assay" demonstrating differences in invasive characteristics of the breast (A–C) and prostate cancer (D–F) cell lines at approximately 47 hours. The $T_1$-weighted $^1H$ MR images show the bright Matrigel layer, which is significantly degraded by (A) MDA-MB-435, (B) MDA-MB-231, (D) MatLyLu, and (E) PC-3 cells, but not by the (C) MCF-7 or (F) DU-145 cells.*

## Discussion

*Vascular Volume and Permeability Measurements*

Accurate quantitation of vascular volume and vascular permeability using the algorithm described in this study requires the assumption that the concentration of contrast agent in the blood remains constant over the time period of MRI data acquisition that was validated here. The second assumption is that water in the vascular and extravascular compartments is in fast-exchange. Data from isolated rat heart perfusion studies suggest that water exchange may be intermediate in the heart [21,22]. However, rat cardiac vessels are well organized and consist of smooth muscle cell lining as well as a layer of basement membrane, which may result in some restriction of water exchanging across the two compartments [23]. In contrast, tumor neovasculature typically consists of a single layer of endothelial cells that facilitates fast exchange. Although the assumption of fast exchange may lead to an overestimation of vascular volume by about 10%, van Dijke et al. [24] have observed a significant correlation of the order of 0.9 between vessel density and MRI-derived values of vascular volume. Other studies have also shown that vascular volume estimates made with MRI, assuming fast exchange of water, were not different from estimates made by quantifying gadolinium with atomic emission spectrsocopy [25]. Because of the noninvasive nature of MRI the technique is able to measure vascular volume corrected for permeability. With invasive techniques some leakage of the tracer will occur in highly permeable regions as soon as the tracer enters the circulation, which might lead to overestimation of values [26]. However, although measurements of vascular volume and permeability for the six tumor models used here have not been performed previously using either MRI or other techniques, the values of vascular volume and permeability obtained here are in reasonably good agreement with values for other solid tumors cited in literature obtained with traditional invasive methods [16,26–28].

*Relationship between Vascular Volume and Permeability, and Necrosis*

A comparison of histologic sections obtained from the imaged tumors consistently showed that areas of cell death and necrosis were typically associated with low or non-detectable vascular volume, although areas of low vascular volume were not always associated with necrosis in histologic sections. Some vessels in large necrotic areas were found to contain clumps of tumor cells. These vessels were surrounded by dead cells suggesting this as one of the mechanisms for vascular collapse in highly metastatic tumors.

We also consistently observed that regions with high vascular volume were significantly less permeable when compared with regions of high permeability within the tumors. Similarly regions of high permeability consistently exhibited lower vascular volumes. One explanation for these observations is that regions of low vascular volume are the most hypoxic and therefore will express higher VEGF [29]. This is consistent with previous observations that more intense VEGF staining is detected around areas of necrosis [30–32] where the vessels are also most permeable [17,33]. Another possible mechanism for the "mismatch" is the occurrence of lymphatic drainage, which is currently under investigation in our laboratory. These findings do imply that in addition to previously proposed mechanisms of high tumor interstitial pressure [34,35], the delivery of macromolecular agents to the tumor interstitium may also be limited by the lower permeability of tumor vasculature in precisely those viable vascular areas where they necessarily should be delivered for effective treatment.

*Vascular Characteristics and VEGF Expression*

The patterns of VEGF expression obtained for the cell lines were in agreement with previously published values of VEGF levels for DU-145, PC-3 [36], MCF-7, and MDA-MB-231 cells [37]. Not surprisingly, VEGF expression, rather than vascular volume, by the cells was most closely related to the permeability measured in the solid tumors. Within the breast and prostate tumor groups, the two cell lines with the lowest expression of VEGF, MCF-7 and PC-3, displayed low permeability whereas the cell lines with the highest expression of VEGF, MDA-MB-231 and MatLyLu, exhibited the highest permeability. MDA-MB-231 was also the only tumor model where the permeability in regions of high vascular volume was not significantly different from regions of low vascular volume. It is apparent, however, that the actual levels of VEGF do not relate to permeability when both breast and prostate tumor models are combined for comparison. This may be related to differences in the site of inoculation, i.e., mammary fat pad versus flank or secretion of other factors that may inhibit or reduce the effect of VEGF [38,39].

*Invasion, Metastasis, and Vascularization*

These experiments were designed to determine the vascular characteristics of breast and prostate cancer models preselected for differences in invasive and metastatic behavior. To determine the ability of MRI to predict the disposition of the tumor to metastasize, the experimental protocol would have required excising the tumor and allowing the animal to survive surgery and determining the metastasis in lungs and other organs at time of natural death. To justify such a protocol an initial study was required to demonstrate significant differences between vascular characteristics of the selected tumor models as is demonstrated here. In the framework of this study we established that within the breast and prostate tumor model groups, tumor models that demonstrated the ability to establish pulmonary metastases to the lung from primary tumors consistently showed significantly higher permeability and, with the exception of MDA-MB-231, higher vascular volume. These data are consistent with results from Melnyk et al. [40], where inhibition of VEGF was found to prevent tumor dissemination by a mechanism that may be distinct from its effect on tumor growth.

The metastatic characteristics of the two breast lines MDA-MB-435 and MDA-MB-231 and the nonmetastatic characteristic of MCF-7 cells are consistent with previous observations [41–43]. Similarly for the prostate tumor models MatLyLu was clonally selected for invasion and metastasis [14] and in our study, it was apparent that the MatLyLu cell line was the most lethal, whereas the DU-145 and the PC-3 cell lines were comparable both in terms of spontaneous and experimental metastasis. Although PC-3 has been observed to metastasize to the lung in other studies, this has mainly occurred from surgical orthotopic implantation in the prostate [44–46]. It is possible that in the orthotopic site PC-3 can establish better vasculature despite its low level of VEGF expression. The PC-3 cell line is undoubtedly highly invasive, and is almost identical to the MatLyLu cell line in terms of its invasive index. The results from the subcutaneous implantation of PC-3 suggests that the invasive and angiogenic phenotypes may represent two distinct subsets, i.e., highly invasive behavior does not necessarily predict for high VEGF expression or high vascularization or metastasis. Results from studies with poorly invasive MCF-7 cells transfected to overexpress the angiogenic factor FGF-1 demonstrate that angiogenic capability alone does not determine the metastatic end-point [47]; our data suggest that neither does the invasive capacity. Rather, cancer cells expressing both high invasive and angiogenic capacity represent the most lethal phenotype. Our data also suggest that targeting angiogenesis may be even more effective than targeting invasion for reducing or preventing metastasis.

**Acknowledgements**

We gratefully acknowledge and thank Gerald Rottman for his invaluable support and for providing us with detailed descriptions for preparing albumin–GdDTPA. We thank Noriko Mori for synthesis of albumin–GdDTPA, Gary Cromwell for maintaining the cell lines and inoculating the

tumors, and Joel B. Nelson for providing us with the prostate cancer cell lines. We gratefully acknowledge useful discussions with R. J. Gillies and Joel B. Nelson.

## References


[1] Srivastava A, Laidler P, Davies RP, Horgan K, and Hughes LE (1988). The prognostic significance of tumor vascularity in intermediate-thickness (0.76–4.0 mm thick) skin melanoma. A quantitative histologic study. *Am J Pathol* **133**, 419–423.

[2] Weidner N, Semple JP, Welch WR, and Folkman J (1991). Tumor angiogenesis and metastasis-correlation in invasive breast carcinoma. *N Engl J Med* **324**, 1–8.

[3] Thompson WD, Li WW, and Maragoudakis M (1999). The clinical manipulation of angiogenesis: pathology, side-effects, surprises, and opportunities with novel human therapies. *J Pathol* **187**, 503–510.

[4] Horak ER, Leek R, Klenk N, LeJeune S, Smith K, Stuart N, Greenall M, Stepniewska K, and Harris AL (1992). Angiogenesis, assessed by platelet/endothelial cell adhesion molecule antibodies, as indicator of node metastases and survival in breast cancer. *Lancet* **340**, 1120–1124.

[5] Wakui S, Furusato M, Itoh T, Sasaki H, Akiyama A, Kinoshita I, Asano K, Tokuda T, Aizawa S, and Ushigome S (1992). Tumour angiogenesis in prostatic carcinoma with and without bone marrow metastasis: a morphometric study. *J Pathol* **168**, 257–262.

[6] Siegal JA, Yu E, and Brawer MK (1995). Topography of neovascularity in human prostate carcinoma. *Cancer* **75**, 2545–2551.

[7] Bossi P, Viale G, Lee AK, Alfano R, Coggi G, and Bosari S (1995). Angiogenesis in colorectal tumors: microvessel quantitation in adenomas and carcinomas with clinicopathological correlations. *Cancer Res* **55**, 5049–5053.

[8] Schmiedl U, Ogan M, Paajanen H, Marotti M, Crooks LE, Brito AC, and Brasch RC (1987). Albumin labeled with Gd-DTPA as an intravascular, blood pool-enhancing agent for MR imaging: biodistribution and imaging studies. *Radiology* **162**, 205–210.

[9] Schwarzbauer C, Syha J, and Haase A (1993). Quantification of regional blood volumes by rapid T1 mapping. *Magn Reson Med* **29**, 709–712.

[10] Su MY, Muhler A, Lao X, and Nalcioglu O (1998). Tumor characterization with dynamic contrast-enhanced MRI using MR contrast agents of various molecular weights. *Magn Reson Med* **39**, 259–269.

[11] Pilatus U, Ackerstaff E, Artemov D, Mori N, Gillies RJ, and Bhujwalla ZM (2000). Imaging prostate cancer invasion with multi-nuclear magnetic resonance methods: the Metabolic Boyden Chamber. *Neoplasia* **2**, 273–279.

[12] Abramovitch R, Marikovsky M, Meir G, and Neeman M (1998). Stimulation of tumour angiogenesis by proximal wounds: spatial and temporal analysis by MRI. *Br J Cancer* **77**, 440–447.

[13] Aboagye EO, and Bhujwalla ZM (1999). Malignant transformation alters membrane choline phospholipid metabolism of human mammary epithelial cells. *Cancer Res* **59**, 80–84.

[14] Isaacs JT, Isaacs WB, Feitz WF, and Scheres J (1986). Establishment and characterization of seven Dunning rat prostatic cancer cell lines and their use in developing methods for predicting metastatic abilities of prostatic cancers. *Prostate* **9**, 261–281.

[15] Ogan MD, Schmiedl U, Moseley ME, Grodd W, Paajanen H, and Brasch RC (1987). Albumin labeled with Gd-DTPA. An intravascular contrast-enhancing agent for magnetic resonance blood pool imaging: preparation and characterization [published erratum appears in *Invest Radiol* 1988 Dec;23(12):961]. *Invest Radiol* **22**, 665–671.

[16] Braunschweiger PG, and Schiffer LM (1986). Effect of dexamethasone on vascular function in RIF-1 tumors. *Cancer Res* **46**, 3299–3303.

[17] Bhujwalla ZM, Artemov D, and Glockner J (1999). Tumor angiogenesis, vascularization, and contrast-enhanced magnetic resonance imaging. *Top Magn Reson Imaging* **10**, 92–103.

[18] Ravi R, Mookerjee B, Bhujwalla ZM, Sutter CH, Artemov D, Zeng Q, Dillehay LE, Madan A, Semenza GL, and Bedi A (2000). Regulation of tumor angiogenesis by p53-induced degradation of hypoxia-inducible factor 1alpha. *Genes Dev* **14**, 34–44.

[19] Laemmli UK, Beguin F, and Gujer-Kellenberger G (1970). A factor preventing the major head protein of bacteriophage T4 from random aggregation. *J Mol Biol* **47**, 69–85.

[20] Towbin H, Staehelin T, and Gordon J (1979). Electrophoretic transfer of proteins from polyacrylamide gels to nitrocellulose sheets: procedure and some applications. *Proc Natl Acad Sci USA* **76**, 4350–4354.

[21] Donahue KM, Burstein D, Manning WJ, and Gray ML (1994). Studies of Gd-DTPA relaxivity and proton exchange rates in tissue. *Magn Reson Med* **32**, 66–76.

[22] Donahue KM, Weisskoff RM, Parmelee DJ, Callahan RJ, Wilkinson RA, Mandeville JB, and Rosen BR (1995). Dynamic Gd-DTPA enhanced MRI measurement of tissue cell volume fraction. *Magn Reson Med* **34**, 423–432.

[23] Levy BI, Duriez M, Phillipe M, Poitevin P, and Michel JB (1994). Effect of chronic dihydropyridine (isradipine) on the large arterial walls of spontaneously hypertensive rats. *Circulation* **90**, 3024–3033.

[24] van Dijke CF, Brasch RC, Roberts TP, Weidner N, Mathur A, Shames DM, Mann JS, Demsar F, Lang P, and Schwickert HC (1996). Mammary carcinoma model: correlation of macromolecular contrast-enhanced MR imaging characterizations of tumor microvasculature and histologic capillary density. *Radiology* **198**, 813–818.

[25] Okuhata Y, Brasch RC, Pham CD, Daldrup H, Wendland MF, Shames DM, and Roberts TP (1999). Tumor blood volume assays using contrast-enhanced magnetic resonance imaging: regional heterogeneity and postmortem artifacts. *J Magn Reson Imaging* **9**, 685–690.

[26] Tozer GM, and Morris CC (1990). Blood flow and blood volume in a transplanted rat fibrosarcoma: comparison with various normal tissues. *Radiother Oncol* **17**, 153–165.

[27] Peterson H-I (1979). Vascular and extravascular spaces in tumors: tumor vascular permeability. In *Tumor Blood Circulation: Angiogenesis, Vascular Morphology and Blood Flow of Experimental and Human Tumors*. H-I Peterson (Ed). CRC Press, Boca Raton. pp. 77–85.

[28] Sands H, Shah SA, and Gallagher BM (1985). Vascular volume and permeability of human and murine tumors grown in athymic mice. *Cancer Lett* **27**, 15–21.

[29] Levy AP, Levy NS, and Goldberg MA (1996). Post-transcriptional regulation of vascular endothelial growth factor by hypoxia. *J Biol Chem* **271**, 2746–2753.

[30] Shweiki D, Itin A, Soffer D, and Keshet E (1992). Vascular endothelial growth factor induced by hypoxia may mediate hypoxia-initiated angiogenesis. *Nature* **359**, 843–845.

[31] Plate KH, Breier G, Weich HA, and Risau W (1992). Vascular endothelial growth factor is a potential tumour angiogenesis factor in human gliomas *in vivo*. *Nature* **359**, 845–848.

[32] Shweiki D, Neeman M, Itin A, and Keshet E (1995). Induction of vascular endothelial growth factor expression by hypoxia and by glucose deficiency in multicell spheroids: implications for tumor angiogenesis. *Proc Natl Acad Sci USA* **92**, 768–772.

[33] Furman-Haran E, Margalit R, Grobgeld D, and Degani H (1996). Dynamic contrast-enhanced magnetic resonance imaging reveals stress-induced angiogenesis in MCF7 human breast tumors. *Proc Natl Acad Sci USA* **93**, 6247–6251.

[34] Jain RK (1987). Transport of molecules in the tumor interstitium: a review. *Cancer Res* **47**, 3039–3051.

[35] Jain RK (1987). Transport of molecules across tumor vasculature. *Cancer Metastasis Rev* **6**, 559–593.

[36] Chen HJ, Treweeke AT, Ke YQ, West DC, and Toh CH (2000). Angiogenically active vascular endothelial growth factor is over-expressed in malignant human and rat prostate carcinoma cells. *Br J Cancer* **82**, 1694–1701.

[37] Hyder SM, Murthy L, and Stancel GM (1998). Progestin regulation of vascular endothelial growth factor in human breast cancer cells. *Cancer Res* **58**, 392–395.

[38] Iruela-Arispe ML, Lombardo M, Krutzsch HC, Lawler J, and Roberts DD (1999). Inhibition of angiogenesis by thrombospondin-1 is mediated by 2 independent regions within the type 1 repeats. *Circulation* **100**, 1423–1431.

[39] Tempel C, Gilead A, and Neeman M (2000). Hyaluronic acid as an anti-angiogenic shield in the preovulatory rat follicle. *Biol Reprod* **63**, 134–140.

[40] Melnyk O, Shuman MA, and Kim KJ (1996). Vascular endothelial growth factor promotes tumor dissemination by a mechanism distinct from its effect on primary tumor growth. *Cancer Res* **56**, 921–924.

[41] Price JE, Polyzos A, Zhang RD, and Daniels LM (1990). Tumorigenicity and metastasis of human breast carcinoma cell lines in nude mice. *Cancer Res* **50**, 717–721.

[42] Thompson EW, Brunner N, Torri J, Johnson MD, Boulay V, Wright A, Lippman ME, Steeg PS, and Clarke R (1993). The invasive and metastatic properties of hormone-independent but hormone-respon-

sive variants of MCF-7 human breast cancer cells. *Clin Exp Metastasis* **11**, 15–26.

[43] Levy JA, White AC, and McGrath CM (1982). Growth and histology of a human mammary-carcinoma cell line at different sites in the athymic mouse. *Br J Cancer* **45**, 375–383.

[44] An Z, Wang X, Geller J, Moossa AR, and Hoffman RM (1998). Surgical orthotopic implantation allows high lung and lymph node metastatic expression of human prostate carcinoma cell line PC-3 in nude mice. *Prostate* **34**, 169–174.

[45] Waters DJ, Janovitz EB, and Chan TC (1995). Spontaneous metastasis of PC-3 cells in athymic mice after implantation in orthotopic or ectopic microenvironments. *Prostate* **26**, 227–234.

[46] Shevrin DH, Gorny KI, and Kukreja SC (1989). Patterns of metastasis by the human prostate cancer cell line PC-3 in athymic nude mice. *Prostate* **15**, 187–194.

[47] Zhang L, Kharbanda S, McLeskey SW, and Kern FG (1999). Overexpression of fibroblast growth factor 1 in MCF-7 breast cancer cells facilitates tumor cell dissemination but does not support the development of macrometastases in the lungs or lymph nodes. *Cancer Res* **59**, 5023–5029.